YOUNGSTOWN STATE UNIVERSITY

# Nano-Characterization of Ceramic-Metallic Interpenetrating Phase Composite Material using Electron Crystallography

by

Marjan Moro

Submitted in Partial Fulfillment of the Requirements
for the Degree of Master of Science in Engineering
in the Mechanical Engineering Program

Mechanical and Industrial Engineering

May 2012

# Nano-Characterization of Ceramic-Metallic Interpenetrating Phase Composite Material using Electron Crystallography

by

Marjan Moro

I hereby release this thesis to the public. I understand that this thesis will be made available from the OhioLINK ETD Center and the Maag Library Circulation Desk for public access. I also authorize the University or other individuals to make copies of this thesis as needed for scholarly research.

Signature: _____

*Marjan Moro*, Student Date

Approvals: _____

*Dr. Virgil C. Solomon*, Thesis Advisor Date

_____

*Dr. Matthias Zeller*, Committee Member Date

_____

*Dr. Timothy R. Wagner*, Committee Member Date

_____

*Dr. Hyun W. Kim*, Committee Member Date

_____

*Dr. Peter J. Kasvinsky*, Dean of Graduate Studies Date

# *Abstract*

Interpenetrating phase composites (IPCs) have unique mechanical and physical properties and thanks to these they could replace traditional single phase materials in numbers of applications. The most common IPCs are ceramic-metallic systems in which a ductile metal supports a hard ceramic making it an excellent composite material. Fireline, Inc., from Youngstown, OH manufactures such IPCs using an Al alloy-$Al_2O_3$ based ceramic-metallic composite material. This product is fabricated using a Reactive Metal Penetration (RMP) process to form two interconnected networks. Fireline products are used, among others, as refractory materials for handling of high temperature molten metals.

A novel route to adding a shape memory metal phase within a ceramic matrix has been proposed. A NiO preform was reacted with Ti to produce an IPC using a plasma arc melting system. This reaction is particularly interesting due to the possible formation of a Ni-Ti metal phase which could exhibit shape memory effects within the ceramic-metal network. Different ratios of NiO and $TiO_2$ (rutile) were reacted with Ti to investigate if the NiTi phase could be formed.

In this thesis, two IPCs, one produced by the TCON RMP process and the other by using plasma arc-melting were investigated. The materials include Al-Fe alloy-$Al_2O_3$ and NiO-Ti ceramic-metallic IPCs. Analysis was performed using scanning/transmission electron microscopy (S/TEM), energy dispersive spectroscopy (EDS), focused ion beam (FIB), and X-ray diffraction (XRD). Observations of these IPCs revealed all present phases within the composite material, obtained orientation relationships, and explored the growth mechanism of the RMP process which still puzzles the scientific community. This information is valuable for developing improved IPC systems with diverse elemental composition for a wide variety of applications.

# *Acknowledgements*

I want to thank my family for the love and support they have provided to me throughout my schooling.

I would like to thank my advisor, Dr. Virgil Solomon, for constantly challenging me to achieve more while guiding me in the right direction during my graduate studies at Youngstown State University. The expertise he has shared with me will certainly help me in my professional career. Furthermore, working with Dr .Solomon has helped me grow as an individual.

I would also like to thank my thesis committee members. First and foremost I would like to thank Dr. Matthias Zeller for spending endless amount of time with me having fruitful discussions. Next I would like to thank Dr. Timothy Wagner for allowing me to use his lab space and for managing my student funding during my studies. Lastly, I would like to thank Dr. Hyun Kim for being there from the beginning to end of my graduate studies and guiding me through the graduate school process.

I am also appreciative of Mr. Klaus-Markus Peters and Mr. Brian Hetzel of Fireline Inc. for providing me with the opportunity to study their company's products.

Finally, I would like to thank my friends and family for listening to me talk hours upon hours about all the academics that I enjoy so much and for trying to understand what captivates me.

# Contents

# List of Figures

# List of Tables

# List of Symbols and Terminology

| | |
|---|---|
| Å | Ångstrom ($10^{-9}$ meters) |
| $\alpha$ | Alpha, lattice angle |
| a, b, c | Cell lattice parameters |
| Al | Aluminum |
| $Al_2O_3$ | Aluminum oxide, Alumina |
| At.% | Atomic percentage |
| $\beta$ | Beta, lattice angle |
| Backscatter | Referring to elastic scattering of electrons or ions |
| BF | Bright Field |
| °C | Degree Celsius |
| CBED | Convergent Beam Electron Diffraction |
| CFQ | Clear Fused Quartz |
| CTF | Contrast Transfer Function |
| cm | Centimeters |
| d | Distance, interplanar spacing |
| EDS | Energy Dispersive Spectroscopy |
| eV | Electron V |
| *F* | Face centered unit cell type |
| Fe | Iron |
| FIB | Focused Ion Beam |
| $\gamma$ | Gamma, lattice angle |
| $\Delta$G | Gibbs free energy (KJ/mol or kcal/mol) |
| hkl | Miller indicies |

| | |
|---|---|
| hr | Hour |
| HREM | High Resolution Electron Microscopy |
| $I$ | Body centered unit cell type |
| IPC | Interpenetrating Phase Composite |
| KE | Kinetic Energy |
| L | Liquid |
| $\lambda$ | Wavelength |
| Micron | 1 $\mu$m ($10^{-6}$m), micrometer |
| mol | Mole |
| n | Integer (1,2,3,...,n) |
| O | Oxygen |
| OR | Orientation Relationship |
| Preform | Starting material of the RMP process (typically silica based) |
| RMP | Reactive Metal Penetration |
| SADP | Selected Area Diffraction Pattern |
| Secondary electron | Referring to inelastic scattering of electrons |
| SEM | Scanning Electron Microscopy |
| Si | Silicon |
| $SiO_2$ | Silicon dioxide, silica |
| Space group | Classification describing a crystal's symmetry |
| S/TEM | Scanning/Transmission Electron Microscopy |
| $\theta$ | Theta, incident angle |
| Ti | Titanium |
| Transformation | Production of an IPC via chemical reaction during the RMP process |
| wt.% | Weight percentage |
| XRD | X-Ray Diffraction |
| x,y,z | Coordinate/direction system |

*Dedicated to my family; Zdenko, Dubravka, and Vanesa Moro ...*

# Chapter 1

# Introduction

There has been an increasing interest in the production of novel Interpenetrating Phase Composite (IPC) materials.[1] IPCs represent a family of materials whose microsctructure is characterized by the continuity and interconnection of two or more phases.[2] The most common studied IPCs are ceramic-metallic systems due to many of their favorable properties. These properties include high resistance to thermal gradients, good resistance against corrosion, and high strength with decreased weight compared to more traditional composite materials.[3] Currently the primary use for these composites is in the aerospace industry. Airframe and spacecraft components are being build with IPCs due to their favorable properties in harsh enviroments.[3] IPCs were engineered to possess a superior blend of properties over traditional composites and therefore other industries such as automotive, refractory, and lately also the military have considered using IPCs for various applications.[4,5]

The most studied IPCs contain a combination of ceramic and metallic phases, particularly $Al_2O_3$ and Al.[2] The ceramic phase contributes high strength, high thermal resistance, and high wear resistance which is supported by tough ductile metallic ligaments.[6] The continuity of the interconnecting phases plays a vital role in providing superior mechanical properties over other composite materials containing the same constituents. Continuity can be demonstrated by conducting electricity and heat through the metal

phase, while the overall thermal expansion is limited by the ceramic phase.[5] Even though the Al-$Al_2O_3$ system is "good enough" for many applications, attempts have been made to find the upper limit of strength, wear resistance, and hardness for IPCs by adding combinations of alloying metals to the composite.[7] Radical modifications such as using a different kind of ceramic-metallic system have been proposed in order to obtain unique new IPC materials. For example, in the present work, it is hypothesized that a NiO-Ti system could potentially exhibit shape memory effects, if NiTi-(nitinol) metal could be obtained during the formation of the IPC.

Variations in properties of the IPC can be accomplished through the addition of alloying elements to the molten metal bath. In this thesis, the addition of iron to the $Al_2O_3$-Al system will be examined. Adding Fe to the process will induce the formation of an Al-Fe phase. Al-Fe based alloys have considerable potential for structural applications at high temperature as they posses improved strength compared to common Al-$Al_2O_3$ IPC.[8] In addition to the improved properties, iron is available at a comparatively lower price than other high-temperature alloying metals.[9]

The fabrication process of these composite materials requires precise synthesis paramerters in order to produce stable IPCs. Over the years many processes have been introduced including combustion synthesis, robotic deposition, direct metal oxidation[6], pressurized melt infiltration, and liquid-solid displacement. All of these processes possess disadvantages such as size and shape restriction, porosity, difficult reproducibility, and excessive costs. The process which showed the highest potential is Reactive Metal Penetration (RMP) also known in the literature as a liquid-solid displacement reaction. The RMP process has few of the disadvantages mentioned above.[10] On the other hand, the greatest advantage of this process is that it can be replicated on an industrial scale. RMP uses a sacrificial oxide, also known as the preform, which is submerged into a molten metal bath for a given period of time. During this time a chemical reaction occurs where the metal penetrates the preform to produce an IPC.[10]

The chemical reaction that occurs between the ceramic and the metal can be classified as a thermite reaction.[11] A thermite reaction refers to an often extremely exothermic process occurring between a metal oxide (AO) and a more electropositive metal (M). The more reactive metal (M) reduces the metal oxide (AO), oxidizes itself (MO) and in the process releases a substantial amount of energy ($\Delta$H).[12] Often times the reaction temperature exceeds the melting temperature of the phases, and the process becomes difficult to control which often results in the formation of unwanted phases in the final product.[13] Nevertheless, there are a few combinations of metal-oxides that react in a predicable manner allowing for the formation of IPCs. The combination of silica and aluminum is one of those exceptions. Equation 1.1 shows the chemical reaction between sacrificial oxide and molten metal bath:

$$M + AO \rightarrow MO + A + \Delta H \tag{1.1}$$

where M is a metal or an alloy and A is either a metal or a non-metal, MO and AO are their corresponding oxides, and $\Delta$H is the heat generated by the reaction.[14] In simple terms the metal (M) strips away the oxide from the other metal/non-metal (A) and during this replacement of oxides excess energy is released in the form of heat $\Delta$H. This equation only explains the reaction but gives no inside into the formation mechanism of the IPCs. There have been many theories on the IPC formation mechanism but it is still not well understood despite decades of research. This thesis focuses on two separate projects. The first project involves analyzing already fabricated composite materials provided by a local company Fireline, Inc., while the second project was an attempt to fabricate and analyze new composite materials not yet described in the literature.

For the first project, material was manufactured using the TCON process of Fireline, Inc., located in Youngstown, Ohio. The TCON process uses the RMP process in order fabricate IPCs. This material was manufactured using clear fused quartz (CFQ)

preforms transformed at 1200 °C. The CFQ was transformed in an aluminum-alloy containing 7.5% iron by weight. The process with and without alloying additives can be described with the following two equations:

$$3SiO_2 + 4Al \rightarrow 2Al_2O_3 + 3Si \tag{1.2}$$

$$3SiO_2 + 4Al + (additives) \rightarrow 2Al_2O_3 + (additives) + 3Si \tag{1.3}$$

Fireline also provided additional samples that were only partially transformed for better understanding of the transformation mechanism of this IPC. Previous thesis work on determining how alloying additions of Si and Fe to the molten metal melt would affect the final product has been done by past graduate students Ryan Paul[5] and Anthony Yurcho[11]. These past studies did not include any TEM investigations. One of the objectives of this study was to use transmission electron microscopy (TEM) techniques to further characterize the materials provided by Fireline down to the nano-level. Special emphasis was placed on using electron crystallography to help explore the crystallographic orientation relationships between various metallic and ceramic phases.

The second project involved a novel idea to produce an IPC material that has not been described previously. Since combining ceramic-metallic phases gives rise to favorable properties, the goal was to find a ceramic-metal pair that would exhibit new unique properties. Liu and Köster claim in their paper that NiO (ceramic) and Ti (metal) would combine to form an IPC.[30] This combination would be ideal if the metal phase NiTi would be present in the interpenetrating networks since it exhibits shape memory effects. The objective was to first successfully synthesize an IPC from NiO and Ti and then maximize the NiTi content within the IPC. Combining the advantages of IPCs with shape memory effect materials would be useful in many ways. The present work is organized into five chapters, as follows:

*Chapter 2 Background*: reviews the literature available on $Al_2O_3$-Al-Fe and NiO-Ti.

*Chapter 3 Experimental*: details the plan, materials and procedures used in conducting various experiments.

*Chapter 4 Results*: describes the results obtained and correlates them with the available information from the literature.

*Chapter 5 Conclusion*: Summarize the obtained results and proposes future work.

# Chapter 2

# Background

## 2.1 Introduction to Interpenetrating Phase Composites (IPCs)

Interpenetrating phase composites (IPCs) are defined as multiphase composites in which each phase is topologically interconnected throughout the microstructure. In the past the approach to making composite materials resulted in discrete, dispersed, and isolated phases embedded within a homogeneous phase. Only diluted concentration of the second phase could be integrated within the first phase. Recent developments in processing made it possible to deliberately make composite materials in which each phase is continuous and interconnecting throughout the structure. The ability to manufacture such materials gives rise to a truly multifunctional material since each phase will contribute its own properties to the macroscopic properties of the composite. For example, while one phase might provide strength the other might provide stiffness to the composite. Interpenetrating composites are relatively common in biology such as bones in mammals and the limbs of many plants but there are only few examples.[15] Intense research has been done on IPCs over the last two decades since they posses such unique multifunctional properties. As a result numerous fabrication processes and applications for IPCs materials have been proposed. In some cases such as the aerospace industry these materials are already being used.[3]

The most studied IPCs are ceramic-metallic systems because they combine very different properties of ceramics and metals into one set of unique properties. Ceramic-metallic composites contain a stiff, thermally resistant ceramic phase supported by ductile metal ligaments which makes them useful to many types of applications. The most studied ceramic-metal system is the alumina-aluminum ($Al_2O_3$-Al) system. The popularity of this system has to do with the availability of the starting materials and low cost of manufacturing of this system over other systems.[4] These IPC composites are manufactured using a reactive metal penetration (RMP) process. An advantage of using the RMP technique resides in the fact that the shape of the preform is preserved upon reaction. Hence, the final product has the same net shape as the starting pre-form. Moreover, the final product can be modified by adding various components to the molten metal to attain a desired property. For example, the addition of Fe will give the final product better high temperature properties.[9] In another example, SiC additions increase the thermal conductivity of the final product.[15] Alumina-aluminum based systems are not the only ceramic-metal IPCs that can be produced. For instance, in this thesis an attempt has been made to transform nickel oxide with titanium (NiO-Ti) into an IPC. Unlike the $Al_2O_3$-Al IPC there have been no studies done on this particular system.

In traditional composite materials the reinforcement is prepared separately and then mixed with the matrix by different methods such as powder metallurgy, casting route, and spray deposition.[16] Recently, there have been several processes developed to produce ceramic-metallic IPCs using in-situ techniques such as reactive sintering[17], combustion synthesis[18,19], pressurized melt infiltration[20], liquid displacement reaction[1,3,21], and robotic deposition[2].

## 2.2 Chronological Literature Review on IPCs

In 1953, Brondyke[22] published a research paper about a reaction of molten aluminum with alumina-silica refractories in an open-hearth furnace. It was found that when

aluminum is molten and held in a furnace lined with alumina-silica refractories, there was a gradual penetration of aluminum into the refractory. In his research this reaction between aluminum metal and the refractory material alumina-silica did pose a problem since the displacement reaction deposits silicon impurities into the molten aluminum bath. It was noted that the temperature plays a major role in the reaction because penetration was negligible at 704°C but increased rapidly at a temperature of 760°C. The wetting and penetration of silica by molten aluminum was found on accident by using silica based refractories. At the time this was considered an unsuitable refractory since it would add impurities to the aluminum. Brondyke is the first to report such a reaction taking place but his intention was not to make IPCs.

The first documented attempt to produce interpenetrating phase composites is by Henri George[23] in 1955. His objective was to manufacture materials having metallic aspects with a highly refractory nature, while being very hard, and with good electric conductivity. He explained the reaction using the following equation:

$$SiO_2 + M \rightarrow MSi^n + MO_x \tag{2.1}$$

in which $SiO_2$ is combined or free silica, M is any reducing metal, MSi is an alloy of metal M with silicon, n signifies the proportions of M and Si, and $MO_x$ is an oxide of metal M. He even hypothesized that more then one metal can be added to play the role of additives. The silica does not have to be solid quartz but is open to other kinds of silica such as sand or pure fused silica. For the reducing metals Al is primarily described but other possibilities such as Mg, Na, K, Li, and Ca are mentioned. Combinations of the metal alloys can be used in order to produce particular interesting alloys. A reaction temperature between 700°C and 900°C was used. George correlates temperature with increase in size of alumina grains, stating that upon increasing the temperature to 1000°C the grain size of alumina would increase. A detailed explanation of the process is provided as follows. A silica glass was submerged in a bath of aluminum and was transformed progressively. The final product is composed of 80% alumina, 20% metal,

and containing four times more aluminum than silicon in the metal phase. This final product conserved both its shape and dimensions meaning that the shape was preserved. However, microstructual analysis was not preformed on the final product. Even today a very similar procedure is used to produce IPCs. Even-though George managed to produce such a composite material there was no research done for many years after his patent was published.

Standage and Gani[24], in 1967, published research on the reaction of fused silica rods in molten aluminum doped with additives. In their study, different amounts of antimony and bismuth were added to the molten aluminum. Silica rods were preheated for 15 minutes before being submerged into the molten bath. After removal from the melt, the rods were suspended in air for 3 minutes. It was noted by the authors that if the hot rods came in contact with a cold surface they shattered immediately. X-ray diffraction (XRD) analysis revealed four distinct products produced by the reaction; silicon, $\nu$-alumina, $\theta$-alumina, and $\alpha$-alumina. The authors did not mention any aluminum being revealed by XRD. The major findings of this study can be summarized as: (1) high concentrations of bismuth and antimony lowered the rate of penetration and increased the reaction time; (2) at low concentrations of the additives, they reduced the activation energy for the formation of $\theta$-alumina. Hence, bismuth and antimony both have an effect on the reaction time and the formation of certain types of alumina depending on the amount of additives used.

During the '70s there were two main methods for producing composite materials. The first method uses powder metallurgy techniques which involved hot-pressing, cold-pressing, and sintering mixtures of ceramic and metallic powders. The second method is liquid-metal infiltration which utilizes a pre-fabricated porous ceramic material that is infiltrated by a liquid metal.[11] Both of these methods still had problems such as high final porosity, low obtainable ceramic volume, discontinuity of phases, and shape/size restrictions.[25]

In 1980, Grimshaw *et al.*[26] addressed the problem of wetting between ceramics and metals. Wetting can be best defined as the ability for a liquid to remain in contact with a solid surface. For example, liquids that have poor wettability with solid surfaces tend not to react with the solid due to poor intermolecular interactions. The solution to the wetting problem was to fabricate a porous ceramic matrix and infiltrate it with the metal. Grimshaw 's patent explains the use of volatile agents such as nickel and tungsten, chromium, titanium or copper. A uniform mixture of these metals coated the alumina in a fibrous or whisker form, then was placed in a mold and hot pressed into a solid form. The combined effect of the temperature and the pressure was chosen to be such that partial liquefaction of the metal would occur during the pressing operation. This method produced increased porosity in the alumina which then can be infiltrated with the metal. This was the first paper that reported the use of volatile agents in to increase the porosity of alumina.

In 1993, Michael C. Breslin[27] published a similar procedure for producing composite materials as George[23] did 40 years earlier. The patent starts of by distinguishing it from other processes as those mentioned above by Brondyke's[22], Standage's[77], Prabriputaloong's[78], and the Lanxide's[79] process. No mention of George's[23] process was included in the patent. The process involves the reaction of silica ($SiO_2$), which can be either polycrystalline or amorphous, with a molten aluminum alloy or pure molten aluminum. He explains it with aluminum but the process is not limited to only aluminum but other components such as iron, nickel, cobalt can also be used. Alloying metals such as magnesium, titanium, tungsten, and tantalum can also be included in the molten bath. The pre-form ceramic and the molten metal are maintained in contact at a temperature ranging from 1000°C to about 1250°C for a time sufficient enough to allow the preform to be transformed into a ceramic metal oxide body containing a metallic phase. The correlation between higher temperatures and increased transformation rate is observed similarly as to George's[23] observation. The final product yields a co-continuous ceramic-metallic composite that is approximately 70% alumina ceramic and 30% aluminum metal. The equation for the reaction is put as follows:

$$AwBx + M \rightarrow ByMz + A \tag{2.2}$$

where AwBx is the sacrificial ceramic preform, and M can be Al, Fe, Ni, Co, Mg, Ti, Ta, W, Y or Nb. B can be oxygen, nitrogen, sulfur, or carbon. The subscripts w, x, y, z need not be whole numbers and can be independently selected depending on the molecular stoichiometry. AwBx is the sacrificial oxide such as $SiO_2$ or $TiO_2$. This equation is identical to the one provided by George[23]. The patent does include a mechanism theory that could explain the formation of the composite material. Physical properties such as coefficients of thermal expansion and thermal conductivity were also included.

Prior to this patent, Breslin's[28] master thesis documented this new composite material. Due to the observed microstructure, he named the material a co-continuous ceramic-metal composite or C4. The main contribution was the correlation between temperature range and phases of alumina obtained. He reported the reaction observations from three different temperature ranges: $700 - 800°C$, $800 - 1000°C$, and $1000 - 1150°C$. The only temperature range that produced an interpenetrating phase composite of $\alpha$-alumina and aluminum metal was the $1000 - 1150°C$ range. The other temperature ranges produced undesirable meta-stable alumina phases.

Two years after Breslins thesis and patent, another paper was published by Breslin *et al.*[1] with additional research about his co-continuous composite (C4) material. The manufacturing process for this material is exactly as explained in his patent using the liquid-solid displacement reaction. A detailed theory of the formation mechanism is provided. As the pre-form Silica ($SiO_2$) is submerged in the liquid Al, a liquid phase displacement reaction takes place. A thin layer of alumina ($Al_2O_3$) is formed on the surface of the $SiO_2$. This layer of alumina experiences an approximate 35% volumetric contraction. The contraction causes cracks to form allowing liquid Al to penetrate deeper into the $SiO_2$ and to continue the reaction. Liquid Al fills these channels and the silicon (Si), which is displaced from the $SiO_2$ preform, diffuses out of the newly formed composite along the Al channels to the surrounding bath. During cooling to room

temperature the remaining Si becomes supersaturated in the Al of the composite and it precipitates out of the final product. TEM analysis shows a strong bond between the two phases with an additional effect of mechanical keying afforded by the development of the facets along the interface.

After many years researching the liquid-solid reaction approach some scientists tried novel methods of fabricating IPCs. In 1995, Feng and Moore[18] proposed a one-step in-situ combustion synthesis technique to produce IPC materials. In their study the following equation was used:

$$3TiO_2 + 3C + (4+x)Al + yAl_2O_3 \rightarrow 3TiC + (2y)Al_2O_3 + xAl \tag{2.3}$$

The quantities were varied by changing x and y to produce different characteristic composite materials. Their reaction can be classified as a combustion (self-propagating high-temperature) synthesis (SHS) which uses an exothermic reaction to provide the energy needed to synthesize the composite material. The reactants are mixed in powder form and pressed into pellets. These pellets are then heated until there is enough energy to ignite, and at that instance the reaction self- propagates due to the highly exothermic heat release; no additional heat has to be provided. Previous attempts in making IPCs using SHS resulted in relatively high levels of porosity. Feng and Moore[18] saw this as an advantage rather then a disadvantage. They applied a compressive load to the pellet as soon as the exothermic reaction occurred. The pressure will fill the voids with Al metal and the net result is an interpenetrating phase composite of ceramic and metal. Although this method is energy efficient, limitations are imposed on shape and size of the pellet.

In 1996 Daehn *et al.*[29] published data on the mechanical behavior of a co-continues composite (C4) material which was manufactured by Breslin's[28] procedure. The macroscopic behavior of the material can not be considered fully ductile since the larger part of the structure consists of a continuous ceramic phase which can not experience extensive

plastic deformation. Hence, mechanical behavior of the stiff ceramic can be classified as elastic-plastic due to the ductile aluminum ligaments that support the alumina. Furthermore, TEM micrographs were taken from a sample deformed by compression. Observed was a high dislocation density in the aluminum phase while the ceramic did not fracture. This clearly demonstrates the stiffening effect of the ceramic in preventing the movement of dislocation in the metal phase. In conclusion, the deformation of this material takes place by plastic deformation in the metal phase that is accommodated by elastic deformation in the ceramic phase.

Liu and Köster[30] published research, in 1996, on the criteria necessary to produce IPCs using different kinds of metals. First they propose a similar transformation mechanism as published by Breslin[28]. Then they give criteria for the formation of oxide/metal composites with an interpenetrating microstructructure as follows: (1) the ceramic produced (i.e. alumina) must have a smaller volume than the sacrificial oxide (silica). (2) The ceramic produced must be more thermodynamically stable than the sacrificial oxide. (3) The processing temperature must be higher than the melting temperature of the reductive metal but lower than its boiling point. In addition, the processing temperature must be lower than the melting point of both the sacrificial oxide and the ceramic. The most significant addition of this publication is the proposal that various other systems are possible in producing IPCs besides the aluminum/alumina system.

Most procedures presented up till now used one step processes in producing IPCs. In 1998 Zhou *et al.*[31] used a two step process which consisted of a self-propagating synthesis (SHS) and pressurized metal infiltration to fabricate ceramic-metal IPCs. Rutile ($TiO_2$), aluminum (Al) powder, and graphite (C) were mixed together using a wet-mill. Cylindrical pellets were produced with different amounts of volatiles to enhance the pores of the pre-form. Next self-propagating synthesis was used under constant pressure to produce TiC-$Al_2O_3$ pre-form pellets. The porous SHS reaction product had about 83% porosity. This porous product was infiltrated with pure Al with a 2024 Al alloy at 750°C under 9MPa in a nitrogen atmosphere. The final product was an IPC. The

analysis showed that many pores were left un-infiltrated leaving high porosity in the sample. This could be due to the low gas pressure of 9MPa used to infiltrate the sample. Unfortunately the maximum infiltration pressure available was only 9MPa. Thus, the strength of the material also suffered due the high porosity of the material.

In 2000, Jung and Paik[32] published the results of their research on mechanical fracture behavior of alumina/aluminum IPCs transformed from clear fused quartz submerged into a pure aluminum melt. The transformed material was taken and strength tests were conducted parallel and perpendicular to the direction of the melt penetration. The main findings included that the strength and toughness were superior in the parallel direction rather than perpendicular direction. This result could help prevent catastrophic failure by knowing which direction to load more heavily.

Some interesting research was published by Banerjee and Roy[33] in 2001. First they fabricated a material by submerging silica glass into an aluminum molten bath at temperatures between $900 - 1300°C$ as described previously. However, they provided some interesting new information about the reaction front. When using electron-probe microanalysis (EPMA) around the reaction front, they observed it to be aluminum rich with little silicon. The authors claim that the reaction front is amorphous. After complete transformation, very little Si was found in the Al metal channels. Some known information was also verified such as linear reaction kinetics, presence of $\alpha$-alumina, and net-shape fabrication.

A truly ingenious method has been proposed by San Marchi *et al.*[2], in 2003, in producing interpenetrating phase composites. A robotic deposition method is used to fabricate a 3-D ceramic preform which then is infiltrated by a metal. Ceramic towers consisting of 30 orthogonal layers stacked on top of each other were produced by robotic deposition using an $Al_2O_3$-5% $ZrO^2$ gel. The tower's dimensions were 6 x 4 x 4 $mm^3$. After assembly the 30-layer tower was dried for 24 hours then sintered in air at 1600°C for 2.5 hours. The closed porosity of the $Al_2O_3$ towers was determined to be 9% by helium pycnometry. Closed porosity refers to pores that are isolate and that will remain pores after the

infiltration process. The infiltration process involved 99.99% aluminum at 750°C under 3.5 MPa in argon gas. The final product yielded 70% ceramic and 30% metal. Mechanical testing revealed inferior compressive strength than that for IPCs produced by solid-liquid displacement. A possible explanation for the variation in compressive strength is due to the finer structure obtained with the solid-liquid displacement reaction which yields a stronger material.

The orientation and grain boundary microstructure of an aluminum/alumina composite material has been investigated by Murth *et al.*[34] in 2005. A very poorly written paper in the sense that not all micrographs are labeled and information is unorganized. The material was manufactured using the RMP process with starting materials of Al and $SiO_2$. The silica pre-form reacts with excess molten aluminum at temperatures ranging from $1000 - 1400$°C. This yielded an alumina and aluminum IPC. The first finding worth noting is that the average width of the alumina grains is greater than that of the metal ligaments, 6.6 microns versus 3.5 microns, respectively. The X-ray diffraction data obtained from both horizontal and vertical sections indicate preferred orientation of $Al_2O_3$ in the composite material when compared to sintered random polycrystalline $Al_2O_3$. On the other hand, no such preferred orientation was found for the aluminum phase. The observed microstructure consisted of composite colonies, which are interconnected as previously reported. However, it appears that the growth of the colonies is restricted due to impingement. They also pointed out that any mismatch between the two growing fronts develops a plane of weakness by accumulation of pores. Pores will cause a decrease in strength of the composite material.

An attempt was made to give a concise accurate chronological literature review to-date on IPC materials. Even though a great deal of progress has been made in the past 60 years in the field of IPCs, there are still many questions that puzzle the scientific community. For instance, the formation mechanism is still unspecified. Also, there still are possibilities to explore other ceramic-metal systems rather than only the common $Al_2O_3$ system.

## 2.3 Modus Operandi of Ceramic-Metallic IPCs

There are two main questions in producing ceramic-metallic IPCs: (1) which elements will combine together in forming such a compound and (2) how does the transformation mechanism work. The next two sections will address those questions.

### 2.3.1 Conditions for IPCs

The chemical reaction to produce IPCs consists of a metal reacting with a (non)-metal oxide to produce a more stable oxide, which is classified as a thermite reaction[15]. Thermite reactions are often extremely exothermic. Proper constituents have to be chosen in order to produce an IPC from a thermite reaction. Due to the exothermic nature of the thermite reaction it is generally difficult to predict the final product.[13] In many cases there is enough heat released to melt both the metal and the non-metal oxide. Another challenge is the speed and intensity of the thermite reaction which makes it difficult to form a product with a controlled microstructure.[35] For example, the reaction between Al and $SiO_2$ is favorable for the formation of IPCs because it proceeds slowly and has an adiabatic temperature of 1487°C.[13] This temperature is ideal since it is less than the melting temperature of the final product $Al_2O_3$. This is one of the reasons the $Al_2O_3$-Al system is the most studied IPC.

Liu and Köster[30] specify the criteria that have to be met in order to obtain an IPC by submerging a dense sacrificial oxide preform into a molten metal bath. The paper outlines three conditions: (1) the ceramic produced must have a smaller volume then the sacrificial oxide. (2) The ceramic produced must be more thermodynamically stable than the sacrificial oxide. (3) The processing temperature must be higher than the melting temperature of the reductive metal but lower then its boiling point. The authors provide two tables which show the possible combination of IPCs that could be fabricated, Tables 2.1 and 2.2.

TABLE 2.1: Possible sacrificial oxides with corresponding metal reductive agents and the composition produced at 1273K.[30]

| Produced Composite | Molten Metal as Reductive Agent | Sacrificial Oxide as preform |
|---|---|---|
| $Al_2O_3$/Al | Al | CuO, NiO, CoO, MnO, $WO_2$, MoO, $TiO_2$, $SiO_2$, $Cr_2O_3$, $Fe_3O_4$, $Ta_2O_5$, $Nb_2O_5$, $NiCr2O_4$, $MgFe_2O_4$, $FeCr_2O_4$ |
| MgO/Mg | Mg | CuO, CoO, MnO, $SiO_2$, $Y_2O_3$, $UO_2$ |
| $NiAl_2O_4$/Al | Al | NiO |
| $CoAl_2O_4$/Al | Al | CoO |
| $MgFe_2O_4$/Mg | Mg | $Fe_3O_4$ |

TABLE 2.2: Possible combinations at a more elevated temperature of 2073 K.[30]

| Produced Composite | Molten Metal as Reductive Agent | Sacrificial Oxide as preform |
|---|---|---|
| $Al_2O_3$/Al | Al | NiO, CoO |
| MgO/Mg | Mg | CuO, CoO, MnO, $SiO_2$, $Y_2O_3$, $UO_2$ |
| $NiAl_2O_4$/Al | Al | NiO |
| $CoAl_2O_4$/Al | Al | CoO |
| $MgFe_2O_4$/Mg | Mg | $Fe_3O_4$ |

### 2.3.2 Transformation mechanism

A theory on the mechanism for the formation of interpenetrating networks from the Al-$SiO_2$ reaction has been explained by Breslin *et al.*[1], Figure 2.1. The theory goes as follows: (1) a thin layer of $Al_2O_3$ forms on the surface of the preform $SiO_2$ as it reacts with the molten Al. (2) Cracking occurs due to the volumetric contraction of approximately 35% of the $Al_2O_3$ phase. (3) The cracking creates channels for the molten aluminum to further penetrate the $SiO_2$ and continue the reaction. (4) The Si that is displaced diffuses away from the reaction front via the aluminum channels and into

the surrounding bath. (5) During cooling to room temperature the Si becomes supersaturated in the Al both in the composite and also in the surrounding bath, and it precipitates out of the melt. The final product is an alumina phase backed up by the aluminum phase. According to Breslin, this explains the transformation mechanism of co-continuous interpenetrating phase composites.

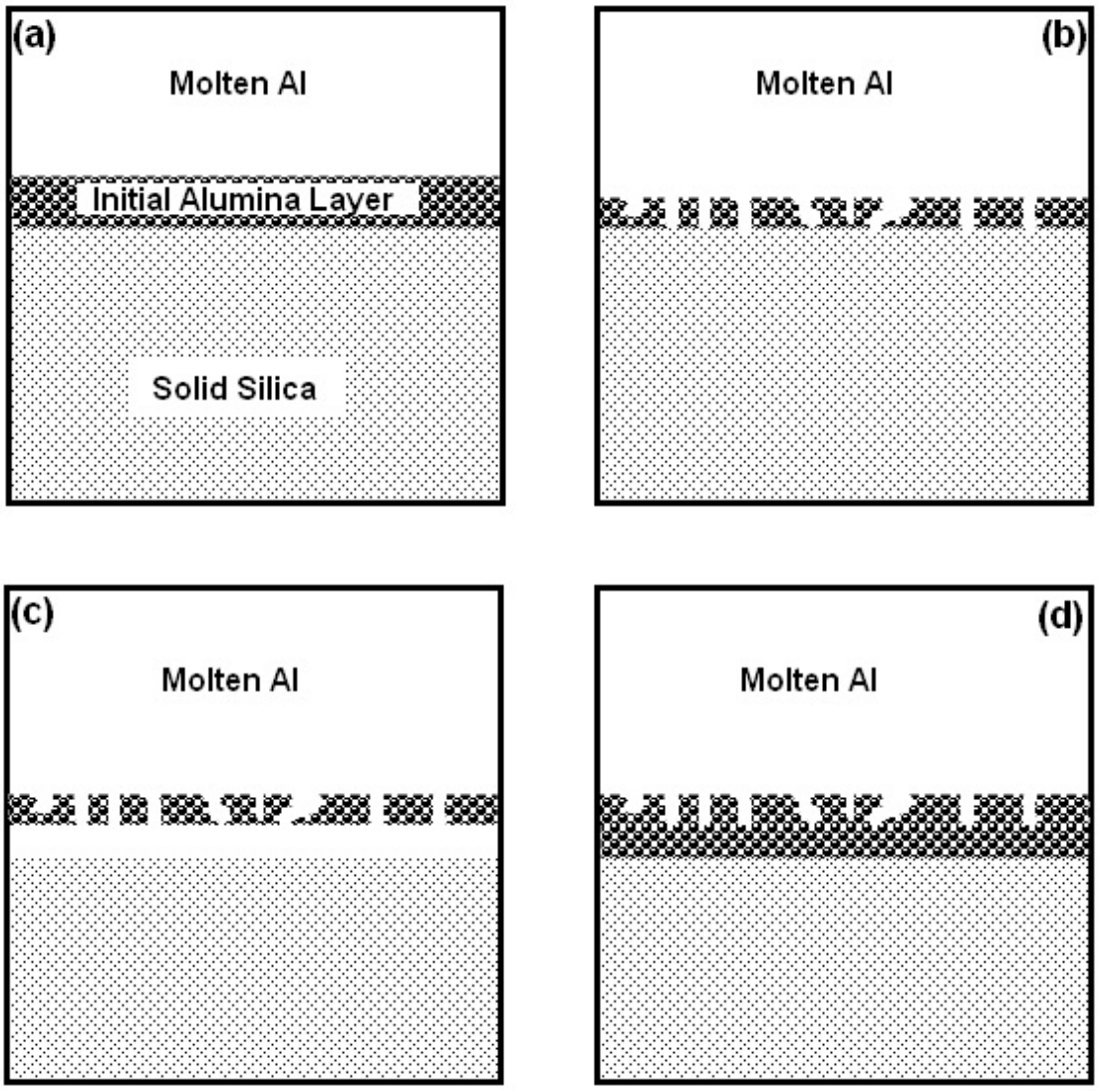


FIGURE 2.1: An illustration of Breslin's mechanism theory. (a) initial alumina layer is formed, (b) the alumina layer cracks due to its properties (c) molten aluminum fills the crack and propagates on (d) another front is created and the processes continues.

## 2.4 Alumina-Aluminum System

The alumina-aluminum system is the best studied ceramic-metallic IPC system as seen from the literature review. This particular system has been studied in depth by previous graduate students at Youngstown State University, mainly Ryan Paul[5] and Anthony Yurcho[11]. For completeness the next couple sections will be a short summary of Yurcho's findings, followed by an explanation where his research stopped and this study began. The first part of this thesis deals with the same material as Yurcho's study was based on.

### 2.4.1 TCON/RMP Process

The material used for this study was produced by the TCON process. The TCON process is a reactive metal penetration (RMP) process developed by Fireline Inc. located in Youngstown, Ohio. Their process is similar to the methods reported by George[23] and Breslin[1]. The process involves submerging a sacrificial oxide into a molten metal bath for a prescribed time. While submerged, a chemical reaction takes place and the metal reacts with the sacrificial oxide to produce a ceramic-metallic interpenetrating phase composite. For instance, clear fused quartz is submerged into a molten aluminum bath. The process results in a net-shape $Al_2O_3$-Al material based on the original sacrificial oxide. The Al and $Al_2O_3$ phases are interconnected throughout the material. The TCON method successfully produces ceramic-metallic IPCs. For more details on this process the reader is referred to Yurcho's thesis.[11]

Fireline experimented with adding alloying elements to the molten bath in order to change the composition of the inter-metallic phases. The capability of altering the RMP process allows Fireline to design, and produce, materials that have different properties than traditional ceramic-metallic composites. In this study, the addition of alloying Fe to the molten metal bath was investigated.

### 2.4.2 Fe-Additives to the $Al_2O_3$/Al system

As mentioned previously alloying elements can be added to the $Al_2O_3$-Al system which can alter the properties of the composite material. The effect of 7.5wt.% iron to the TCON process was studied in depth by Yurcho.[11] Using Fe as an additive increases the overall strength of the composite at elevated temperature. There are other advantages such as (1) Fe has a higher melting temperature than Al, (2) Fe has a lower affinity for oxygen than Al and will not interfere with the reaction of forming $Al_2O_3$, and (3) handling molten Fe is relatively easy and does not require special atmospheric conditions. Crystal structure and lattice parameters of the metal components involved in the present research are presented in Table 2.3.

TABLE 2.3: Crystal structure and lattice Parameters of Al, Fe, and Si

| Aluminum | Iron | Silicon |
|---|---|---|
| 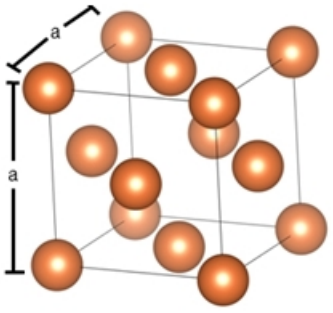 | 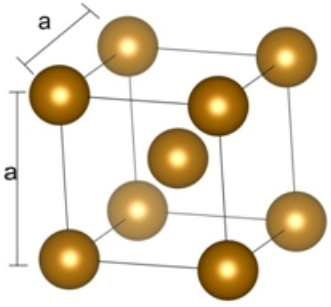 | 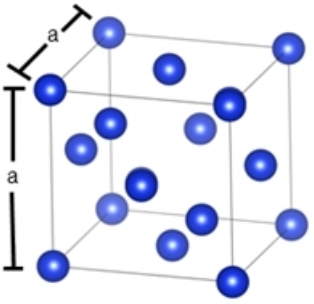 |
| $Fm\bar{3}m$ | $Im\bar{3}m$ | $Fd\bar{3}m$ |
| $a = b = c = 4.04958$Å | $a = b = c = 2.8665$Å | $a = b = c = 5.4310$Å |
| $\alpha = \beta = \gamma = 90°$ | $\alpha = \beta = \gamma = 90°$ | $\alpha = \beta = \gamma = 90°$ |

Based on the oxide/metal formation it is unlikely that the iron will react with the silica. The iron will most likely react with the Al and form a binary Al-Fe phase . Table 2.4 shows the common binary phases of Al-Fe. On the other hand, it is possible that the iron will react with the displaced silicon that is present within the Al and form a ternary Al-Fe-Si phase. Table 2.5 shows common Al-Fe-Si phases. This research was done to clarify which phases are formed when 7.5wt.% Fe is present in the molten Al.

TABLE 2.4: Crystal structure and lattice parameters of common Al-Fe and Al-Si binary phases.

| Phase | wt.%Al | wt.%Fe | wt.%Si | Space Group | Lattice Parameters (Å) |
|---|---|---|---|---|---|
| $Al_6Fe$[39] | ≈13 to ≈20 | ≈80 to ≈87 | 0 | $C$mcm | $a = 6.49$ |
| | | | | | $b = 7.44$ |
| | | | | | $c = 8.79$ |
| $\epsilon$[40] | ≈40 to ≈47 | ≈53 to ≈60 | 0 | - | - |
| AlFe[41] | 12.8 to ≈37 | 68 | 0 | $P$m$\bar{3}$m | $a = 2.895$ |
| $Al_5Fe_2$[42] | 53 to 57 | 43 to 47 | 0 | $C$mcm | $a = 7.65$ |
| | | | | | b = 7.41 |
| | | | | | c = 4.22 |
| $Al_{13}Fe_4$[37] | 58.5 to 61.3 | 38.7 to 41.5 | 0 | $C$2/m | $a = 15.49$ |
| | | | | | $b = 8.08$ |
| | | | | | $c = 12.48$ |
| | | | | | $\beta = 107.72°$ |
| (Al)[44] | 98.4 to 100 | 0 | 0 to 1.6 | $F$m$\bar{3}$m | $a = 4.04958$ |
| (Si)[44] | 0 to 0.01 | 0 | 99.99 to 100 | $F$d$\bar{3}$m | $a = 5.4310$ |

TABLE 2.5: Crystal structure and lattice parameters of common Al-Fe-Si ternary phases.

| Phase | at.%Al | at.%Fe | at.%Si | Space Group | Lattice Parameters (Å) |
|---|---|---|---|---|---|
| $Al_{4.5}FeSi$[45] | 69.2 | 15.4 | 15.4 | $A$2/a | $a = 12.404$ |
| ($\beta$ or $\tau_6$) | | | | | $b = 6.175$ |
| | | | | | $c = 20.813$ |
| | | | | | $\beta = 90.42°$ |
| $Al_{2.7}FeSi_{2.3}$[45] | 45.0 | 16.7 | 38.3 | $P$bcn | $a = 6.061$ |
| ($\delta$ or $\tau_4$) | | | | | $c = 6.061$ |
| $Al_2FeSi45$ | 50.0 | 25.0 | 25.0 | $C$mma | $a = 7.995$ |
| ($\tau_{23}$) | | | | | $b = 15.162$ |
| | | | | | $c = 15.221$ |
| $Al_2Fe_3Si_4$[45] | 22.2 | 33.3 | 44.4 | $C$mcm | $a = 3.6687$ |
| ($\tau'$) | | | | | $b = 12.385$ |
| | | | | | $c = 10.147$ |
| $Al_4Fe_{1.7}Si$[45] | 59.7 | 25.4 | 14.9 | $P6_3$/mmc | $a = 7.509$ |
| ($\tau''$) | | | | | $c = 7.594$ |
| $Al_6Fe_4Si_6$[46] | 37.5 | 25.0 | 37.5 | $P2_1$/n | $a = 7.179$ |
| ($\tau_8$) | | | | | $b = 8.354$ |
| | | | | | $c = 14.455$ |
| | | | | | $\beta = 93.80°$ |
| $Al_{63.5}Fe_{20.5}Si_{16}$[46] | 63.5 | 20.5 | 16.0 | unknown | $a = 17.78$ |
| ($\tau_7$ or $\gamma$) | | | | | $b = 10.25$ |
| | | | | | $c = 8.90$ |
| | | | | | $\beta = 132°$ |
| $Al_{15}Fe_6Si_5$[46] | 57.7 | 23.1 | 19.2 | $P6_3$/mmc | $a = 12.404$ |
| ($\tau_5$ or *alpha*) | | | | | $c = 2.6223$ |

### 2.4.3 Alloying Aluminum with Iron and Silicon

Figure 2.2 shows the binary phase diagram of aluminum and iron. With 7.5wt% iron and 92.5wt% aluminum this composition is characterized by the eutectic reaction L $\rightarrow$ Al+$Al_{13}Fe_4$.[37]

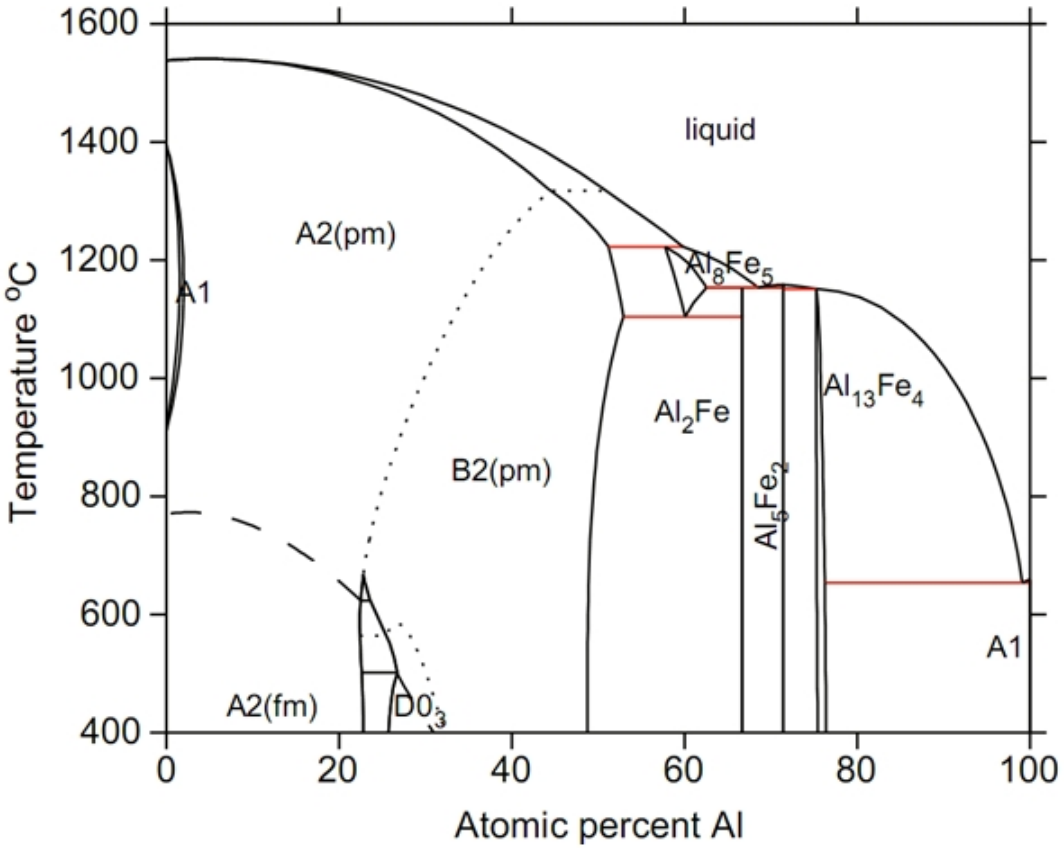


FIGURE 2.2: Binary Fe-Al phase diagram by Sundman *et al.*[37]

The phase diagram of Al-Fe-Si ternary system at 600°C is shown in Figure 2.3. Regarding the Al-Fe-Si ternary system, the only related research found in literature focuses on the effects of Fe and Si impurities during aluminum purification.[11] Commercially produced products have the following phases coexisting $Al_6Fe$, $Al_{13}Fe_4$, $Al_8Fe_2Si$, $Al_6FeSi$, $Al_4FeSi_2$, and Si.[37] Since the TCON process is a unique RMP it is hard to predict which

phase will be present. It is the purpose of the present research to do a complete characterize of the ternary Al-Fe-Si phases observed in Al-7.5 wt%Fe-based ICP using electron crystallography.

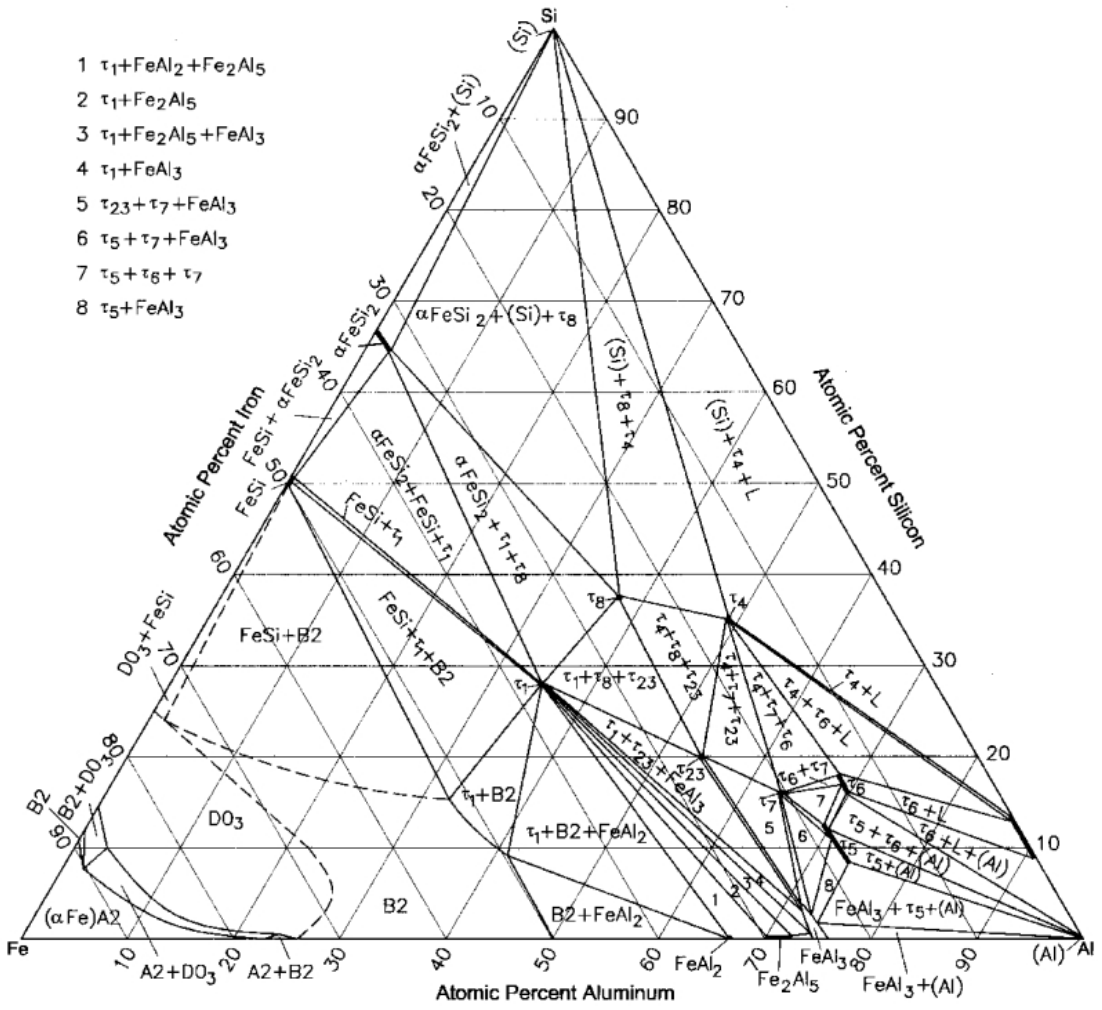


FIGURE 2.3: Al-Fe-Si Computed Phase Diagram at 600°C.[46]

### 2.4.4 Previously Obtained Results

This section will summarize the previous results that have been obtained in characterizing the TCON material.

## X-ray Diffraction (XRD) Results

XRD was the first step for the analysis. These results indicated which phases are present in the sample. This analysis was performed on the 7.5wt% Fe sample to figure out which phases were formed. XRD confirmed the presence of $Al_2O_3$, Al, and Si in the sample. Additional un-indexed peaks exist for the Al-Fe binary phase. There are numerous possibilities on indexing the peaks with different Al-Fe phases. At the time an $Al_{13}Fe_4$ (ICDD entry number 00-050-0797)[38] had been chosen tentatively as the best fit. In this thesis an attempt has been made to use electron crystallography in order to find out exactly which Al-Fe phase is in the composite material and to determine the crystallographic relationship with other phases.

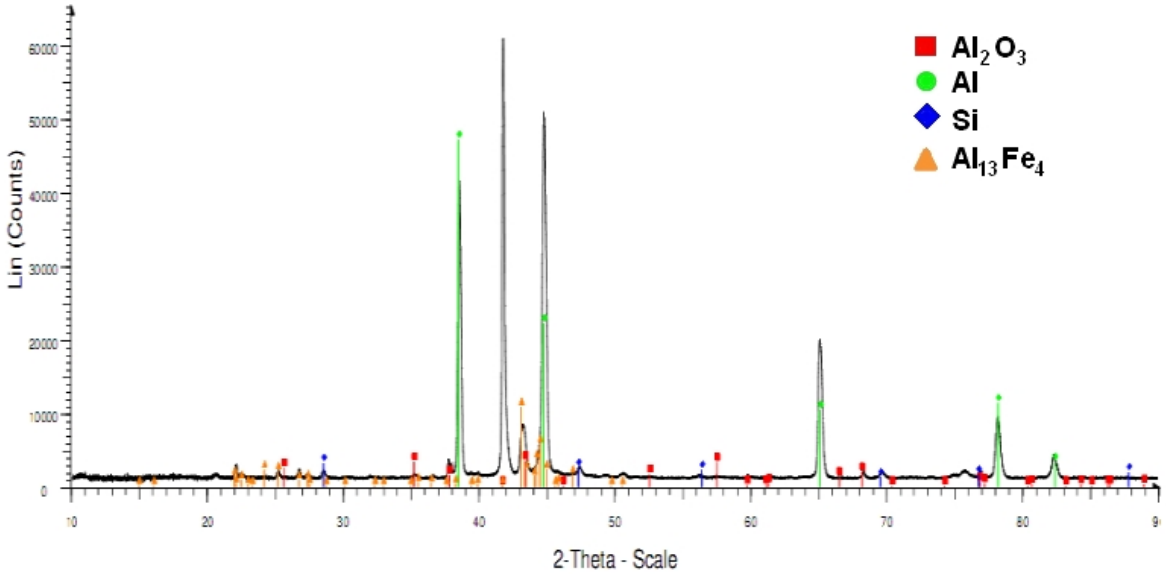


FIGURE 2.4: Powder XRD pattern from the Al-7.5wt.%Fe sample. The result shows the presence of $Al_2O_3$ (ICDD: 00-010-0173), trigonal,$R\bar{3}c$ , a: 4.758Å, c: 12.991Å)[62] and Al (ICDD: 00-004-0787), cubic $Fm\bar{3}m$, a: 4.049Å)[63]. The data also show the presence of small amounts of Si (ICDD: 04-001-7247, cubic $Fd\bar{3}m$, a: 5.429Å)[64] in both samples. The pattern suggests the presence of $Al_{13}Fe_4$ (ICDD: 00-050-0797), orthorhombic $Bmmm$, a: 7.751Å, b: 23.771Å, c: 4.034Å)[65], but other Fe-Al alloys showed similarly well fitting patterns.

## Energy Dispersive Spectroscopy (EDS) Results

Energy Dispersive Spectroscopy was used in order to confirm the XRD results and to obtain details on the material chemical compositions. EDS analysis located where the phases are and verified the XRD data as seen in Figure 2.5.

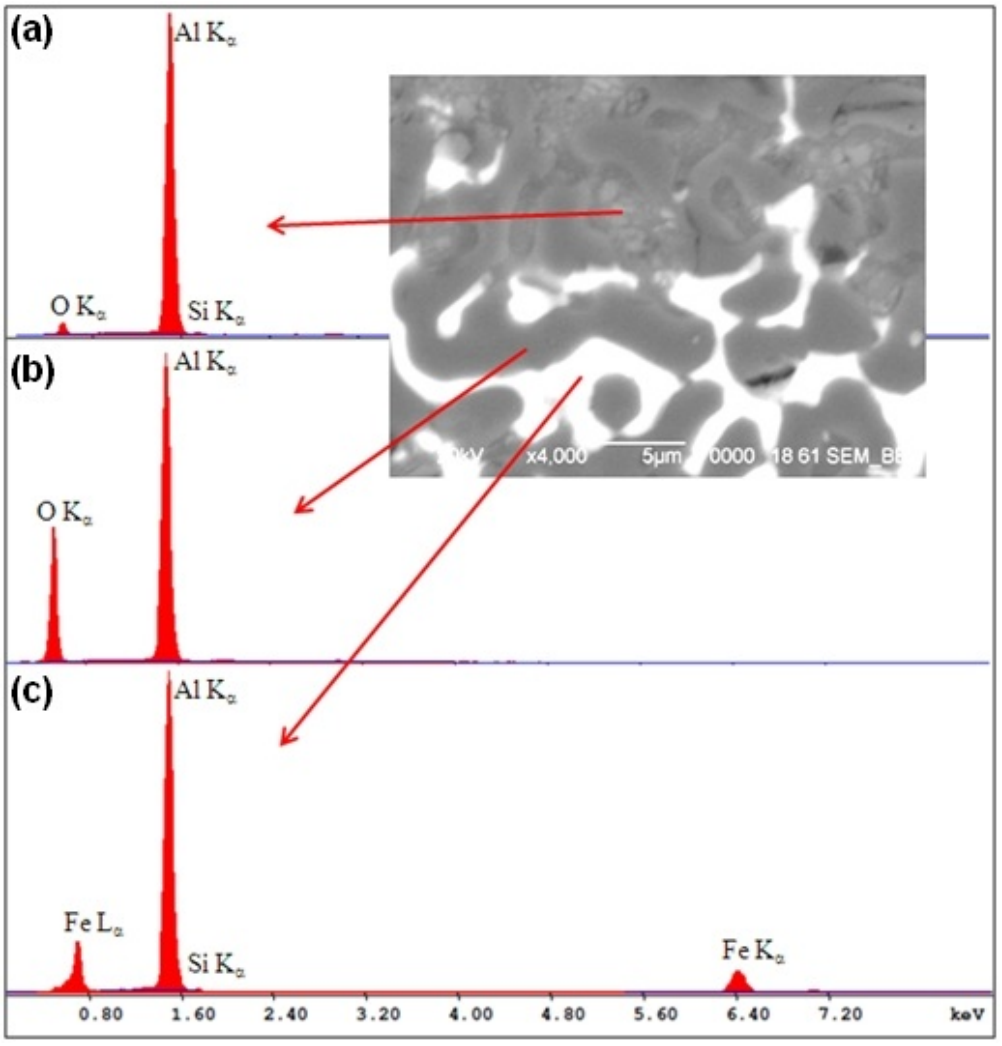


FIGURE 2.5: EDS spectra from the light gray (a), dark gray (b), and white (c) regions of the Al-7.5wt.%Fe sample. The characteristic X-ray peaks are indicative of (a) an Al metal phase, (b) an $Al_2O_3$ phase, and (c) an Al-Fe intermetallic phase, respectively. Trace amounts of Si are detected in the Al and Al-Fe spectra.[11]

## Mass and Thermal Properties

The mass and thermal properties of the Al, Fe, Si components and fused silica, and alumina compounds are presented in Table 2.6.

TABLE 2.6: Mass and thermal properties of selected compounds

| | Aluminum[37] | Iron[37] | Silicon[37] | Fused Silica[47] | 99.9%(Corundum) $Al_2O_3$[47] |
|---|---|---|---|---|---|
| Atomic/Molecular Weight | 26.91541 | 55.847 | 28.08 | 60.08 | 101.96 |
| Density ($g/cm^3$) | 2.6989 | 7.87 | 2.329 | 2.2 | 3.98 |
| Melting Point (°C) | 660.4 | 1538 | 1414 | 1665 | 2072 |
| Boiling Point (°C) | 2494 | 2870 | 3145 | 2230 | 2977 |
| Thermal Conductivity (W/m K) | 247 | 80.4 | 185.7 | 1.4 | 39 |

## 2.5 Nickel Oxide-Titanium System

As mentioned previously, other interpenetrating phase composite materials than Al-$Al_2O_3$ can be produced. An attempt has been made to synthesize a nickel oxide-titanium IPC system. Since this reaction is of the thermite type, the final phases are difficult to predict. The main objective is to obtain a NiTi-(Nitinol) phase present within the interpenetrating network. Nitinol is a shape memory alloy (SMA) that would add unique properties to the stiff ceramic matrix. The nitinol alloy combines the characteristics of shape memory materials and super-elasticity with excellent mechanical properties, wear resistance, and corrosion resistance.[48] Nitinol also exhibits high tensile strength and ductility.[49] In addition, SMAs are know to be excellent damping materials which makes them ideal for applications where large impacts might have to be absorbed. All these properties would be a great addition to an IPC material.

In this system the goal is to use NiO pellets as the sacrificial oxide and Ti as the molten metal reductive agent to produce an IPC that will contain ceramic, metal and possibly a NiTi shape memory alloy phase. The reaction can be summarized the in the following manner:

$$2NiO + Ti \rightarrow TiO_2 + Ni + ??NiTi?? \tag{2.4}$$

The question mark on the NiTi indicates the uncertainty of the presence of nitinol as a metal phase interpenetrating with the ceramic matrix. The formation of nitinol will be possible only if there is enough Ti left to combine with Ni. There are, however, a couple of obstacles that have to be avoided when melting Ti. The most challenging obstacle in producing an IPC with Ti is that Ti is very electro-positive and tends to be oxidized easily. This high affinity to oxygen creates a layer of $TiO_2$ on the metal surface which impedes the formation of a nitinol containing IPC. To avoid the initial reaction with oxygen the synthesis has to be carried out under inert gas atmosphere. Another challenge is to obtain a Ni-Ti phase following a NiO/Ti thermite reaction, taking into

account the extreme affinity of Ti for oxygen. Hence, the Ti will react with the NiO, and only if there is any metallic Ti left will it react with Ni to form NiTi. Experiments have to be carried out to find if the desired phases can be formed.

### 2.5.1 Literature

Liu and Köster[30] published criteria for formation of IPCs. Based on their paper, the use of NiO as sacrificial oxide and Ti as the reactive metal is possible. The justification for the possibly of a NiO-Ti system stems from the following three criteria, as follows:

(1) The produced oxide, $TiO_2$ must have a smaller volume than the sacrificial oxide, NiO. The volume calculation for both oxides involved in the reaction is presented below. The physical characteristics of the oxides are intoducted below and also summarized in Table 2.7.

$$A_{NiO} = 72.69 gmol^{-1} \qquad A_{TiO} = 79.87 gmol^{-1} \qquad \rho_{NiO} = 6.75 gcm^{-3} \qquad \rho_{TiO_2} = 4.23 gcm^{-3}$$

The following equations were used to compute the volume:

$$V_{2NiO} = \frac{A_{NiO}}{\rho_{NiO}} = 22.22 cm^3 \qquad V_{TiO_2} = \frac{A_{TiO_2}}{\rho_{TiO_2}} = 18.64 cm^3$$

Two moles of NiO would have a volume of $22.22 cm^3$, one mole of $TiO_2$ would amount to $18.64 cm^3$. The calculation shows that the first criterion is met because the sacrificial oxide has a larger volume than the produced oxide $TiO_2$. Shrinkage of about 16% is achieved while the $Al/Al_2O_3$ system experiences an approximate 35% volumetric contraction. It can be speculated that if the NiO/Ti system forms an IPC it will contain less metal due to a smaller volumetric contraction from the sacrificial oxide.

TABLE 2.7: Physical properties of Ti, Ni, NiO, $TiO_2$

| | Titanium[53] | Nickel[53] | Nickel Oxide(II)[53] | Titanium Oxide(IV) Rutile[53] |
|---|---|---|---|---|
| Molecular Weight (g/mol) | 47.88 | 58.69 | 74.69 | 79.87 |
| Density ($g/cm^3$) | 4.606 | 8.912 | 6.75 | 4.23 |
| Melting Point °C | 1668 | 1455 | 1955 | 1863 |

(2) The produced oxide $TiO_2$ must be more stable than the sacrificial NiO, i.e the Gibbs free energy must be more negative for $TiO_2$. Figure 2.6.

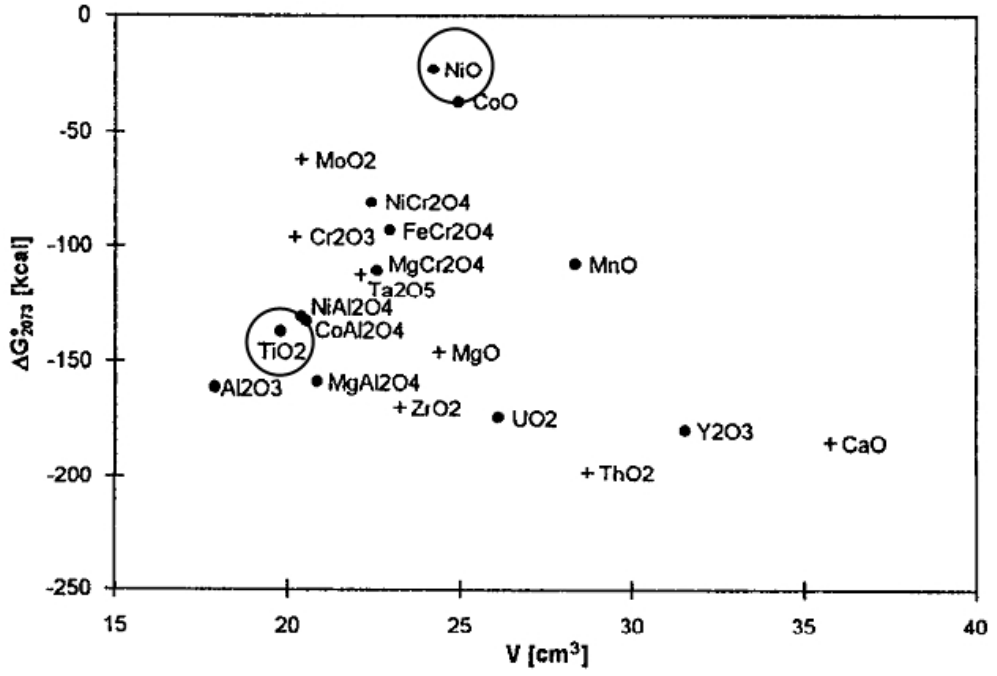


FIGURE 2.6: Diagram of Gibbs free energy as a function of volume for various ceramics. For a NiO-Ti reaction, the finally produced oxide $TiO_2$ must be more stable than the initial sacrificial NiO.[30]

(3) The processing temperature must be higher than the melting point of Ti and Ni but lower than their boiling points. Data obtained from Table 2.7.

$$1668°C < ReactionTemperature < 2732°C$$

Thus all the criteria are satisfied for the formation of a NiO-Ti system. Hence, the formation of such a system is theoretically possible.

In 2007, Kobayashi *et al.*[50] used a blend of NiO and Ti powders as a preform with molten Al in order to produce an IPC. The pre-form was heated to a range of temperatures in an induction furnace under $N_2$ atmosphere. Analysis was performed with XRD and SEM. Their objective was to use the titanium as an infiltration aid to cause a spontaneous infiltration of NiO with the molten aluminum. Using different Ti to NiO ratios the results were as follows: (1) spontaneous infiltration took place when the processing temperature was around 1100°C. (2) If the volume fraction of Ti was 25% or more the preform exploded. (3) At 1100°C and 15vol % Ti the phases $Al_3Ni_2$, $Al_3Ti$, and $Al_2O_3$ were obtained. Other results are mentioned such as the formation of $NiTiO_3$ at 1400°C and 15vol % Ti. The authors did not mention producing any NiTi phase. It would be expected that at least a ceramic "TiO" phase should occur since Ti is more electropositive than aluminum and it is more likely to react with O. The absence of such a phase seems to be related to the low reaction temperature of 1100°C, as, when a temperature of 1400°C was used, a $NiTiO_3$ phase formed. The author's intent was not to make an IPC from only NiO and Ti.

There have not been many studies done towards the production of a NiO-Ti based IPC system. The lack of research on this system makes it even more intriguing to investigate. Any successful fabrication of such a material would be useful for a variety of applications, in particular for high impact applications where good damping properties are required.

### 2.5.2 Shape Memory Alloys

In 1932, Olander observed the pseudoelastic behavior of an Au-Cd alloy. This was the first step towards discovering shape memory alloys. By the 1960s Buehler and his colleagues at the U.S. Naval Ordnance Laboratory discovered the shape memory effect in an equiatomic alloy of nickel and titanium, which can be considered as a breakthrough in the field of shape memory materials.[51] Following this breakthrough intense research was

devoted towards understanding and developing shape memory alloys as we know them today. The most widespread commercial use for shape memory alloys is in medicine.[51] Shape memory alloys exhibit two properties that are unique and would greatly improve the damping ability of a ceramic matrix.[52] These two properties are shape memory and superelasticity which will be introduced in the next sections.

### Shape Memory Effect

The equiatomic NiTi-Nitinol shape memory alloy exists in two different temperature dependent crystal structures called martensite (low temperature) and austenite (high temperature). The shape memory effect is demonstrated in the following manner, Figure 2.7. Initially the NiTi is in the low temperature martensite phase with individual grains of the material being highly twinned. Upon applying stress (i.e. deformation) the martensite phase of NiTi becomes a deformed martensite phase in which the macroscopic shape of the material is changed. In the process, the martensite phase partially or completely "untwins", which allows for a deformation without change to particle size or alignment of up to 8%.[51] (Figure 2.7) Heating the martensite phase above the transformation temperature will cause an atomic rearrangement into the high temperature austenite phase. At this point the original shape of the material recovers. When the austenite phase is left to cool the twinned martensite phase is obtained again, but no macroscopic change is observed. This phenomenon is called the one-way shape memory effect. The ability of shape memory alloys to retain a certain shape at high temperature and a different shape at low temperature is know as the two way shape memory effect.[51]

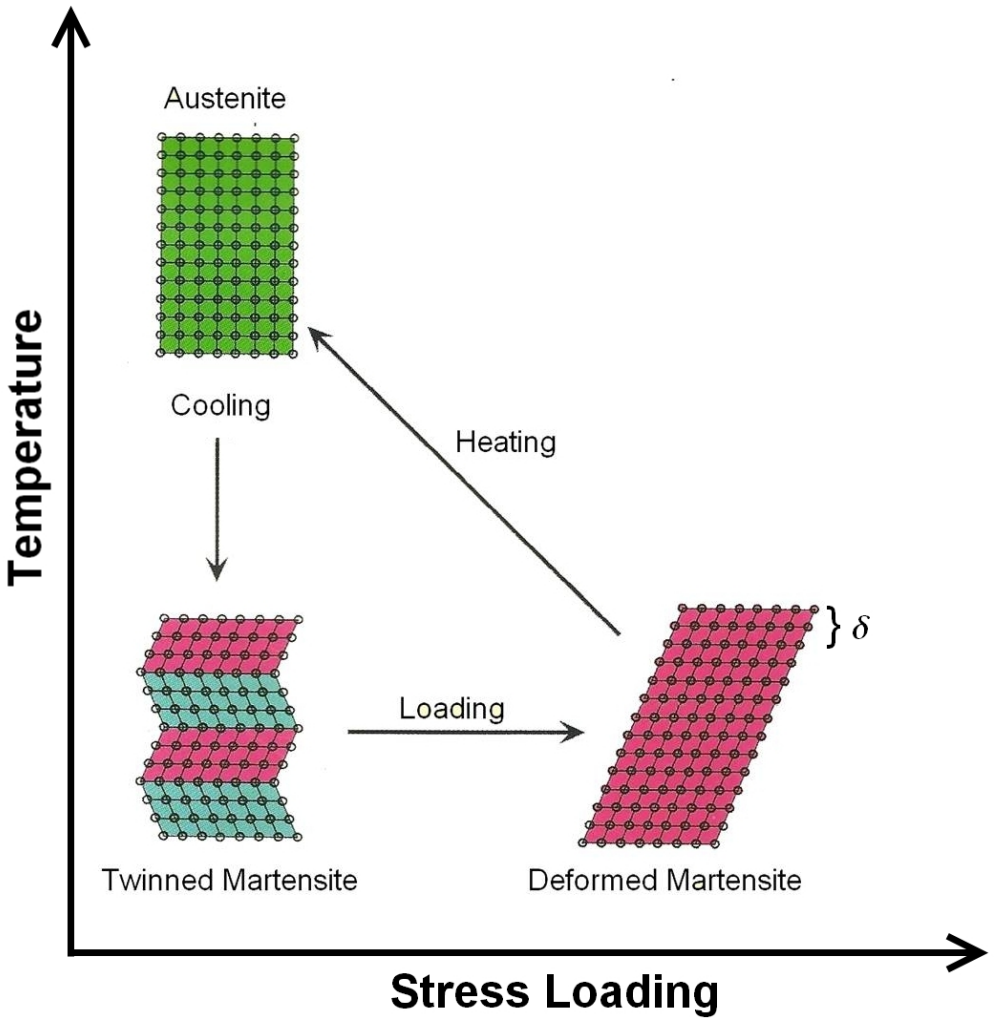


FIGURE 2.7: Inducing a stress loading on the twinned martensite phase will deform the martensite phase and results in an elongation of $\delta$. Upon heating the deformed martensite phase transforms into high temperature austenite phase and the original shape is recovered. As the material cools the twinned martensite is obtained but no further macroscopic change is seen.[66]

### Superelasticity

Superelasticity, also known as pseudoelasticity, refers to the ability of a shape memory alloy to be deformed, well above the proportionality limit and return to the original shape after the deformation stress is removed. Ordinary materials experience Hookian elasticity followed by irreversible plastic deformation. Conversely, shape memory alloys can be strained several times more due to the reversible rearrangement of the twins in

the martensite phase. By releasing the loading stress the material returns to its original shape, Figure 2.8. Deformation of the martensite phase is easy, as described for the SMA effect, and temporary stress induced transformation of the austenite phase into a martensite phase allows for extensive elastic deformation.[67] The extended recoverable deformation ability over ordinary materials allows shape memory alloys to absorb more energy, hence making shape memory alloys great damping materials.

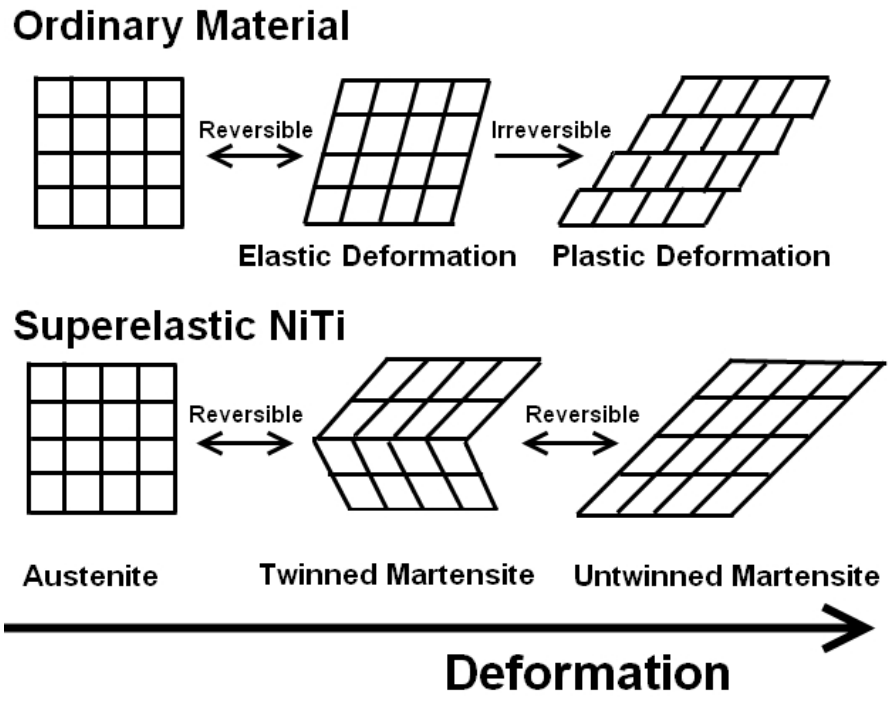


FIGURE 2.8: Schematic representation showing how ordinary materials compare to superelastic shape memory alloys. Upon loading and unloading the shape memory alloy deformation by twinning is reversible while the deformation of an ordinary material is non-reversible.[66]

Shape memory effect and superelasticity would be a great addition to a stiff ceramic matrix. Previous work with IPCs motivated the idea to combine shape memory alloys with a ceramic to obtain an IPC with unique properties. Ultimately the goal of this research is to obtain a nitinol NiTi intermetallic phase within a ceramic matrix.

To produce a nitinol (Ni-Ti) phase a precise ratio of Ni to Ti must be maintained. Figure 2.9 shows the phase diagram of Ni-Ti. It has been shown that in order to obtain a material that exhibits a shape memory effect a ratio of about 50 at.% nickel and 50 at.% titanium has to be present and the material has to be quenched from above 600°C[52]. After the processing of the shape memory alloy containing near-equiatomic NiTi phase material has to be annealed above the austenite transformation temperature in order for the phase to exhibit shape memory effects. The crystallographic information of Ni and Ti is presented in Table 2.8.

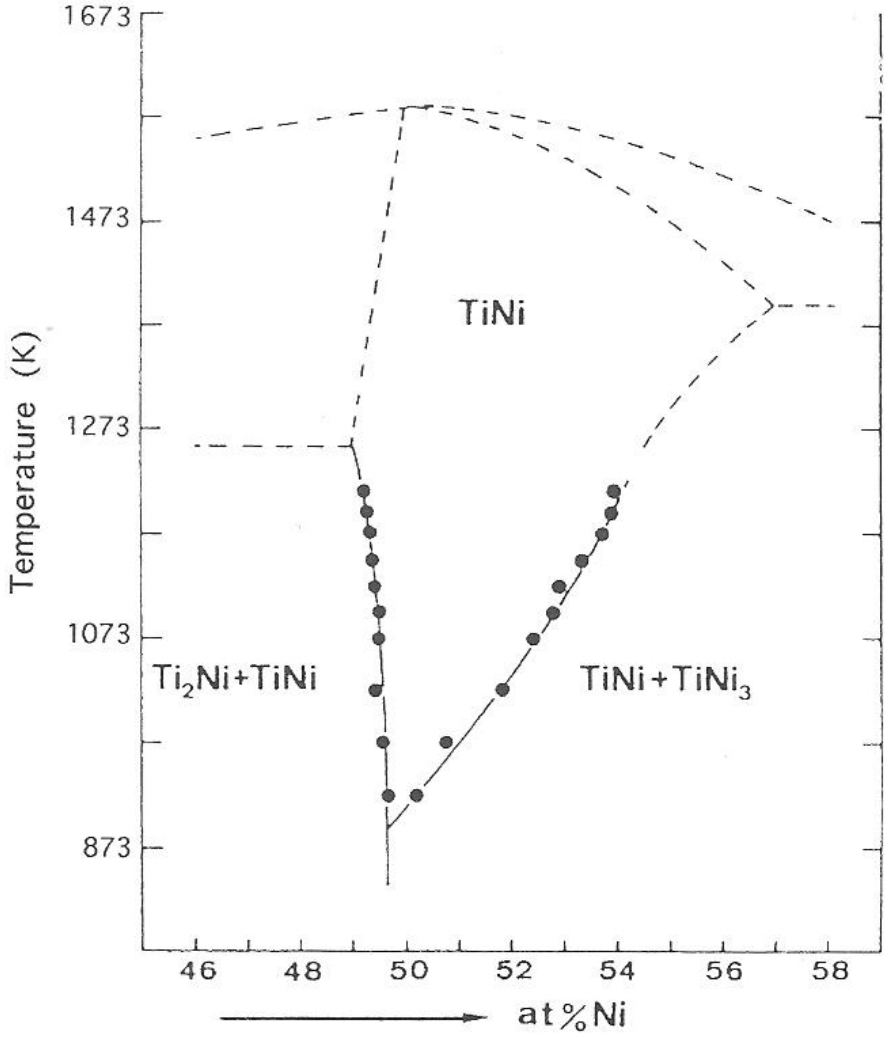


FIGURE 2.9: The component concentration requirement in order to obtain a NiTi phase. This is an equilibrium phase diagram; all these phases are present at room temperature.[51]

TABLE 2.8: Crystallographic structure of Ni and Ti metals.

| Titanium | Nickel |
|---|---|
| 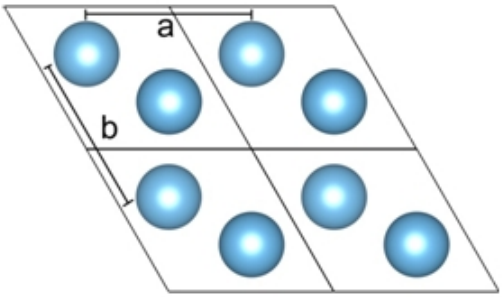  | 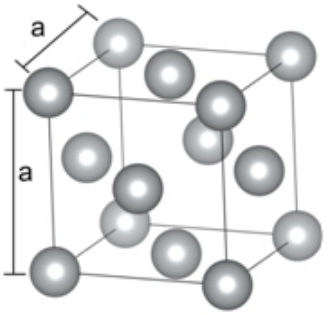  |
| $P6_3/\mathrm{mmc}$ | $F\mathrm{m}\bar{3}\mathrm{m}$ |
| $a = b = 2.9508$Å | $a = b = c = 3.524$Å |
| $c = 4.6855$Å | $\alpha = \beta = \gamma = 90°$ |
| $\alpha = 90°$ | |
| $\gamma = 120°$ | |

# Chapter 3

# Experimental

This chapter will explain materials synthesis, sample preparation techniques and it will give the rationale and details of the analytical methods used in the present research. The last two sections will be a short theoretical treatment on high resolution electron microscopy and electron diffraction.

## 3.1 Sample Acquisition and Sample Preparation

### 3.1.1 TCON Material

TCON materials were manufactured by Fireline, Inc., Youngstown, OH using their unique TCON RMP process. The samples for light and scanning electron microscopy investigations were prepared using metallographic techniques. Detailed sample preparation methodology is presented in previously published work by Anthony Yurcho, former YSU graduate student.[11] A Focused Ion Beam (FIB) was used to prepare TEM samples. Out of the four materials provided by Fireline (Table 3.1) this work focused on two of them. In Al-7.5wt.% Fe sample needed further investigating using TEM techniques to determine which phases were present within the bulk. In addition, an Al (2hr) sample which was only submerged for 2 hours in the molten aluminum bath and the sample was

only partially transformed. This sample would provide insight into the transformation mechanism. This work deals only with the second material listed in Table 3.1.

TABLE 3.1: Materials provided by Fireline, Inc.

| Name | Starting Material | Metal Bath | Transformation Time | Reaction Temperature |
|---|---|---|---|---|
| Al | Clear Fused Quartz | Pure Al | 6 hours | 1200 °C |
| Al-7.5wt.%Fe | Clear Fused Quartz | Al-7.5wt.%Fe | 4.63 hours | 1200 °C |
| Melt | Residual Al-7.5wt.%Fe alloy | N/A | N/A | N/A |
| Al (2hr) | Clear Fused Quartz | Pure Al | 2 hr | 1200 °C |

### 3.1.2 NiO-Ti System

Nickel oxide powder with a purity of 99.9999% (GFS Chemicals, Columbus, OH) was compressed at 1500 psi into a 5 mm thick pellet using a hydraulic laboratory press from International Crystal Company (IFC). Since the pellet was still in a powder form sintering was required to prevent later out-gassing of the pellet under vacuum which otherwise could damage the vacuum system or the pellet. Sintering was done at 1400 °C for 12 hours using a Thermolyne high temperature tube furnace. The phase composition of the powder and pellet were verified using XRD analysis to ensure purity and that no reaction took place between pellet and the ceramic furnace holder. Figure 3.1 shows an XRD pattern of a NiO pellet after sintering

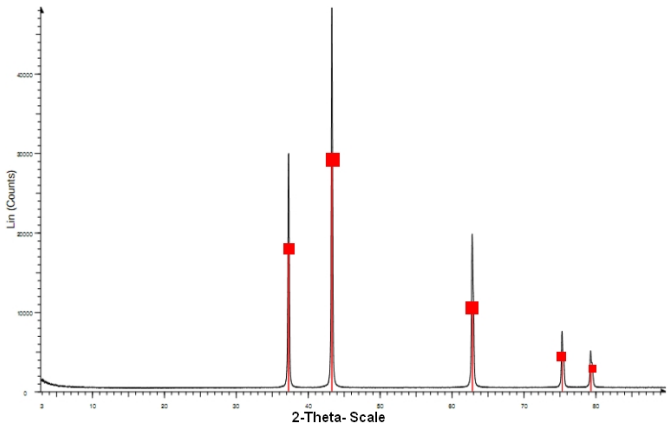


FIGURE 3.1: XRD pattern of a NiO pellet after sintering. The peaks correspond to Bunsenite NiO (ICCD: 00-047-1049, Cubic $Fm\bar{3}m$, a: 4.177 Å).

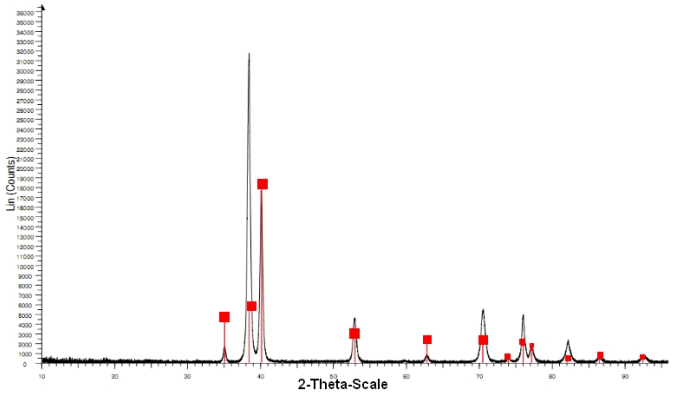


FIGURE 3.2: XRD pattern of a Ti metal slice. The peaks correspond to Titanium Ti (ICCD: 00-044-1294, Hexagonal, $P6_3/mmc$, a: 2.950 Å, c: 4.682 Å)

Titanium slices were cut using a Buehler IsoMet 1000 precision saw. A slice of Ti, about 2 mm thick, was placed on top of a sintered NiO pellet. The XRD spectra of Ti used in the experiment is presented in Figure 3.2. An Edmund Buehler, GmbH (Germany) mini arc melting system (MAM-1) was used to melt the Ti in order to react with the NiO pellet. The mini arc melting system was used for several reasons. Compared to aluminum Ti has a high melting point (1668 °C). The MAM-1 arc melting system can achieve 4000 °C. Small samples can be fabricated rapidly using this method. The main reason for using this system is its vacuum capabilities and inert atmosphere. As Ti reaches its melting temperature it tends to react with oxygen. Working under vacuum in combination with Ar purging is the easiest way to avoid unwanted Ti oxidation by atmospheric oxygen. The Mini Arc Melter MAM-1 uses roughing and turbo pumps that can evacuate the 1.1 liter chamber to about 1.0 x $10^{-4}$ mbar[54]. Before reaching the final vacuum the chamber can be purged with ultra pure argon gas 3-5 times to remove all traces of oxygen and ensure a completely oxygen free environment. Due to production of extreme temperatures the base plate of the furnace is water cooled to avoid melting the sample holder.

Upon melting of the Ti on top of the NiO pellet a reaction occurred. When the process was complete the sample was allowed to cool and then removed from the furnace. Next, the samples were cut using a precision low speed saw to expose a cross-section in order to

investigate the interior of the final product. After sectioning the material and exposing the cross section of the sample the two pieces were embedded in epoxy to create a large sample which is easier to handle during the polishing stage than the small pellet. Ted Pella epoxy was used in small copper cylinders and left to cure for 12 hours at room temperature. The various steps of the sample preparation are presented in Figure 3.3.

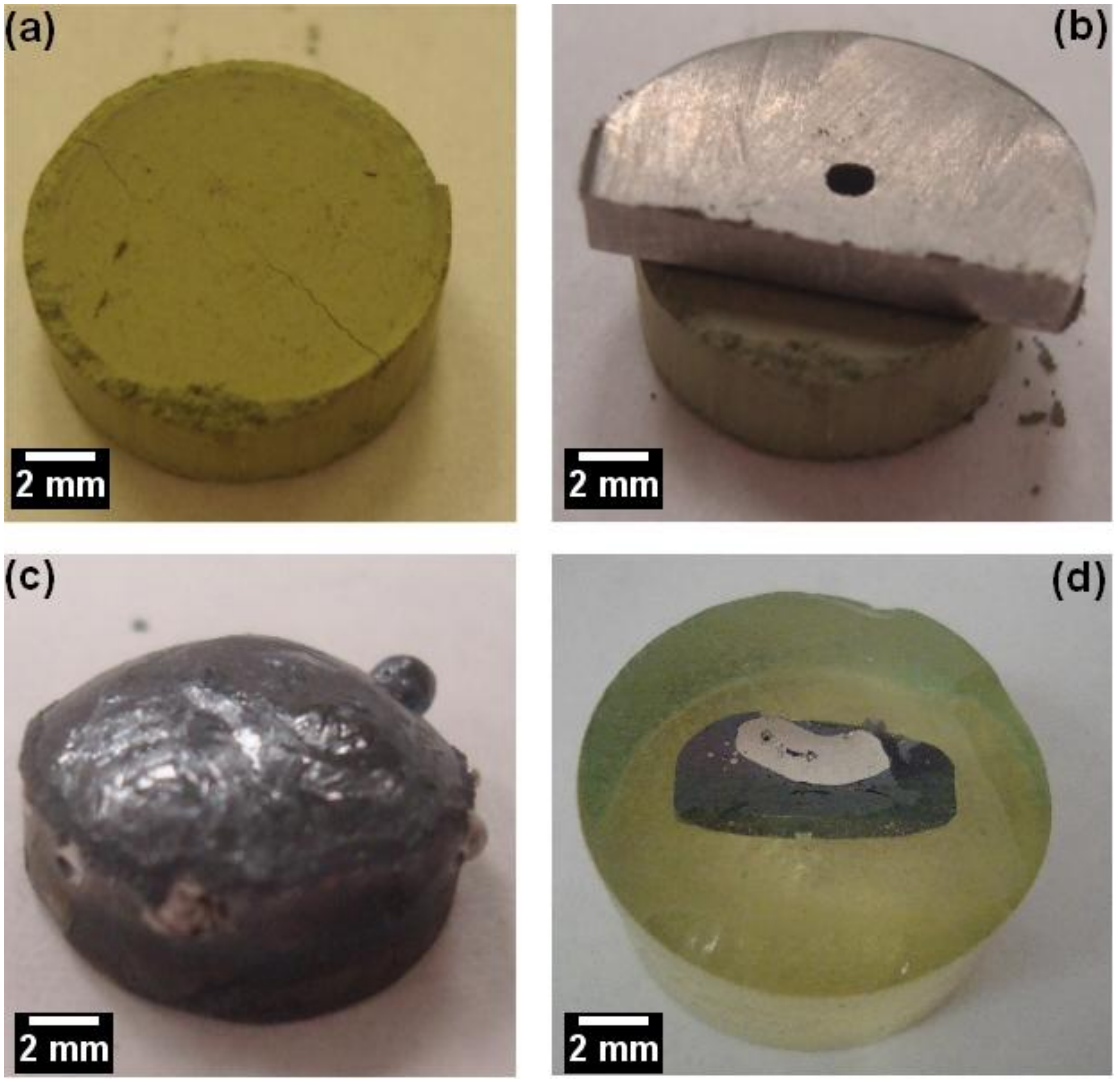


FIGURE 3.3: (a) NiO pellet after pressing and sintering. (b) A piece of Ti metal is placed on top of the NiO pellet to be reacted. (c) After reaction in the arc-melting furnace the pellet had a dome shape. (d) The transformed pellet was cross-sectioned and placed into epoxy for easier polishing and analysis.

The polishing stage is crucial for obtaining high quality microscopic data. In the first grinding step rough silicon carbide P#800 paper (from Struers) was used to remove any

bumps created during cross-sectioning of the sample. Next, silicon carbide P#1000 and P#1200 paper were used to remove any scratches induced by the rough P#800 paper. The sample was constantly rotated to avoid any single directional scratching by the silicon carbide paper. Fine polishing was performed using 3 micro-meter, 1 micro-meter, and 0.25 micro-meter pads in order to expose the microstructure. In between fine polish steps the sample was thoroughly washed with soap and water to remove any contamination left from the previous polishing step. Table 3.2 shows a summary of the polishing steps.

Table 3.2: Summary of Polishing Steps

| Step | Type | Lubrication |
|---|---|---|
| Grinding 1 | Struers Silicon Carbide P#800 Paper | Water |
| Grinding 2 | Struers Silicon Carbide P#1000 Paper | Water |
| Grinding 3 | Struers Silicon Cardide P#1200 Paper | Water |
| Polish 1 | Struers DP 3 micro-meter pad Struers | DP-Lubricant Blue |
| Polish 2 | Struers DP 1 micro-meter pad Struers | DP-Lubricant Blue |
| Polish 3 | Struers DP 0.25 micro-meter pad Struers | DP-Lubricant Blue |

Other pellets were prepared from 1:1 mixtures of NiO and $TiO_2$ powders. The mass of reacted Ti was also varied. Table 3.3 shows the different pellets-metal combinations used in the experiment.

Table 3.3: Trial pellets made

| Pellet # | Composition | Sintered hours @ Temp (°C) | Mass (g) | Mass of Ti reacted (g) |
|---|---|---|---|---|
| 1 | NiO | 14 @ 1400 | - | - |
| 2 | NiO | 14 @ 1400 | 2.0367 | 1.0636 |
| 3 | NiO | 14 @ 1400 | 2.4154 | 0.2218 |
| 4 | 50wt.% NiO 50wt.% $TiO_2$ | 14 @ 1400 | 2.1849 | 0.2613 |
| 5 | 50wt.% NiO 50wt.% $TiO_2$ | 14 @ 1400 | 2.4961 | 0.1261 |
| 6 | 50wt.% NiO 50wt.% $TiO_2$ | 14 @ 1400 | 2.8626 | 0.1430 |
| 7 | 50wt.% NiO 50wt.% $TiO_2$ | 14 @ 1400 | 2.5343 | 1.0218 |
| 8 | $TiO_2$ | 14 @ 1400 | 2.5913 | 0.4501 |

## 3.2 Instrumentation

### 3.2.1 Transmission Electron Microscopy

In the next sections some of the general principles of electron microscopy will be discussed. A basic introduction into the theoretical background of electron diffraction theory and high resolution electron microscopy simulation will be provided. The following transmission electron microscope (TEM) has been used in this study:

- JEOL JEM-2100 Scanning/Transmission electron microscope: 200 kV High Resolution TEM with maximum resolution of 0.23 nm, $LaB_6$ electron source. This microscope is equipped with an EDAX Genesis 2000 energy dispersive x-ray spectrometer.

A TEM is a complex and expensive scientific instrument, but its principles may be explained using a couple of simple ideas. First, there is an accelerator that generates a beam of high energy electrons. Next, there are electric and/or magnetic fields that act as lenses which help control the path of the electrons. An evacuated scattering chamber contains the sample. It is assumed that the electron beam is only slightly disturbed (i.e. scattered) when passing though the thin sample.

The electrons are produced by heating the source, which may consist of either tungsten, $LaB_6$, or a field emission gun. These electrons are then accelerated to their final energy. In most microscopes this energy ranges from 100 kV-400 kV. The wavelength of such electrons is a few picometers making this radiation ideal for microscopy at the atomic scale. Compared to light or even hard X-rays these electrons have much smaller wavelengths and can be easier steered and focused, hence electrons are ideal for an illumination source to be used in a microscope. Table 3.4 shows the energy and wavelength of electrons typically used in TEM applications. Relativistic corrections have been applied to the calculation of the wavelength since the ratio of the speed of the electrons and the speed of light is larger then half for 100 kV acceleration voltage.

TABLE 3.4: Energy with corresponding wavelength. Where v is the speed of the electrons and c is the speed of light.

| E(kV) Energy of electrons | $\lambda$(pm) Wavelength of electrons | $\lambda$ (Å) Wavelength of electrons | v/c |
|---|---|---|---|
| 100 | 3.70 | 0.0370 | 0.548 |
| 150 | 3.35 | 0.0335 | 0.587 |
| 200 | 2.51 | 0.0251 | 0.695 |
| 250 | 2.20 | 0.0220 | 0.741 |
| 300 | 1.97 | 0.0197 | 0.777 |
| 400 | 1.64 | 0.0164 | 0.828 |

Figure 3.4 shows a basic lens configuration of a TEM and ray diagram in imagining mode which is one of the main modes of operation of a TEM instrument. The use of the magnetic/electric lenses helps steer the beam along the desired path. These lenses make it possible to focus the beam. In order to focus the electron beam to a single point it is necessary to change the phase of the wave at different points along the wave-front and cause the wave to collapse onto a single point. For electrons, phase shift is accomplished by using specially shaped magnetic or electric fields that act as lenses. Magnetic lenses are more common and usually possess cylindrical symmetry. Since these lenses are not perfect there are errors in the control of the phase shift which results in imperfect focusing giving rise to lens aberrations.[55] The most common aberrations include astigmatism, spherical aberration, chromatic aberration, and coma.

The condenser lens system converges the beam to a minimal probe size. A small probe size is desired because it will yield better resolution. Since the electromagnetic lenses are far from perfect apertures are used to block highly divergent rays which carry imperfections such as spherical and chromatic aberrations. The beam rays that transmit through the sample encounter the objective lens (which is also known as the image forming lens) which brings together the scattered rays back to a cross-over. The objective lens is the most important lens and has its own aperture which blocks out beam impurities and creates better contrast in the image. As the beam travels further down the column it is projected using the projector lenses onto a phosphorescent screen on which it then can be viewed. Charged-couple device (CCD) cameras are used to record the image directly

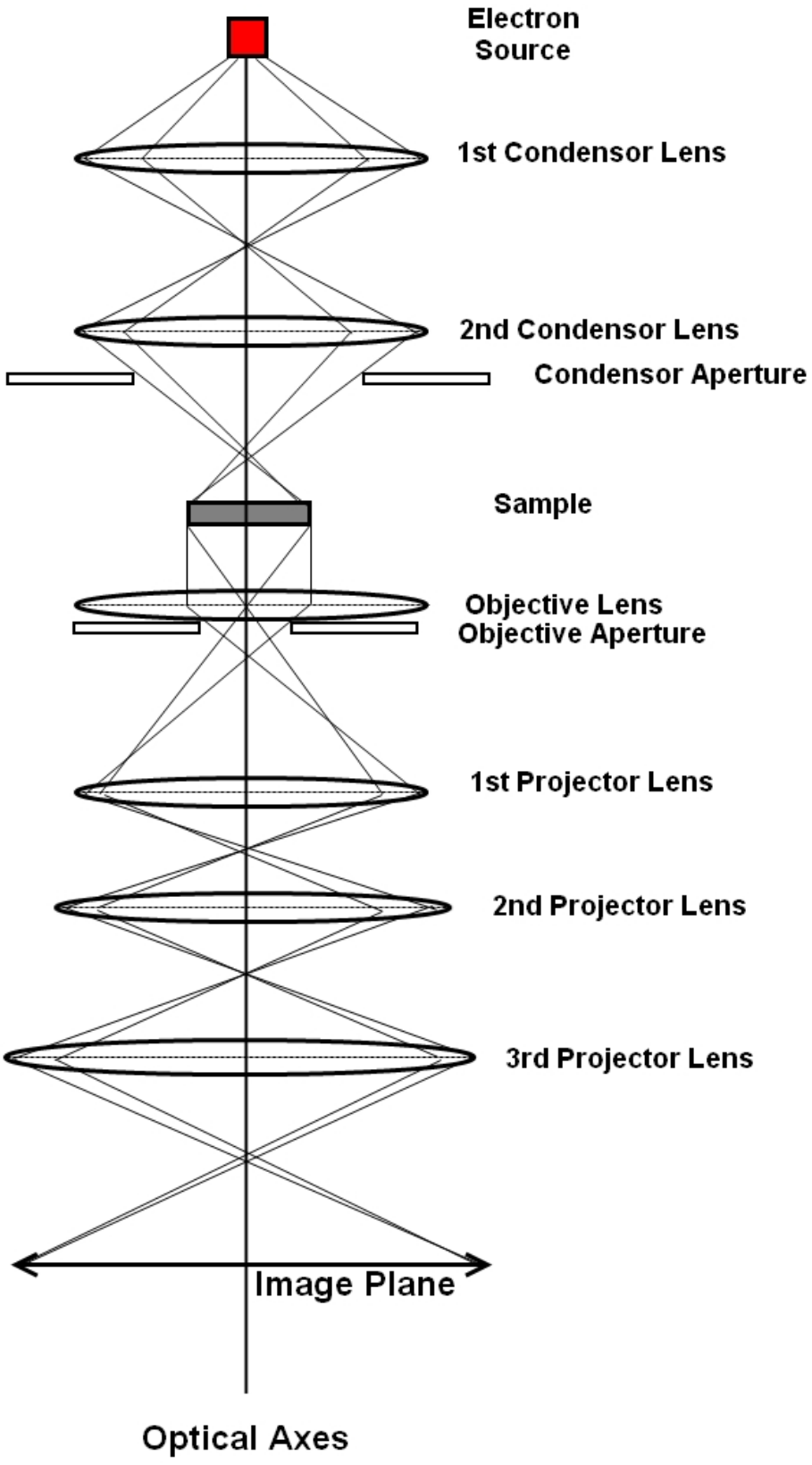


FIGURE 3.4: A typical ray diagram of a basic transmission electron microscope. Depending on the manufacture, some microscopes have extra lenses.

into the computer where it can be processed and stored. Charged- couple device cameras as used in common TEM systems record on a linear scale with a dynamic range from 12 to 16 bits.[56]

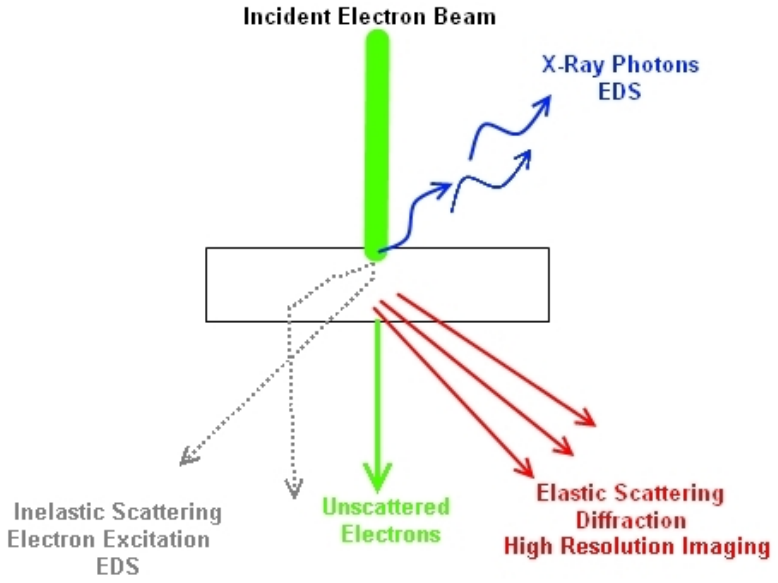


FIGURE 3.5: Interaction of the Incident Electron Beam with the sample. This figure is simplified and only the most important signals are shown here.

When the electron beam interacts with the sample numerous signals are created, as shown in Figure 3.5. These signals allow for elemental analysis, imaging, and diffraction. The electron has both wave and particle properties (wave-particle duality). Since the electron behaves as a wave as it moves through the solid, wave mechanics must be used in order to predict all the properties of the interactions. A general electron-solid interaction can be obtained by using this wave quantum mechanics approach. When an electron passes through the lenses and sample in the TEM, it interacts with the atoms and magnetic fields via electromagnetic forces. For example, the nucleus of an atom creates an electrostatic potential which can change the velocity of the passing electron (scattering). The total energy of the particle can then be written as the sum of a potential energy and a kinetic energy term.

$$E_{tot} = E_{kin} + V \tag{3.1}$$

Schrödinger hypothesized that, in the presence of a potential, a wave equation could be written based to the energy conservation law.

$$-i\hbar\frac{\partial\psi(x,t)}{\partial t} = -\frac{\hbar}{2m}\nabla^2\psi(x,t) + V(x,t)\psi(x,t) \tag{3.2}$$

This is the time dependent Schrödinger equation for a non-relativistic particle moving through a potential. Notice that it is a complex differential wave equation and that the equation as shown is the non-relativistic formulation which is only an approximation since the electrons do travel at least at 50% of the speed of light in a TEM microscope; a relativistic formulation is thus necessary. The collision of electrons with atoms in a crystal is a quantum mechanical many body problem. A detailed description of the underling physics that take place in an electron microscope can be found in numerous books and will thus not be covered here any further. A clear and concise description is provided for example by Cowley.[57]

The JEOL JEM-2100 was utilized to its full capabilities in this thesis. This model comes equipped with scanning transmission electron microscope (STEM) capabilities. Both modes, TEM and STEM, were employed. Techniques such as brightfield, darkfield, high resolution, diffraction, and x-ray energy dispersion spectrometry (XEDS) were utilized. All of these techniques were combined in order to fully characterize each sample.

## 3.3 Electron Crystallography

For crystalline materials all atoms are arranged in a symmetrical pattern with a base motif that repeats according to symmetrical operations. After applying all valid symmetry operations and permutations in three-dimensional space it gives rise to 230 space groups distributed over 14 space lattice and 32 point group symmetries. These space groups and point groups can be categorized into 6 crystal families, which are defined by

three lattice vectors and the angles between them.[59] Table 3.5 shows the distribution of Bravais lattices, point groups, and space groups according to the crystal system.

TABLE 3.5: List of crystal systems with corresponding unit cells.

| Crystal Family | Bravais lattices | Point groups | Space groups | Unit cell |
|---|---|---|---|---|
| Triclinic | 1 | 2 | 2 | $a \neq b \neq c$<br>$\alpha \neq \beta \neq \gamma$ |
| Monoclinic | 2 | 3 | 13 | $a \neq b \neq c$<br>$\alpha = \gamma = 90^\circ \neq \beta$ |
| Orthorhombic | 4 | 3 | 59 | $a \neq b \neq c$<br>$\alpha = \beta = \gamma = 90^\circ$ |
| Tetragonal | 2 | 7 | 68 | $a = b \neq c$<br>$\alpha = \beta = \gamma = 90^\circ$ |
| Trigonal/<br>Hexagonal | 2 | 9 | 52 | $a = b \neq c$<br>$\alpha = \beta = 90^\circ, \gamma = 120^\circ$ |
| Cubic | 3 | 5 | 36 | $a = b = c$<br>$\alpha = \beta = \gamma = 90^\circ$ |
| Total | 14 | 32 | 230 | - |

The Bravais lattices can be seen in Fig 3-6. These lattices are a nice visual tool to be able to image the unit cells of each crystalline compound.

The structure of crystalline materials will always exhibit one of the crystal systems shown above[1]. The parameters of the three lattice vectors and angles between them are unique to every crystalline compound or phase.

Besides imaging, the transmission electron microscope can be used as a diffraction instrument. In a TEM high energy electrons are scattered (i.e. electrons accelerated by a potential greater than 50kV).[58] The electrons are scattered at small angles as a result of the strong electron-matter interaction. In fact, the interaction is approximately 104 times larger than for X-rays. Much like X-ray and neutron diffraction, electron diffraction is a technique used to reveal the array of atoms in a solid and expose the symmetry of the structure. By using electron diffraction, the diffraction pattern can help indentify a phase by matching the pattern to known lattice parameters. The electron diffraction patterns are obtained by using the TEM. There are two kinds of diffraction patterns, (1)

[1]Exception: Quasi crystalline materials, incommensurately modulated compounds.

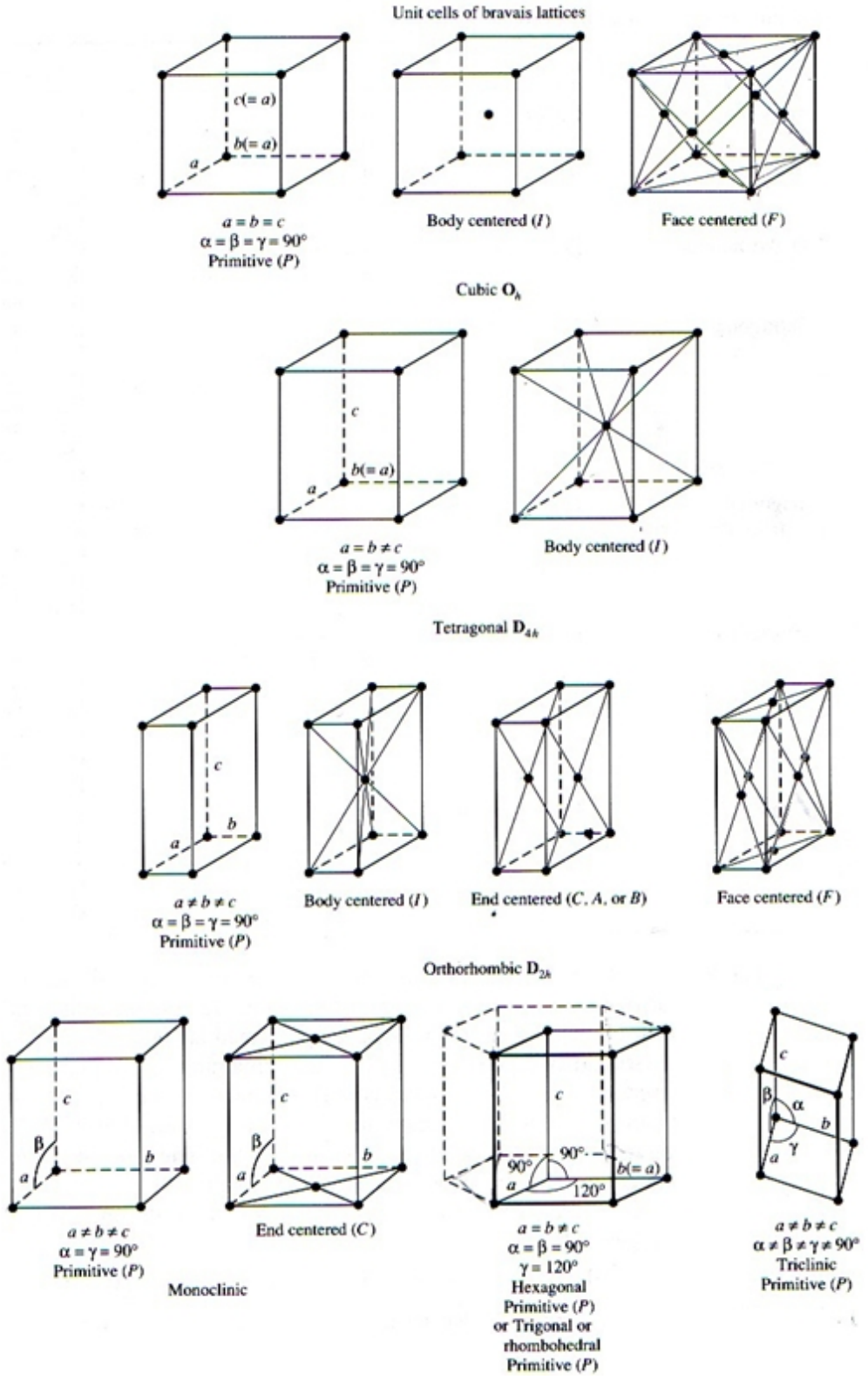


FIGURE 3.6: Bravais lattice with the corresponding crystal system.[55]

convergent beam electron diffraction (CBED) patterns and (2) selected area diffraction (SAD) patterns. The main difference is that CBED patterns can provide more information on the symmetry of the crystal. For a full theoretical treatment of the subject the reader can refer to William and Carter.[55] In this thesis, selected area diffraction was used to determine the structure of phases and to find orientation relationships between phases.

### 3.3.1 Selected Area Diffraction Patterns and jEMS Software

A diffraction pattern is a two-dimensional projection of a three-dimensional periodic lattice of the crystal structure, Figure 3.7. After being projected some information is extracted with defined operations. For example, the spacing of the diffraction spots is inversely proportional to the structure periodicity. Therefore, if the spacing between lattice points is doubled, the spacing on the diffraction spots is halved. The angles depend on which type of lattice it is but are usually not preserved under the projection. As a result, the diffraction pattern is known to be in reciprocal space because of its inverse relationship to the direct crystal lattice. When the pattern is recorded on a CCD camera it consists of bright spots on a dark background. Each spot corresponds to a lattice plane. When a number of planes are parallel to a single direction, it is known as a zone axis or zone direction. Therefore, the sample is tilted until a zone axis is found and a pattern is taken. Miller indices are conventionally used to define the direction with three numbers [hkl]. A more in-depth explanation is provided by P.E. Champness.[60]

Today SADP is still one of the most important TEM modes used by material scientists to help identify crystallographic phases of small volumes. It is very simple to obtain a SADP and for highly symmetrical systems it is quite easy to index the pattern. However, indexing less symmetrical patterns can be challenging and therefore the jEMS software package was used to help indexing these more difficult patterns. JEMS was created by Stadelmann[58] at the Ecole Polytechnique Federale de Lausanne in Switzerland. This software package is very useful not only for indexing diffraction patterns but also for

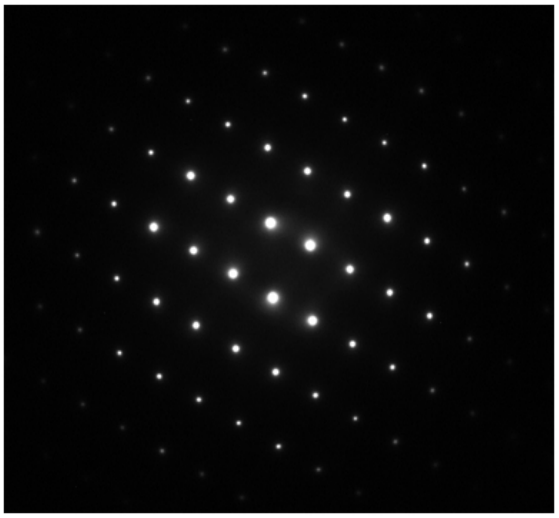

FIGURE 3.7: A typical electron diffraction pattern. This pattern is from an aluminum grain.

simulating high resolution images, which will be discussed in the next chapter. Most of the phases seen in this study had complex diffraction patterns thus the use of the software was useful for both time and simplicity considerations.

One of the most useful features of selected area diffraction patterns (SADP) is the ability to find a crystallographic relationship between two phases which is described by parallel directions and parallel planes of the phases. This process is known as finding an orientation relationship (OR). Orientation relationships are described in terms of parallel directions in a pair of parallel planes.[60] The following steps are taken in obtaining an OR: (1) The sample is tilted until one of the phases is on a major zone axis. (2) A diffraction pattern is obtained from that phase. (3) Without tilting the sample, the sample is moved to the second phase where a diffraction pattern is obtained. (4) Next, a diffraction pattern is obtained in an area between the two phases so that spots from both phases appear in the diffraction pattern. (5) Lastly, the patterns are indexed and the parallel directions and planes are found. This procedure was used in the study of the TCON material to find ORs in the composite material. These relationships can help explain how well two phases match geometrically by considering the unit cell of each phase. Consequently, a model can be constructed to show how well these phases match

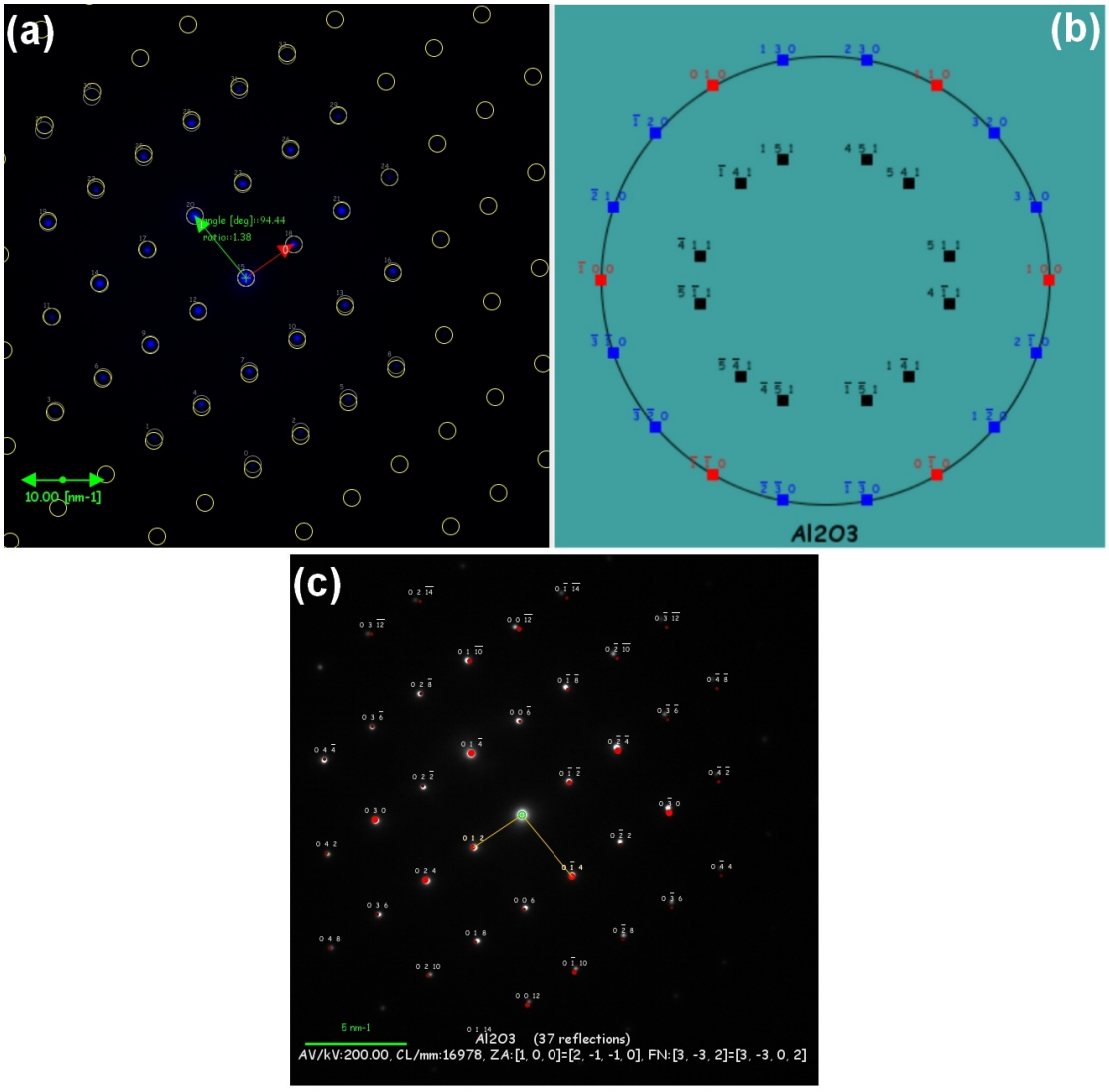


FIGURE 3.8: (a) The pattern is masked by selecting two non collinear points and by scaling the pattern; the ratio and angle between the two vectors is displayed by the software. (b) The pattern is indexed and possible matches are shown on a stereograph. (c) The possible matches are explored to see if the pattern matches a known phase.

geometrically. Visualization for Electronic and Structural Analysis (VESTA) software was used to create a model of the structures.

## 3.4 High Resolution Electron Microscopy

Whereas the diffraction pattern data results in a two-dimensional projection of a reciprocal lattice, high resolution electron microscopy results in a real space image. An image can be loosely defined as a one-to-one correspondence between points in the object and points in the image. Hence, an image replicates the real structure of the object. The electron wave that exits the sample is called the exit surface wave function. Ideally, an enlarged copy of the exit wave function is reconstructed. The lenses are used to recombine the exit wave functions to form an image. When the lenses recombine the exit wave further phase changes occur. Hence, it is impossible to distinguish which spots in the image are actual atom positions and which are free space. In other words, not every intense spot in the image corresponds to an atom position. A relationship, called the contrast transfer function (CTF), is developed between the exit wave and the final image wave. The CTF function includes defocus and aberration parameters of the microscope which are highly nonlinear. Consequently, methods have been developed to simulate high resolution images according to the CTF to determine the precise position of the atoms. Two well known methods are the Bloch waves method and the multislice method. The multislice method was used in this thesis to confirm the atom positions of high resolution images and will be explained in more detail in the next section.

$$\sin\left(\chi(u)\right) = -\sin\left(\frac{\pi}{2}C_s\lambda^3u^4 + \pi\lambda\Delta f u^2\right) \tag{3.3}$$

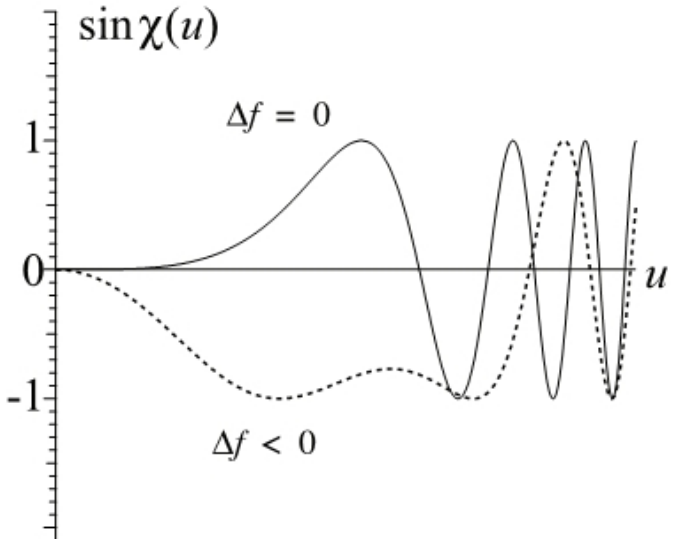


FIGURE 3.9: A typical contrast transfer function which depends on the defocus and aberration parameters of the microscope as seen in equation above.

### 3.4.1 Multislice Method

The Multislice method is a procedure to simulate high resolution TEM images. As the name implies a three dimensional object is sliced into an infinite number of two-dimensional layers that approach zero thickness and then integrated over all slices to determine the behavior of the exit wave. Since the beam will interact with each slice in sequence and the beam interaction for a single slice can be calculated a result can be obtained by summation of all the interactions. Hence, integration is required to determine the interaction for the whole sample. Figure 3.10 shows a pictorial illustration on how the multislice method works.

Keep in mind that all simulation methods solve the Schrödinger wave equation (Equation 3.2) using some numerical method to predict how the electron will move inside the sample. The multislice method is based on the physical optics theory of Cowley and Moddie.[56] This method uses numerical integration to solve Schrödinger's wave equation. The Schrödinger wave equation is a first order differential equation after appropriate assumptions are made. The equation can be integrated numerically by cutting the sample into many thin slices perpendicular to the beam. The propagation through

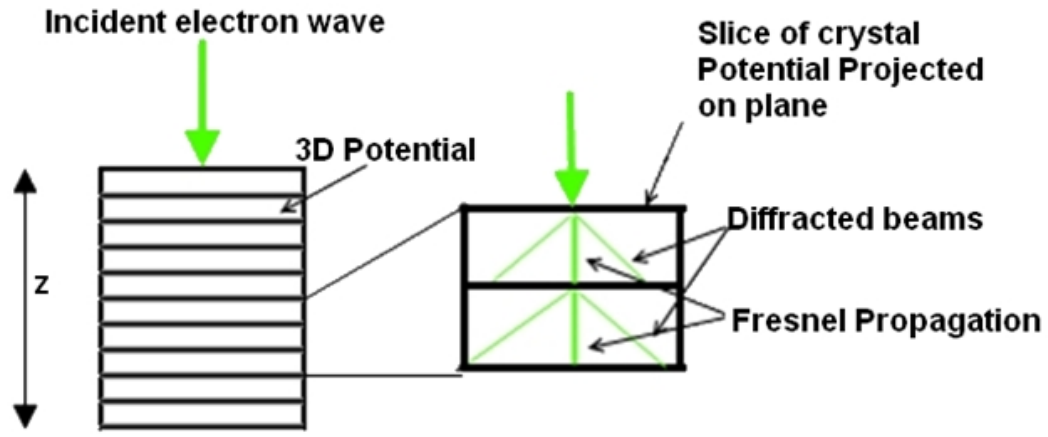


FIGURE 3.10: The multislice method. The 3-D potential is integrated in the z-direction in order to obtain a 2-D potential. Then the incident electron wave is multiplied by the 2-D potential and propagated until reaching the next 2-D potential. This process is repeated until the last slice is reached and the exit wave function is obtained.

each slice is done in two steps. First there is diffracted transmission where the incident wave function is multiplied with the crystal potential in real space. Secondly Fresnel propagation occurs in reciprocal space where a Fourier transform is taken of the wave function and is multiplied by the Fourier transform of the Fresnel propagation.[56] The first step is performed to obtain the interaction between the electron beam and the crystal potential. Then the second step explains the propagation of the electron beam to the next slice. This is a brief explanation of the multislice method. A more in-depth explanation is covered in Koch's PhD thesis.[56]

The jEMS software was used to simulate high resolution images using the multislice method. All the technical calculations are hidden from the user. The only input needed are the parameters of the microscope and the crystal information. The user must also select a range for the thickness and defocus. Then the jEMS software produces a thickness versus defocus map for the user to compare to the high resolution image obtained from the microscope. By doing so the image simulation helps locate precise atom positions. Image simulation was done on all high resolution images in this thesis.

# Chapter 4

# Results

## 4.1 TCON Material

### 4.1.1 Introduction

The results in this chapter will be presented in the following manner. Preliminary analysis will show the regions the TEM samples were prepared from. In the next section phase assignment is going to utilize electron crystallography in order to identify unknown Al-Fe and Al-Fe-Si phases. After all the phases were assigned and identified, orientation relationships were taken and will be reported accordingly. The characteristics of the silicon inclusions in the samples will be discussed. Lastly, HREM data for the TCON materials will be presented. These results will help to further the knowledge on the composite materials that Fireline TCON is manufacturing.

### 4.1.2 Preliminary Analysis

Electron transparent samples for TEM analysis have been prepared from TCON material using Focused Ion Beam (FIB) techniques. Figure 4.1 shows from which area TEM samples were prepared. Three distinct regions can be identified in a typical Al-Fe TCON

sample: (1) $Al/Al_2O_3$, (2) $Al\text{-}Fe/Al_2O_3$, and (3) Si. Samples from each region were prepared in order to be investigated, as indicated in Figure 4.1 (b) The main objective is to clarify the chemical composition and crystallographic structure of the unknown Al-Fe and Al-Fe-Si phases. After each phase has been assigned and indentified the next task is to find unique orientation relationships between the phases and lastly the silicon particles were investigated.

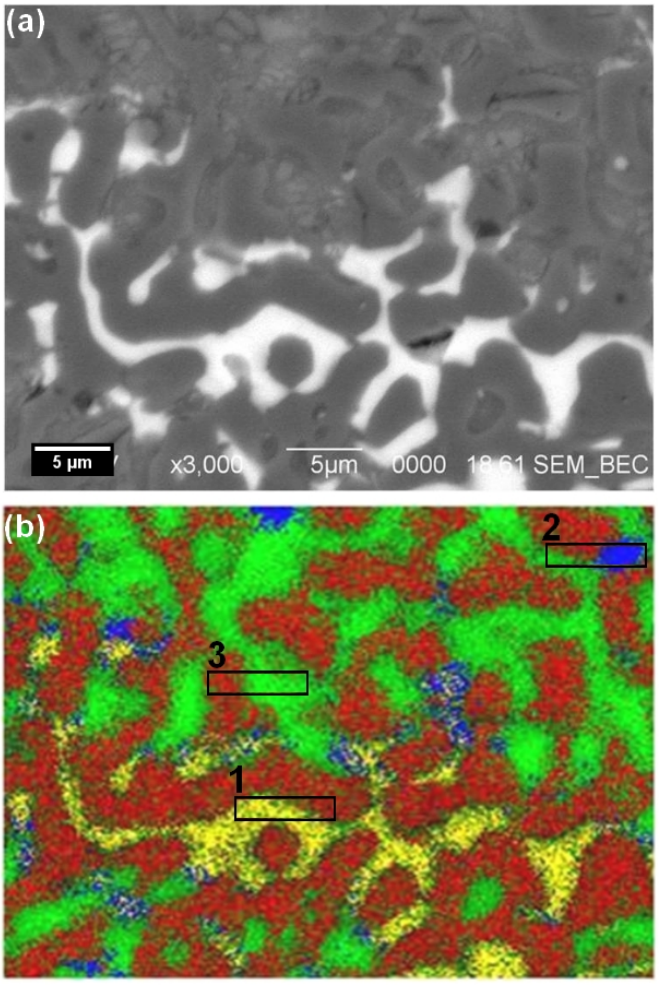


FIGURE 4.1: (a) Backscatter electron micrograph of a cross-sectioned TCON sample. The contrast mechanism is related with the atomic number of the components. The higher the atomic number (i.e. Z-number) the lighter the area will appear. Hence, areas with Fe will be the brightest since Fe has a higher Z-number then aluminum and silicon. (b) Elemental EDS map that shows each element by color; Red-Oxygen, Green-Al, Yellow-Fe, and Blue-Silicon. The rectangles indicate the area from which TEM samples were prepared using the FIB.

### 4.1.3 Phase identification by Electron Crystallography

#### Al and $Al_2O_3$ Phases

The phase identification using electron crystallography was started out for the known ceramic phase, $Al_2O_3$. This was done in order to get more familiar with the crystallography software and to check how accurately the results from the software agree with manual indexing of a diffraction pattern. After this was accomplished the unknown structures were analyzed with the help of the software with confidence that the solution is valid. TEM diffraction patterns of individual alumina grains, when viewed along one of the major zone axes, showed the same contrast for the entire area, indicating that individual grains of the alumina structure in all samples were single crystal. Figure 4.2 shows $Al_2O_3$ and Al diffraction patterns with the location it was taken from, and including the EDS spectrum for verification. Unlike the ceramic phase, the Al-based phases are polycrystalline, and the electron diffraction pattern is not symmetric. This means that the corresponding Al grain, from which the diffraction pattern was recorded, it is not oriented along a major crystallographic axis in this sample orientation.

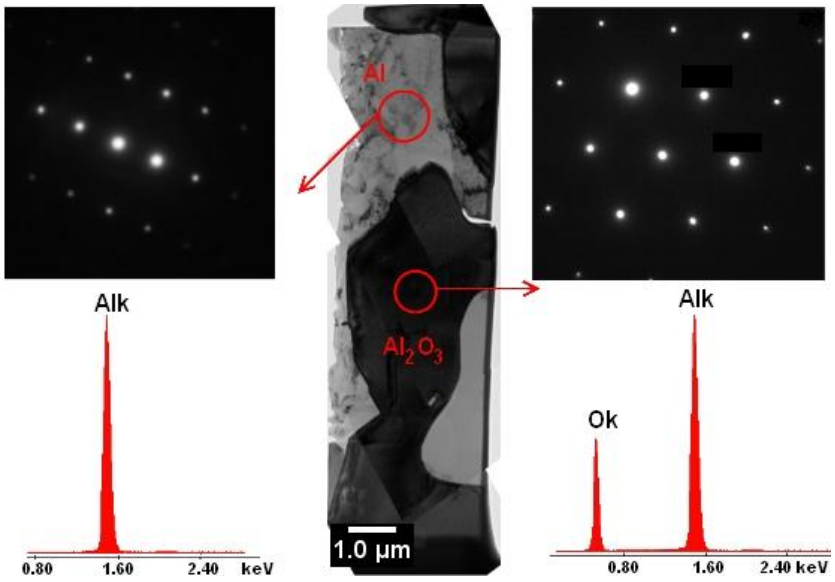


FIGURE 4.2: Identification of $Al_2O_3$ and Al phases in the TCON sample using selected area electron diffraction (SAED) and EDS techniques. EDS analysis was used to correlate the chemical composition with corresponding diffraction patterns.

To manually index the pattern the following steps are taken:

1. A spot and its nearest neighbors are chosen and the distance ratios between the central spot and all neighbors as well the angle between those spots are measured, Figure 4.3. Note that image (a) in Figure 4.3 was inverted in contrast because it is easier to work with dark spots on a white a background.

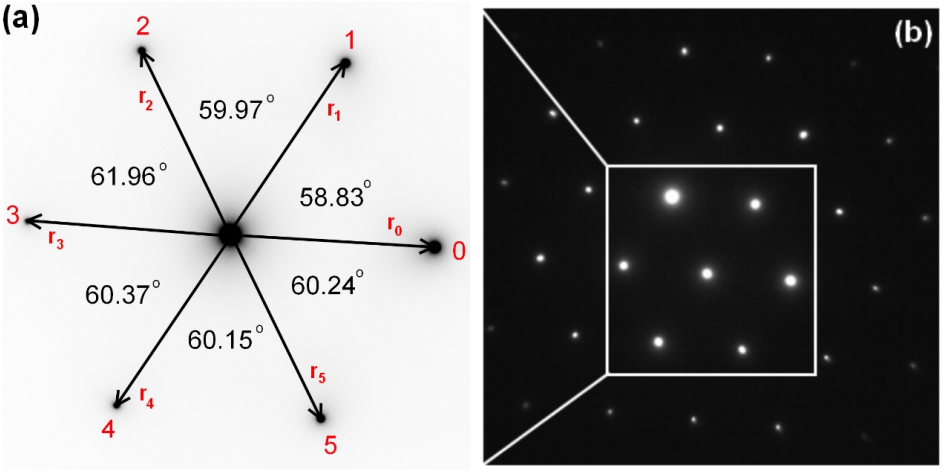


FIGURE 4.3: (a) Seven spots from the selected area electron diffraction pattern in (b) were taken, and the angles and ratios between them where measured. This information was organized into tables, Tables 4.1, 4.2, 4.3 and 4.4.

2. The microscope is aligned so that the camera length is known in order measure the d-spacing between the spots. See Appendix for details.

3. Tables were prepared to compare the ratios obtained with the theoretical ratios of given d-spacing, Tables 4.1, 4.2, 4.3, and 4.4. Note that there are errors in the diffraction pattern compared to the theoretical calculation. This is due to the nature of the imperfection of the electron microscope, measurement accuracy and signal to noise ratio.

TABLE 4.1: Measured distance ratios between the spots indicated in Figure 4.3.

| | $r_0$ | $r_1$ | $r_2$ | $r_3$ | $r_4$ | $r_5$ |
|---|---|---|---|---|---|---|
| $r_0$ | 1 | 0.833333 | 1.010101 | 0.833333 | 1.00 | 1.00 |
| $r_1$ | 1.21 | 1.010101 | 1.020480 | 1.020480 | 1.010101 | |
| $r_2$ | 0.99 | 0.99 | 1 | 1.010101 | 1.00 | 1.00 |
| $r_3$ | 0.99 | 0.98 | 0.99 | 1 | 0.990099 | 0.990099 |
| $r_4$ | 1.00 | 0.98 | 1.00 | 1.01 | 1.00 | 1.00 |
| $r_5$ | 1.00 | 0.99 | 1.00 | 1.01 | 1.00 | 1.00 |

TABLE 4.2: Theoretical ratios between indicated planes.

| (hkl) | (110) | $(\bar{1}20)$ | $(\bar{2}10)$ | $(\bar{1}\bar{1}0)$ | $(1\bar{2}0)$ | $(2\bar{1}0)$ |
|---|---|---|---|---|---|---|
| (110) | 1 | 1 | 1 | 1 | 1 | 1 |
| $(1\bar{2}0)$ | 1 | 1 | 1 | 1 | 1 | 1 |
| $(\bar{2}10)$ | 1 | 1 | 1 | 1 | 1 | 1 |
| $(\bar{1}\bar{1}0)$ | 1 | 1 | 1 | 1 | 1 | 1 |
| $(1\bar{2}0)$ | 1 | 1 | 1 | 1 | 1 | 1 |
| $(2\bar{1}0)$ | 1 | 1 | 1 | 1 | 1 | 1 |

The theoretical ratios were computed using the following equation. This equation is only valid for the hexagonal and trigonal (hexagonal axes) crystal system.[60]

$$\frac{d_{h_2,k_2,l_2}}{d_{h_1,k_2,l_2}} = \frac{4c^2(h_1^2 + h_1k_1 + k_1^2) + 3al_1^2}{4c^2(h_1^2 + h_1k_1 + k_1^2) + 3al_1^2} \tag{4.1}$$

Where h, k, l are the Miller indices of a crystallographic plane and a, b, c are the unit cell parameters. The unit cell parameters for alumina can be found in Chapter 2, Figure 2.4. A similar procedure was performed in order to check if the measured angles agree with the theoretical calculation.

For the theoretical calculation of the angles the equation (4.2) was used. Similarly to the ratio equation the angle equation is only valid for the hexagonal and trigonal (hexagonal axes) crystal system.[60]

TABLE 4.3: Measured angles between spots indicated in Figure 4.3.

| $\phi$ | 0 | 1 | 2 | 3 | 4 | 5 |
|---|---|---|---|---|---|---|
| 0 | 0 | 58.83 | 118.80 | 180.76 | 241.13 | 301.28 |
| 1 | 58.83 | 0 | 59.97 | 121.93 | 179.22 | 242.45 |
| 2 | 118.80 | 59.97 | 0 | 61.96 | 122.33 | 182.48 |
| 3 | 180.78 | 121.93 | 61.96 | 0 | 60.37 | 120.52 |
| 4 | 241.15 | 182.3 | 122.33 | 60.37 | 0 | 60.15 |
| 5 | 301.3 | 242.45 | 182.48 | 120.52 | 60.15 | 0 |

TABLE 4.4: Theoretical angles between indicated planes.

| $\phi$ | (1 1 0) | (-1 2 0) | (-2 1 0) | (-1 -1 0) | (1 -2 0) | (2 -1 0) |
|---|---|---|---|---|---|---|
| (1 1 0) | 0 | 60 | 120 | 180 | 240 | 300 |
| (1 -2 0) | 60 | 0 | 60 | 120 | 180 | 240 |
| (-2 1 0) | 120 | 60 | 0 | 60 | 120 | 180 |
| (-1 -1 0) | 180 | 120 | 60 | 0 | 60 | 120 |
| (1 -2 0) | 240 | 180 | 120 | 60 | 0 | 60 |
| (2 -1 0) | 300 | 240 | 180 | 120 | 60 | 0 |

$$\cos\phi = \frac{h_1h_2 + k_1k_2 + \frac{1}{2}\left(h_1k_2 + h_2k_1\right) + \left(3a^2/4c^2\right)l_1l_2}{\sqrt{\left(\left(h_1^2 + k_1^2 + h_1k_1 + \left(3a^2/4c^2\right)l_1^2\right)\left(h_2^2 + k_2^2 + h_2k_2 + \left(3a^2/4c^2\right)l_2^2\right)\right)}} \tag{4.2}$$

Where h, k, l are the Miller indices of a plane and a, b, c are the unit cell axes. A Python script was written to produce the tables (Appendix A).

4. The lowest possible indices were picked for the spots. All of the other spots can be obtained by using vector addition of two or more spots. This answer corresponds to what the jEMS[58] software provided as the analysis result, Figure 4.4. Hence, the software can be trusted, and there is reasonable confidence to do more complicate indexing in the automated fashion as a viable alternative to manual indexing which is too complicated and time consuming. Therefore, this verification illustrates that the software obtains indeed a valid answer for indexing patterns and can be used through out the thesis.

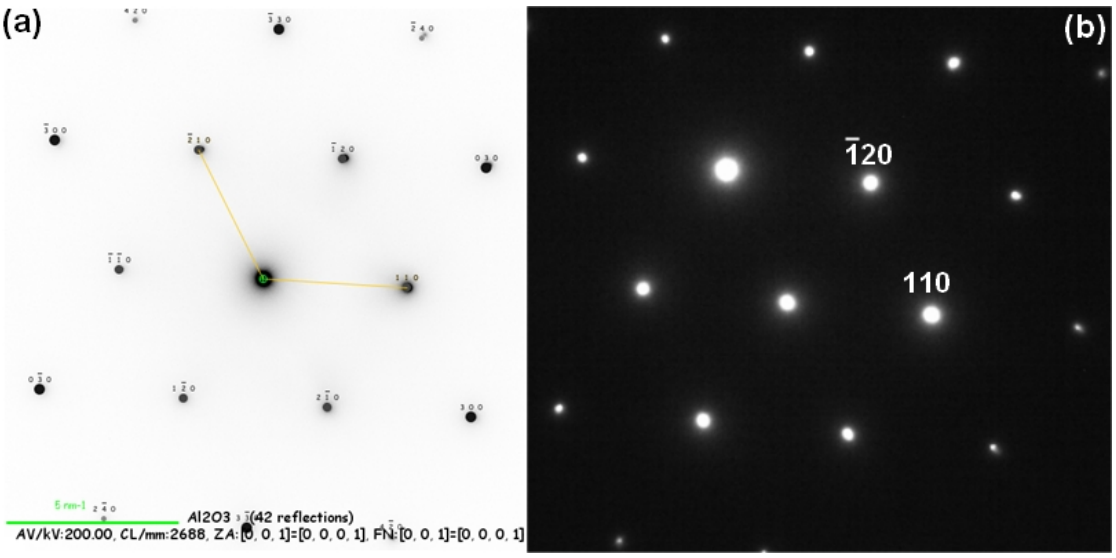


FIGURE 4.4: (a) The indexed selected area diffraction pattern as obtained with the jEMS software after automatic indexing. (b) The diffraction pattern after manual indexing. The two results agree. Diffraction patterns will be indexed with the software but all indexed diffraction patterns will be shown as in (b). Only two planes will be included since all other spots can be obtained by vector addition.

### Aluminum-Iron-Silicon Phase

The TEM and EDS investigation has proved the existence of a nano-scale ternary Al-Fe-Si phase that was not indicated by XRD analysis, Figure 4.5. This ternary phase was possible on theoretical grounds, since there are known Al-Fe-Si phases in the literature. Having all three components present in the material made it possible for them to combine. The following steps were taken in order to analyze the structure of the ternary phase. First, a standardless EDS analysis was performed in order gain some preliminary data on the ratio between Al, Fe, and Si in the ternary phase. Standardless EDS analysis was expected to have some error but is useful for obtaining an approximate elemental composition and for elemental mapping. The results of EDS analysis yielded $Al_{6.9}Fe_{2.9}Si$ as the approximate composition. Next, a literature search was conducted to find if phases with a similar elemental composition have been reported. The result of the literature research is shown in Table 4.5; only three structures were a close match.[46] The unit cells were constructed for these structures in order to simulate a diffraction pattern. Each

simulated diffraction pattern was compared with that of the unknown Al-Fe-Si phase. $Al_4Fe_{1.7}Si$ ($\tau''$) was the best match. Figure 4.5 shows the indexed diffraction pattern. Since the diffraction pattern was able to be indexed with parameters found in literature a number of possible conclusions can be drawn. (1) The error of the standardless EDS analysis was quite high and the elemental composition observed in the sample is the same composition as found in the literature. The error in EDS measurements can be explained based on the nano-scale volume of the Al-Fe-Si ternary phase combined with the low spatial resolution of X-ray analysis due to the use of a quite large probe size. In the particular case presented in Figure 4.5 it is possible that the Al grain observed next to the ternary phase to extend underneath the Al-Fe-Si grain. Therefore, the incident electrons will simultaneously excite the atoms from both phases with the overall effect of higher intensity Al peaks, and thus higher Al content, see Table 4.5. However, the diffraction pattern obtained from the ternary phase was successfully indexed with the unit cell parameters given the literature entry.[46] (2) The atomic percent of Fe in both $Al_4Fe_{1.7}Si$ ($\tau''$) found in the literatures and the $Al_{6.9}Fe_{2.9}Si$ EDX are very similar while the Al and Si percent are different. Hence, the ratio of Al + Si to Fe is similar, 2.9 for $Al_4Fe_{1.7}Si$ and 2.7 for $Al_{6.9}Fe_{2.9}Si$. The atomic radii of Al and Si are also very similar, 125 pm and 110 pm respectively and could possibly be interchange for the same structure to be formed. Therefore even though the Al and Si atomic percentages in the literature and EDS analysis are quite different the structure can be indexed by using the cell parameters found in the literature. Despite the remaining doubts the ternary phase was assigned to be $\tau''$ ($Al_4Fe_{1.7}Si$).

TABLE 4.5: Experimental $Al_{6.9}Fe_{2.9}Si$ EDX compound compared to similar compounds from the literature.

| Phase Name | Al (at%) | Fe(at%) | Si(at%) | Space group | Lattice parameter (nm) |
|---|---|---|---|---|---|
| Standarless EDS analysis $Al_{6.9}Fe_{2.9}Si$ | 63.9 | 27.0 | 9.2 | unknown | unknown |
| $Al_4Fe_{1.7}Si$[46] ($\tau$") | 59.7 | 25.4 | 14.9 | Hexagonal $P6_3/mmc$ | $a = 0.7509$ $c = 0.7594$ |
| $Al_{15}Fe_6Si_5$ ($\tau_5$ or $\alpha$) | 57.7 | 23.1 | 19.2 | Hexagonal $P6_3/mmc$ | $a = 1.2404$ $c = 2.6223$ |

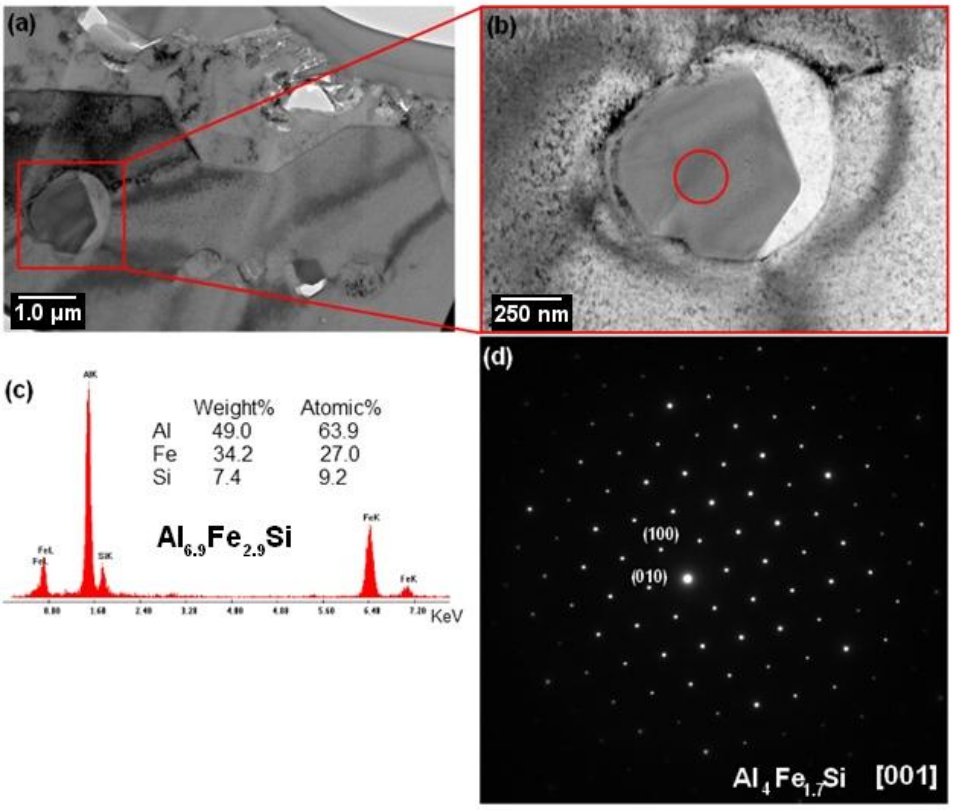


FIGURE 4.5: ((a) Bright field TEM micrograph of the area where the ternary particle was found. (c) The standardless EDS analysis. (d) Indexed selected area electron diffraction pattern with a known structure from literature.

### Aluminum-Iron Phase

Finding the correct structure for the binary Al-Fe proved to be challenging. There were three structures listed in the database, two of them virtually identical, which closely match the powder XRD and electron diffraction patterns. The two unique structures are given in the Table 4.6.

Table 4.6: Possible matches for Al-Fe phase.

| Phase name | Lattice System | Space group | Lattice parameter (nm) |
|---|---|---|---|
| $Al_{13}Fe_4$[71] | Orthorhombic | $B$mmm | a= 0.7751<br>b=0.4034<br>c=2.3771 |
| $Al_{13}Fe_4$[70] | C-centered Monoclinic | $C2/m$ | a=1.549<br>b=0.807<br>c=1.247<br>$\beta$=107.7° |

The matching of the electron diffraction patterns to know structures was performed as follows. Unit cells were constructed and indexing was attempted for the two possible structures. Initially many unit cells simulated matched the diffraction pattern. Tilting of the sample was performed and collection of more diffraction patterns was able to eliminate some of these structures. The intent was to tilt the sample and index the patterns until only one of the simulated patterns matched with the actually pattern. After numerous tilting attempts the only two structures, given in Table 4.6, the $Al_{13}Fe_4$ (Orthorhombic) and $Al_{13}Fe_4$ (C-centered monoclinic), remained. More investigation had to be done in order to be certain of the structure assignment. A literature search was conducted to find if any similar monoclinic and orthorhombic structures have been reported for $Al_{13}Fe_4$. A Paper by Liebertz and Koster[70] reported multiple twinning in samples of monoclinic $Al_{13}Fe_4$ showing pseudo-orthorhombic symmetry. Their results state that since the C-centered monoclinic structure is twinned in such a manner it can be confused with the orthorhombic structure given by previous authors[10]. They concluded that the orthorhombic structure for $Al_{13}Fe_4$ was not assigned correctly and the actually structure is C-centered monoclinic.

Parallel to the TEM analysis of the Al-Fe sample Matthias Zeller of Youngstown State University and a group of five undergraduate students analyzed an Al-Fe melt (7.5wt.% Fe) by single crystal x-ray diffraction. The Al-Fe melt exhibited the same XRD pattern as the composite material minus the peaks for $Al_2O_3$ and Si. In their project they dissolved the aluminum matrix in boiling phenol[69] and the freed Al-Fe particles were screened by single crystal XRD. Their results were very similar to those of Libertz and Koster[30] and indicated that the structure is indeed $Al_{13}Fe_4$ (C-centered monoclinic).[68] In addition to finding the correct structure of $Al_{13}Fe_4$ their single crystal results also agree with the previously reported structure for $Al_{13}Fe_4$.[69,72,73,74] Hence, it can be safely assumed that the structure for the binary Al-Fe phase is $Al_{13}Fe_4$ since both single crystal x-ray and electron diffraction analyses agree. This is one example where powder XRD and selected area electron diffraction patterns alone could not unambiguously solve a problem.

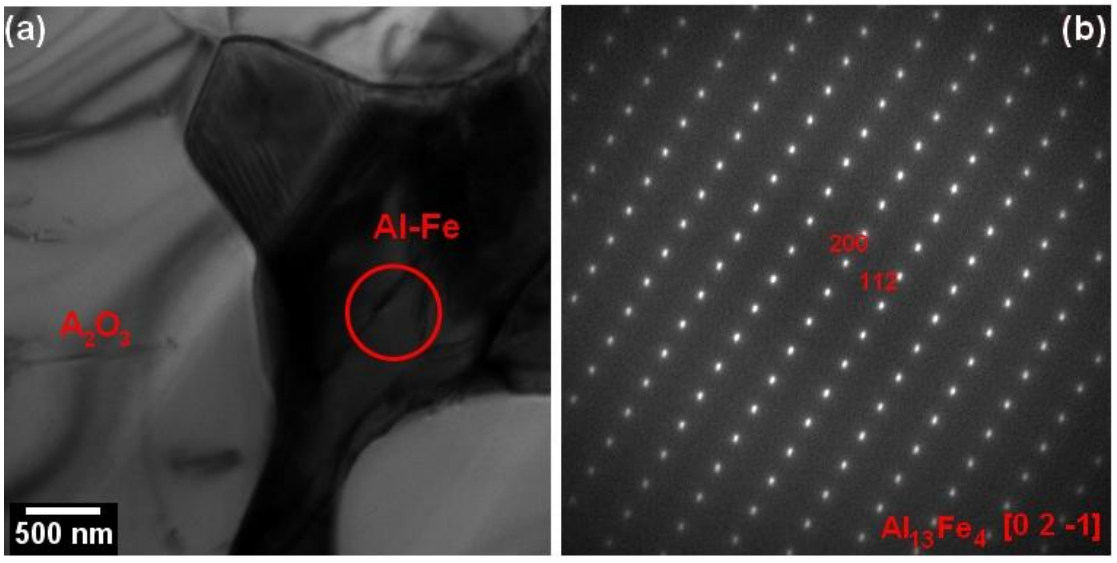


FIGURE 4.6: (a) Bright field TEM micrograph that shows the Al-Fe phase. The red circle indicates the location from where the diffraction pattern was taken. (b) The best match for the diffraction pattern was $Al_{13}Fe_4$ (C-centered monoclinic).

Prior to 2009's paper published by Sundman *et al.*[37] the equilibrium compound listed in the phase diagram for Al-Fe in the area $Al_{13}Fe_4$ had been $Al_3Fe$. In the past it

was hypothesized that if the final product containing an Al-Fe alloy is cooled in a slow controlled manner rather than quenched that the resulting phase would be $Al_3Fe$. A newly revised phase diagram of Al-Fe is presented by Sundman's[37] paper which shows that the previously assigned $Al_3Fe$ regions have been replaced by $Al_{13}Fe_4$. According to this paper the $Al_{13}Fe_4$ phase is considered the thermodynamically stable aluminum rich phase.

### 4.1.4 Orientation Relationships

#### $\mathbf{Al/Al_2O_3}$

The orientation relationships were determined between phases in order to find how two phases are oriented relative to each other. It must be noted that alumina is mostly single crystalline while aluminum is polycrystalline in the sample. Therefore the sample was tilted on the zone axes of the alumina phase and a diffraction pattern was obtained from a grain of aluminum together with that of alumina in order to find the orientation relationship (OR) between the two. Only one grain of aluminum was picked for the OR analysis (the aluminum phase is polycrystalline but the grain boundaries can be seen in a TEM micrograph). After the OR was indexed and the corresponding directions and planes were found an atomic model was developed to illustrate the relationship. One such selected area and the corresponding electron diffraction pattern are shown in Figure 4.7. The orientation relationship between the two grains was determined as follows:

$$[\bar{1}00]_{Al_2O_3}//[310]_{Al}$$
$$(006)_{Al_2O_3}//(002)_{Al}$$

The model in Figure 4.8 illustrates the orientation relationship between the two phases on the atomic scale.

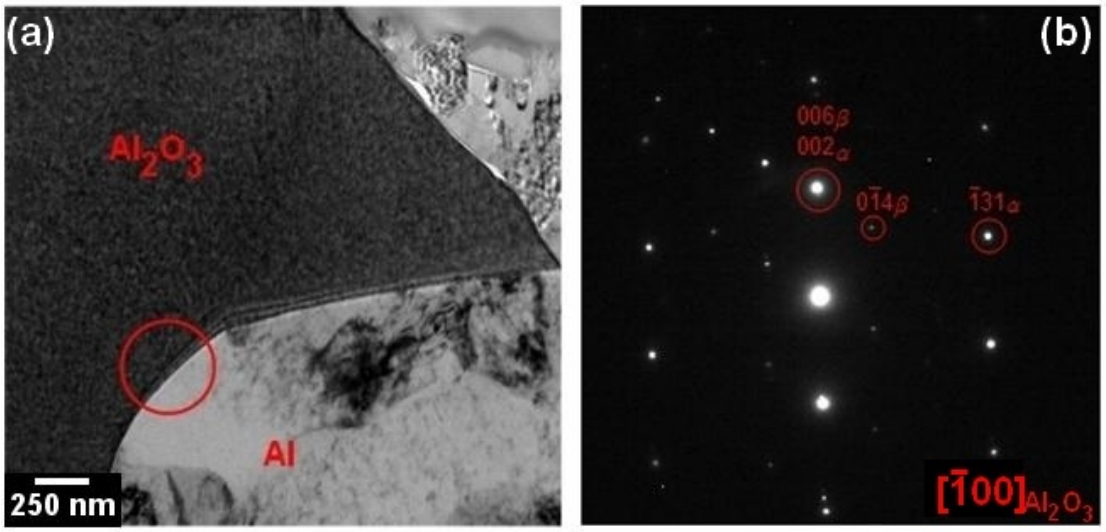


FIGURE 4.7: (a) Bright field electron micrograph of an $Al/Al_2O_3$ interface. The red circle indicates the area from which the diffraction pattern was obtained. (b) Shows the indexed diffraction pattern that reveals the orientation relationship between the $Al_2O_3$ and Al phases. $\alpha$ indicates Al and $\beta$ indicates $Al_2O_3$.

Looking at the geometrical interpretation of this result is interesting. The unit cell of alumina in the c direction is 12.99 Åwhile aluminum's c length is 4.04 Å. Thus, three unit cells of aluminum (4.04Åx 3 = 12.12 Å) in the c direction are needed to nearly match the alumina phase, refer to Table 2.3 for lattice information. Phases strive when possible to accommodate with neighboring phases in such a manner as to minimize the total energy in the crystal and at the interface. At times, it takes less energy for a phase to slightly rotate itself to fit another phase as shown in this orientation relationship. In other cases, the phase will develop defects to accommodate another phase. These defects might include stacking folds, dislocations, and twinning.

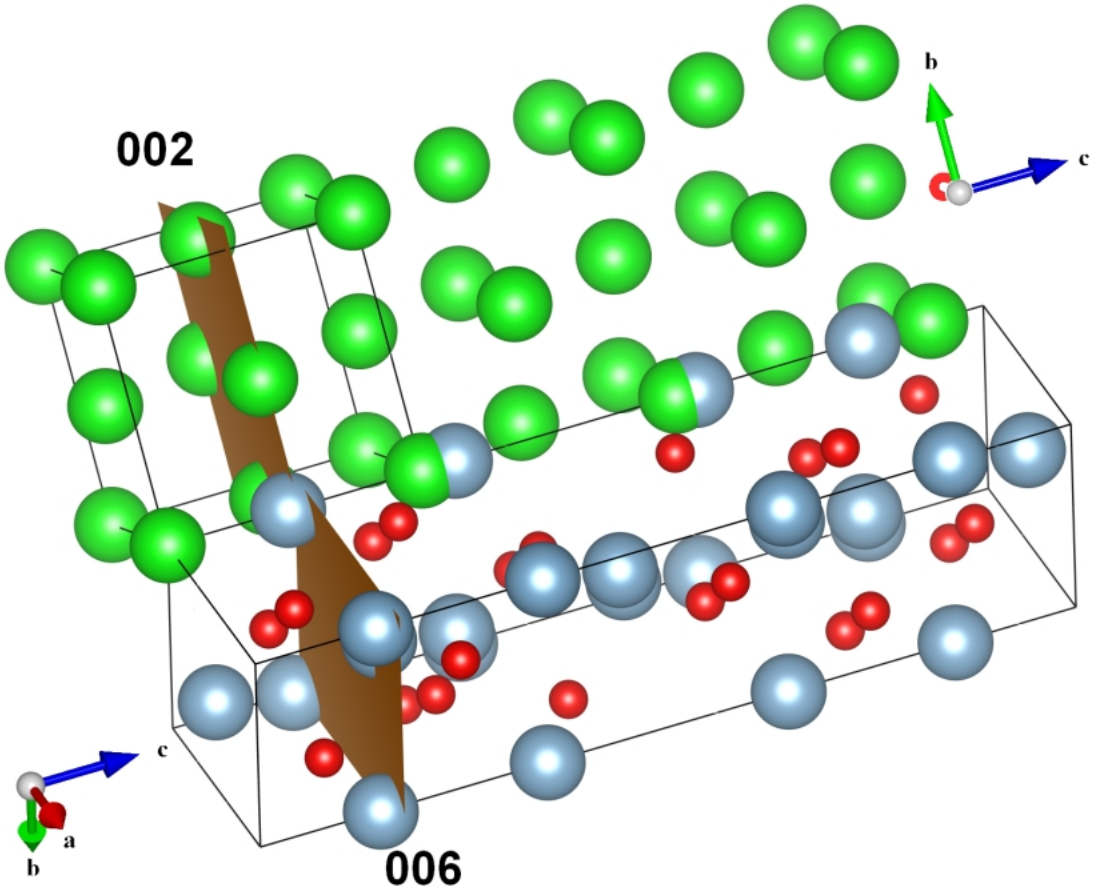


FIGURE 4.8: Schematic model showing the orientation between Al and $Al_2O_3$ at atomic level. The green atoms are aluminum of the metallic aluminum phase and the unit cube can be seen, while the blue and red atoms are the alumina structure. This model shows the planes $(002)_{Al}$ and $(006)_{Al_2O_3}$ are indeed parallel and the OR is valid.

### $Al_2O_3/Al_{13}Fe_4$

In a similar manner, an orientation relationship was determined between alumina and the binary phase $Al_{13}Fe_4$. It was easy to obtain this OR since both $Al_2O_3$ and $Al_{13}Fe_4$ are formed over a large area of the sample. This time the $Al_{13}Fe_4$ phase was tilted onto a major zone axis and the corresponding alumina orientation was determined. An interesting fact is that the alumina was very near a major zone axis when the $Al_{13}Fe_4$ was on a major zone axis. The corresponding selected area electron diffraction

pattern is shown in Figure 4.9. The orientation relationship between the two phases was determined to be:

$$[1\bar{1}1]_{Al_2O_3}//[\bar{4}03]_{Al_{13}Fe_4}$$
$$(\bar{1}23)_{Al_2O_3}//(31\bar{1}4)_{Al_{13}Fe_4}$$

The different spacing of atomic planes can be seen in the diffraction pattern. $Al_{13}Fe_4$ has very close packed spots in reciprocal space. Therefore the atom planes in real space have to be further apart than in alumina where the spots are more spread out.

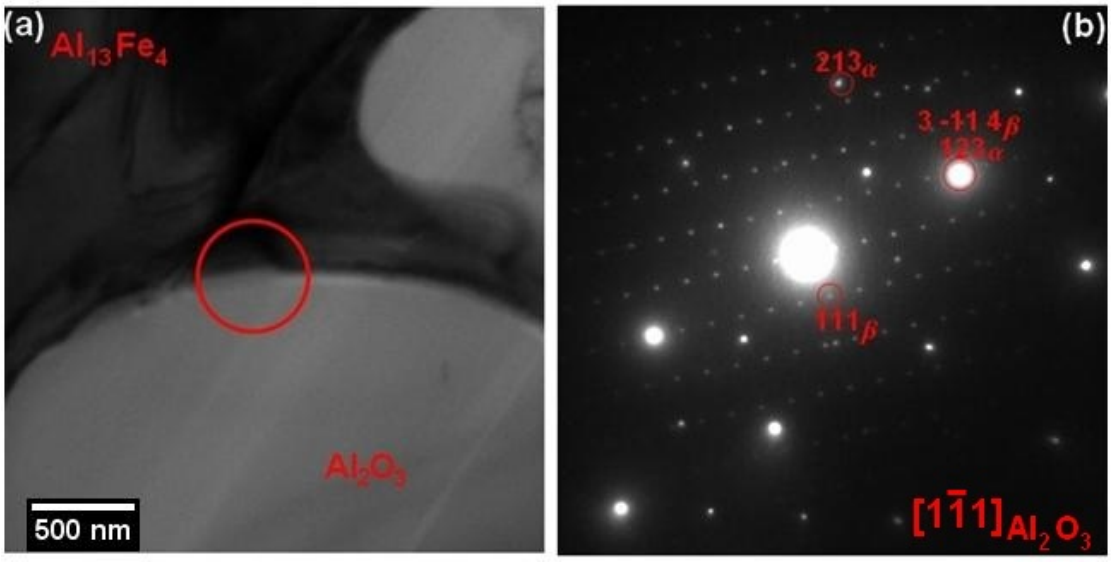


FIGURE 4.9: (a) Bright field (BF) TEM micrograph showing the $Al_2O_3$ and binary $Al_{13}Fe_4$ boundary. The red circle indicates the location from where the diffraction pattern was taken. (b) Corresponding selected area diffraction pattern collected from the red circle. $\alpha$ indicates the $Al_2O_3$ spots and the $\beta$ indicates the $Al_{13}Fe_4$ spots.

The model in Figure 4.10 illustrates the orientation relationship between the two phases on the atomic scale. The geometrical considerations in this model are not as trivial as in the last orientation relationship. In this model it is harder to see if the two phases fit in a purely geometrical sense. These two phases do not match very well; further investigation has to be performed in order to find out what is happening at the boundary. Even though, the monoclinic unit cell could theoretically match the trigonal unit cell

in a compact manner, since alumina's c length is 12.99 Åand $Al_{13}Fe_4$'s is 12.47 Åwhich align as seen in Figure 4.10.

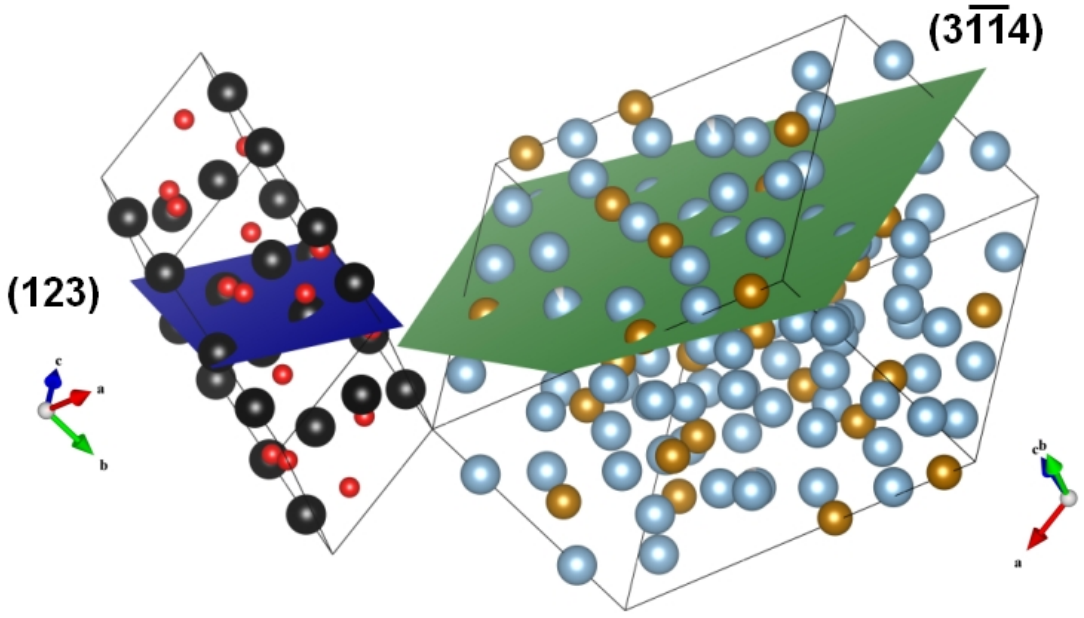


FIGURE 4.10: Atomic model of the orientation relationship between $Al_2O_3$ and $Al_{13}Fe_4$. The parallel planes are shown in the two structures, the blue plane in alumina and the green plane in aluminum-iron. It can be observed that these two planes are indeed parallel and the orientation relationship is verified. Even though the orientation relationship is valid, the two phases do not match very well hence something more complex might be happening at the boundary of these two phases.

### $Al_2O_3$/ $\tau''$(Al-Fe-Si)

Lastly, an orientation relationship was determined between the alumina and the ternary phase $\tau''$ (Al-Fe-Si). It was difficult to obtain this OR since the $\tau''$ phase grains are very small, Figure 4.11 (a). The $\tau''$ grain was tilted to a major zone axis and the corresponding alumina orientation was determined. Similar to the previously discussed OR, the alumina grain was also near a major zone axis. The corresponding selected area electron diffraction pattern is shown in Figure 4.11 (b). The orientation relationship between the two phases was determined to be:

$$[4\bar{4}\bar{1}]_{Al_2O_3}//[120]_{\tau''}$$
$$(\bar{1}\bar{1}0)_{Al_2O_3}//(\bar{6}3\bar{6})_{\tau''}$$

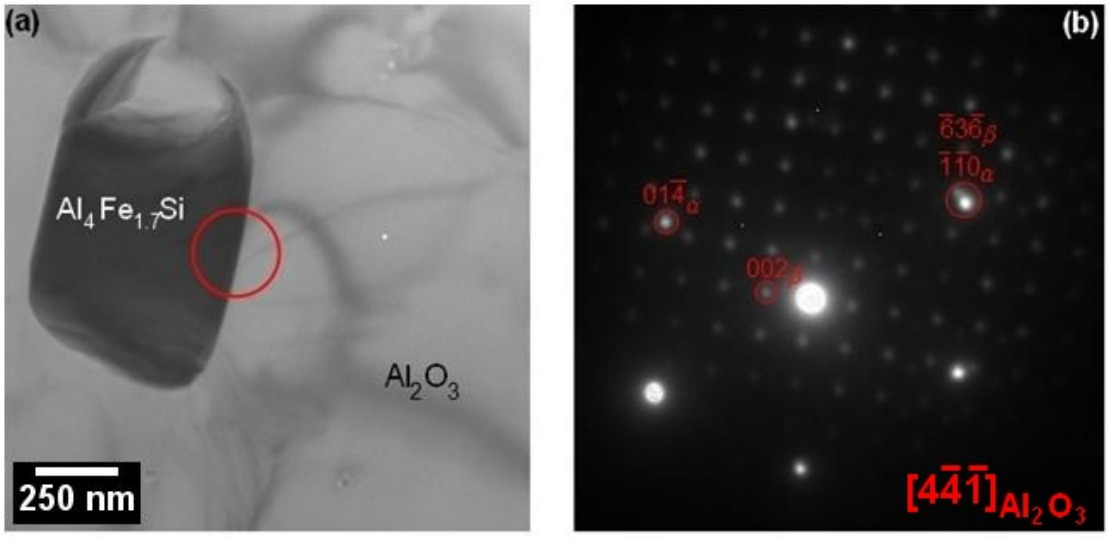


FIGURE 4.11: (a) Bright field TEM micrograph of a $Al_4Fe_{1.7}Si$ ($\tau''$)particle embedded in $Al_2O_3$ matrix. The red circle indicates from where the electron diffraction pattern in (b) was obtained. $\alpha$ and $\beta$ indicate $Al_2O_3$ and $\tau''$ respectively.

### 4.1.5 Silicon Inclusions

Several researchers, such as Breslin[27], and Banerjee and Roy[33] state that silicon diffuses out into the molten metal bath. However, it was found that silicon particles still remain in the final product.[15,27,28,33] These particles can be on the micron scale range, as seen in TEM micrograph shown in Figure 4.12 (a).

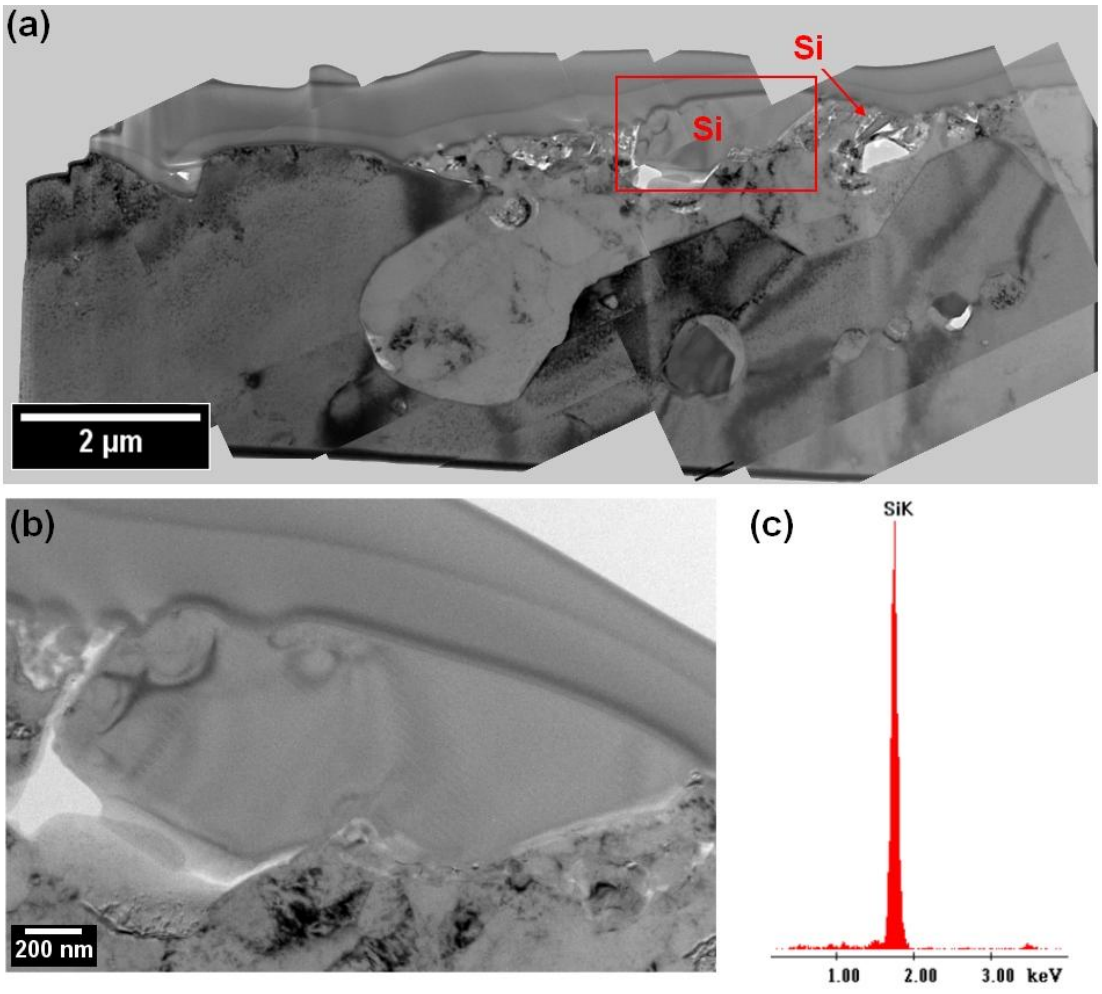


FIGURE 4.12: (a) Composite bright field micrograph of a TEM sample showing the positioning of silicon particle within the composite material. (b) Silicon particle observed in Al-Fe-transformed TCON material. (c) Typical EDS spectra recorded form silicon particles

Silicon particles were observed in all investigated samples and this section discusses the features observed in the silicon inclusions. First, the observed silicon particles have a plate-like morphology. Figure 4.13 (a) shows a side view of a of a silicon particle. A more detailed search was conducted by tilting the investigated TEM samples and looking for any difference in morphology. The silicon particles seen in Figure 4.13 (b), (c) are surrounded by pure Al and $Al_4Fe_{1.7}Si$ phases. It is believed that silicon particles in Figure 4.13 (b), (c) are view along the short edge of the particle shown in (a). Therefore, it is concluded that the silicon particles have plate-like morphology.

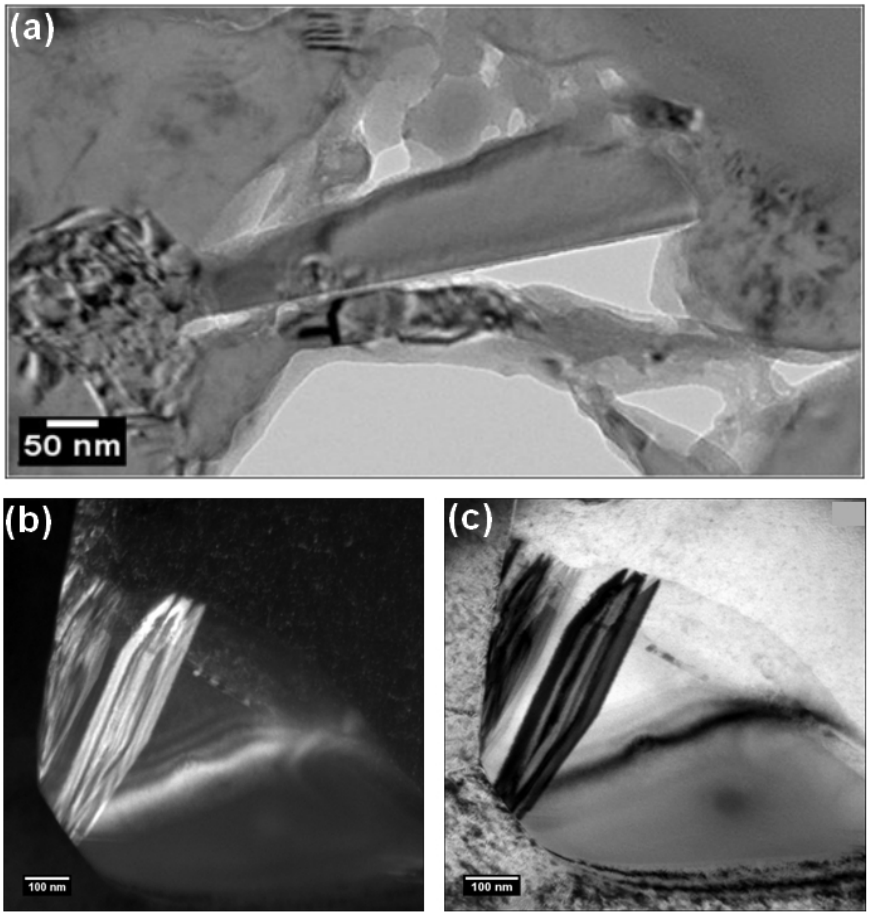


FIGURE 4.13: (a) A darkfield micrograph showing the plate like nature of this silicon inclusion. The silicon inclusion is embedded into the aluminum and is not next to voids as previously found. (b) The corresponding brightfield micrograph.

Figure 4-13 (a) also provides some insight into the kinetic growth mechanism of silicon

particles. Silicon particle nucleated and grew within a void between two aluminum volumes. Micron and submicron size voids are commonly observed in transformed TCON materials.[11] The silicon particle seems to emerge (nucleate and grow) from Al volume at left, and expanded until impinged into the Al volume at right (as indicated by arrows in Figure 4.13 (a)). Silicon has limited solubility in aluminum, 1.65wt% at 577°C,[new] and upon cooling segregates as silicon particles in an $\alpha$-Al matrix.

Second, the particles seems to be single crystalline, as indicated by electron diffraction and high resolution imaging investigations, Figures 4.14 and 4.15. Moreover, the particles have a modulated structure which can be only observed in certain orientations. When the sample is tilted in a certain direction the modulation can be observed in both the image and the corresponding diffraction pattern, Figure 4.14. Hence, the modulation is only present in certain crystallographic directions.

After noticing the modulation, high resolution micrographs have been taken in order to elucidate the nature of the modulation, Figure 4.15. The high resolution micrographs reveal the existence of modulation within the silicon crystal. The modulated sequence has a periodicity of six atomic planes, as confirmed by the electron diffraction (five extra satellite reflections between the fundamental spots).

Silicon is a well studied element because of its importance to the semi-conductor industry. Hence a literature search has been conducted to find if similar features have been reported for silicon. A paper by Scheerschmidt and Werner[61] reported twinning along the [111] direction in carbon supersaturated silicon. The paper provides a high resolution image simulation which matches the high resolution images obtained in this research. However, in carbon supersaturated silicon modulated sections of the crystals are limited by the twin boundary, while in the TCON samples the modulation is observed for the entire crystals. Scheerschmidt and Werner[61] concluded that carbon incorporation at the twin boundaries is a possible cause of the crystalline modulation. This is not the case for TCON sample in which, at least theoretically, there is no carbon.

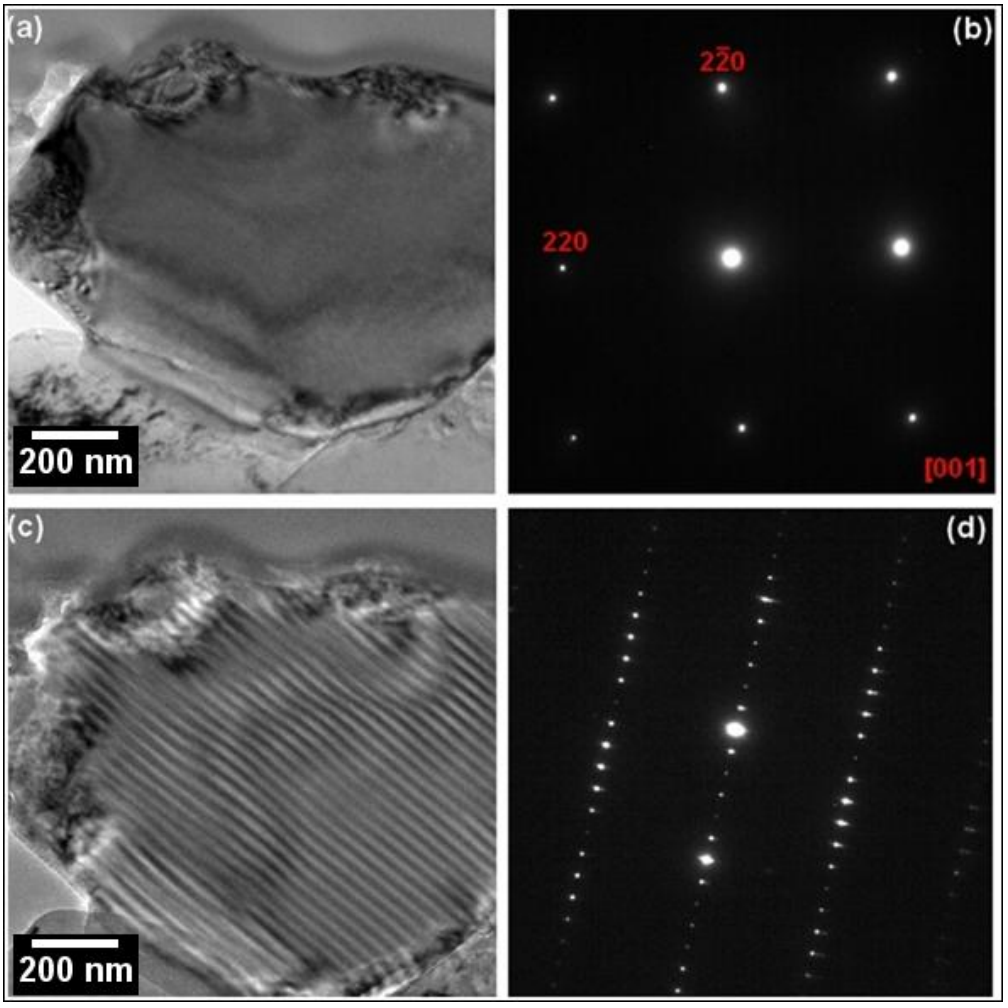


FIGURE 4.14: (a) Bright field electron micrograph of a silicon particle in an orientation with no apparent modulation, as indicated by corresponding selected area electron diffraction pattern in (b). (c) Bright field micrograph of the same particle as in (a) recorded at different orientation, and the corresponding diffraction pattern in (d). The diffraction pattern in (d) shows a six fold modulation along one of the major axes.

Most inorganic crystal structures are periodic in three dimensions which follow a set of symmetry operations and display a diffraction pattern that can be indexed with three integers.[80] In modulated structures, atoms or groups of atoms are shifted or rotated with respect to their neighbors such that the three-dimensional translational symmetry is distorted.[80] These shifts and rotations in modulated structures are not random but rather follow distinct rules. There are two kinds of modulated structures: commensurate and incommensurate. In commensurately modulated structures the periodicity

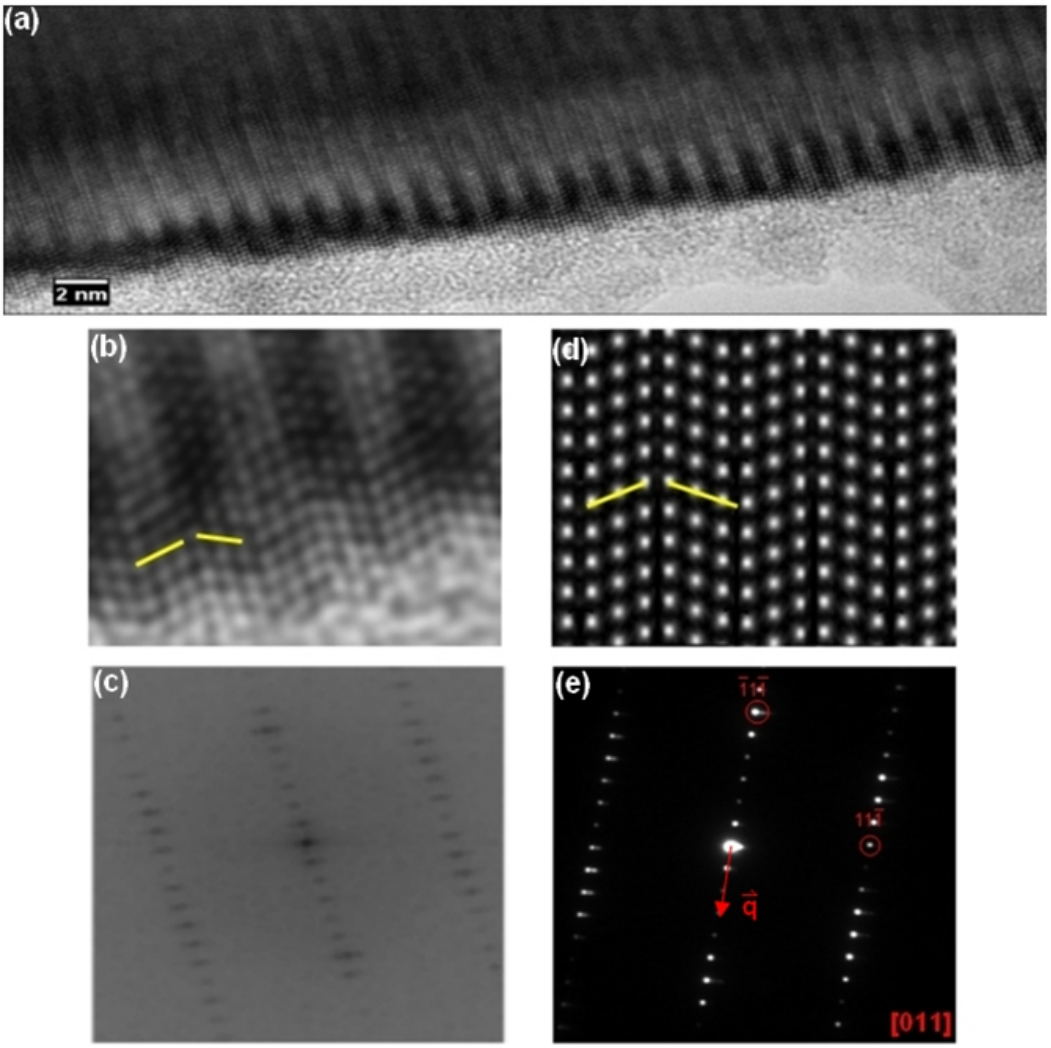


FIGURE 4.15: (a) High resolution micrograph which shows the modulated structure of the silicon particle in Figure 4.13 (a). (b) A closer look at the modulation shows a periodicity of six atomic planes. (c) A Fast Fourier Transform (FFT) was taken to see if the patterns will match the modulated diffraction pattern from the silicon. (d) Scheerschmidt and Werner61 high resolution image simulation on [110] direction matches the experimental high resolution micrograph in (b). (e) To obtain a basic cell of the structure only the main spots are indexed and the satellites between the main spots are ignored. The pattern indicates that the basic cell matches the silicon structure on the [011] direction. This is commonly referred to as the average structure. There is a larger six fold supercell that will solve the structure completely. The modulation vector q indicates the direction along which the commensurately modulation occurs.

matches an integral number of lattice translations of the basic cell, while incommensurately modulated structures the periodicity does not match an integral number of lattice translation.[80] The periodic nature of modulated gives rise to additional diffraction spots which are referred to as satellite reflections and usually they are less intense then the main reflections. The satellite reflections can lie on one of the main axis, but that is not always the case. Modulated structures are not defects in crystal but have long-range order which can be mathematically described by the so-called atomic modulation functions (AMFs).[80]

A possible cause for the silicon modulation in TCON materials might be that the particle was compressed by the surrounding matrix. The compression caused the silicon atoms to reorganize in order to accommodate to the smaller space. The modulation is seen in the diffraction pattern because satellite spots appear in the diffraction pattern around the main spots. These satellite reflections have weaker intensities compared to the main spot. In this case the satellite reflections are all equally spaced and collinear with the main spots. It can be concluded that commensurate modulation is present in these silicon particles.

In order to obtain the basic cell and the average crystallographic structure of the modulated silicon only the main spots were included in the indexing and the satellites were ignored. The result of this indexing reveals that the silicon un-modulated structure is along [011] crystallographic direction, see Figure 4.14 (b). Hence, the modulation occurs in the [011] direction, see Figure 4.15 (b). Further analysis has to be carried out to find the supercell of the structure and fully solve the structure that occurs in the silicon inclusions.

In order to validate the claim that upon cooling silicon shrinks less than aluminum and alumina, which this might "'squeeze"' the silicon particle and be the source of modulation, an approximation calculation was done using a thermal expansion coefficient analysis. Table 4.7 shows the linear expansion coefficient by which each element will contract, and it can be seen that silicon will contract least. The results are calculated

with equation 4.2, where $\Delta$L is the change in length, $\alpha$ is the linear expansion coefficient, L is the initial length, which was taken to be a unit meter, and $\Delta$T is the change in temperature with $T_f$=25°C and $T_i$=1200°C. Even though this is a rough approximation and the volumetric contraction is not taken into account it still conveys the argument that the silicon will shrink the least. This approximation shows that silicon will contract least and therefore it is a possibility that the silicon is being squeezed by the aluminum, which induces the modulated structure.

TABLE 4.7: Elements and their corresponding linear expansion coefficients, with the last column calculated using Equation 4.1.

| Element | Linear Expansion Coefficient $\alpha$ ($10^{-6}$/°C) | Contraction (mm/m) |
|---|---|---|
| Al | 23 | 27 |
| Si | 3 | 3.5 |
| $Al_2O_3$ | 8.1 | 95.2 |

$$\Delta L = \alpha L \Delta T \tag{4.3}$$

### 4.1.6 HREM Investigations

Based on the orientation relationship discussion in section 4.1.3 there is a small misalignment between $Al_2O_3$ and $Al_{13}Fe_4$, Figure 4.10. Since the OR showed a mismatch it was hypothesized that something more was happening at the boundary between $Al_2O_3$ and $Al_{13}Fe_4$. Additional analysis was performed using high resolution electron microscopy imaging to observer the boundary between the two phases. High resolution electron micrographs were obtained from a nano-scale particle which reveals the ceramic-metal interface shown in Figure 4.16. The interface between the alumina and the $Al_{13}Fe_4$ particle looks interesting in many regards. First, the crystal structure on the boundary looks different than the structure in the middle of the particle. This could mean that there is a buffer layer between the single-crystalline ceramic phase and the binary $Al_{13}Fe_4$ phase. It was found that there is some silicon on the boundary so therefore the

boundary may consist of Al-Fe-Si. Buffer layers are well studied because of their wide use in the semi-conductor industry. A buffer layer can be defined as a layer between two crystalline materials that helps to accommodate the difference in their crystallographic structure. This buffer layer can be thought of as an intermediate layer that fits well with both crystalline materials and helps connecting two mismatching structures. In this case, an Al-Fe-Si phase seems to be the buffer layer for $Al_2O_3$ and $Al_{13}Fe_4$. This buffer layer is at most couple nm thick hence no extra diffraction spots were observed while indexing the orientation relationship. It was noticed later after careful observation that this buffer layer occurs everywhere where $Al_{13}Fe_4$ is present in proximity to $Al_2O_3$. Based on the orientation relationship calculation along with high resolution imaging analysis it can be concluded that the Al-Fe-Si buffer layer observed between $Al_2O_3$ and $Al_{13}Fe_4$ help to reduce the crystallographic mismatch between the two phases.

### HREM Simulation

To improve the image quality of the high resolution micrograph a Fast Fourier Transform (FFT) was taken, and the spots corresponding to the periodic structure were masked. After masking an inverse FFT was taken to obtain the image back. This new image has better quality because only those signals which produce the periodic structure in the image are selected and the noise is reduced in this manner. Figure 4.17 shows the process of using FFT in order to reduce the noise of the image.

Multislice simulation, explained in section 3.2.1, was performed in order to precisely locate the atoms in the ceramic material. The single crystal ceramic was found to be orientated along the [001] direction before the high resolution micrographs were taken, Figure 4.19 (a). A map of thickness and de-focus was produced in order to be compared the recorded micrograph, Figure 4.18. Figure 4.19 shows the results of the multislice simulation. The simulation indicates that the thickness of the sample was approximately 127.42 nm and defocus was -44.0 nm.

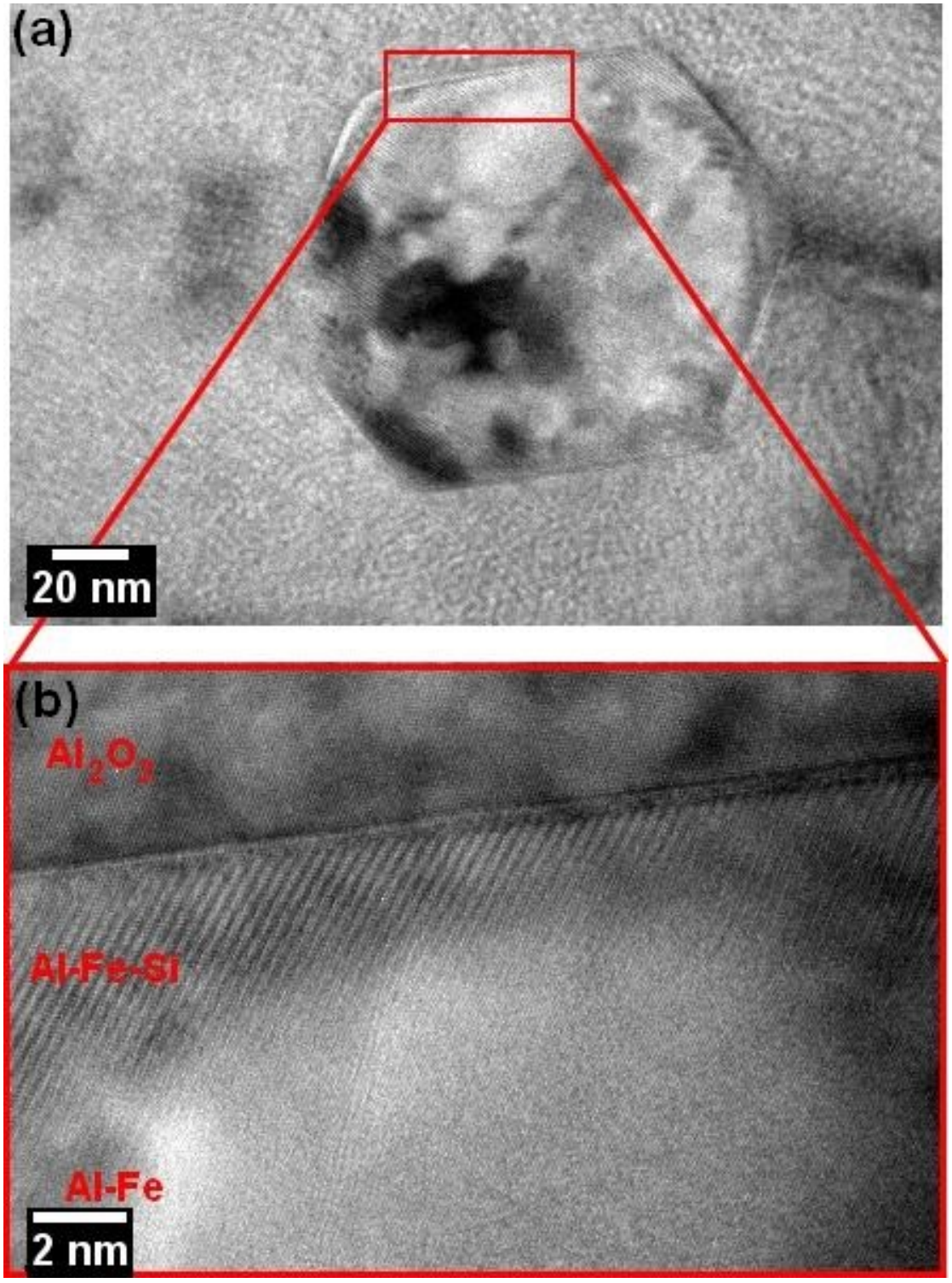


FIGURE 4.16: (a) High resolution electron micrograph of a Al-Fe metal particle embedded in $Al_2O_3$ matrix. (b) Atomic resolution electron micrograph recorded from the area marked in (a). Al-Fe-Si buffer layer between the $Al_2O_3$ and the Al-Fe structures can be observed in both micrographs.

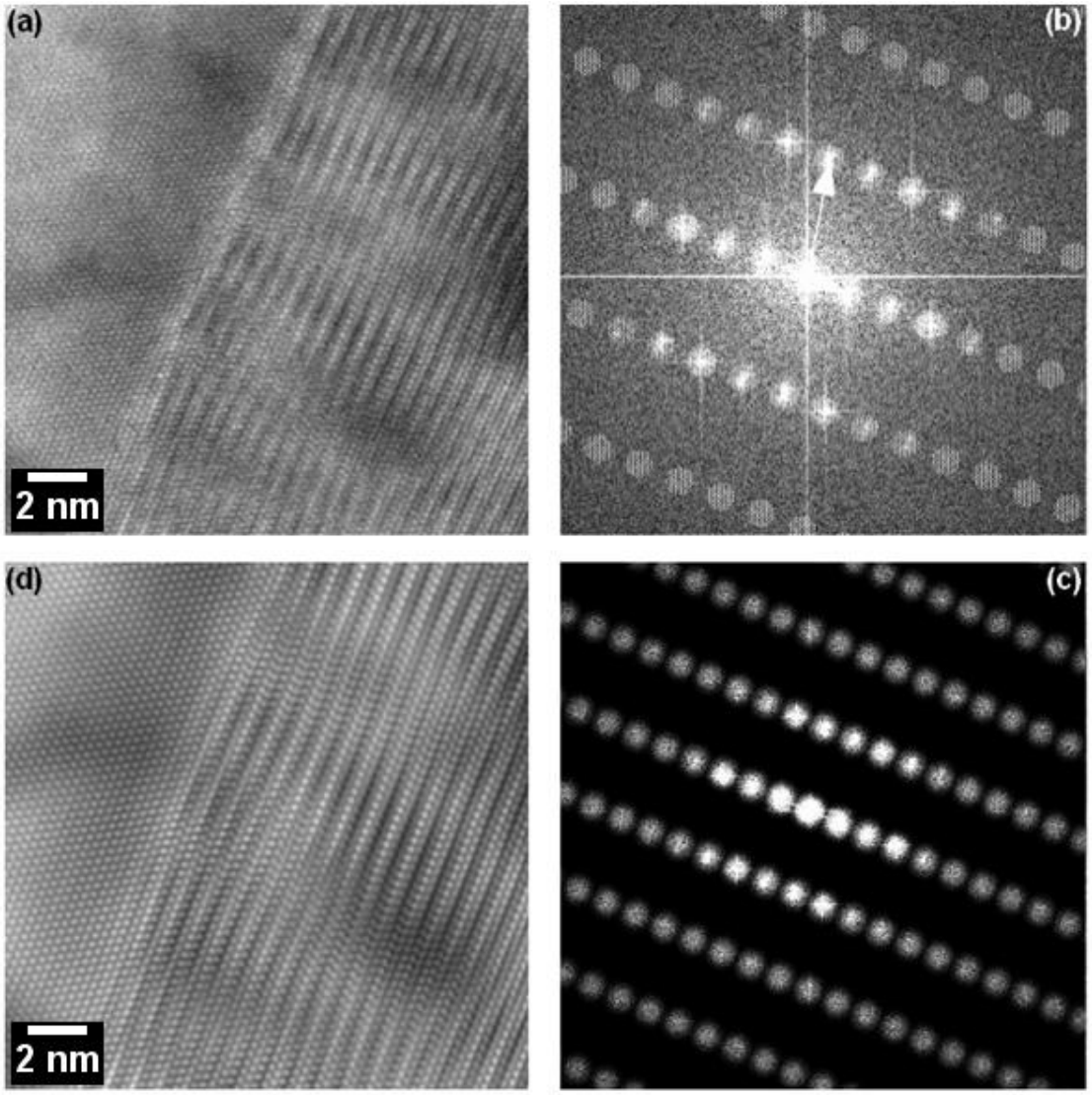


FIGURE 4.17: (a) Original high resolution electron micrograph. (b) The FFT of the original image with the mesh pattern overlaid. (c) The result of applying the mask onto the FFT. (d) The new reduced noise image obtained as the result of the inverse FFT transform operation

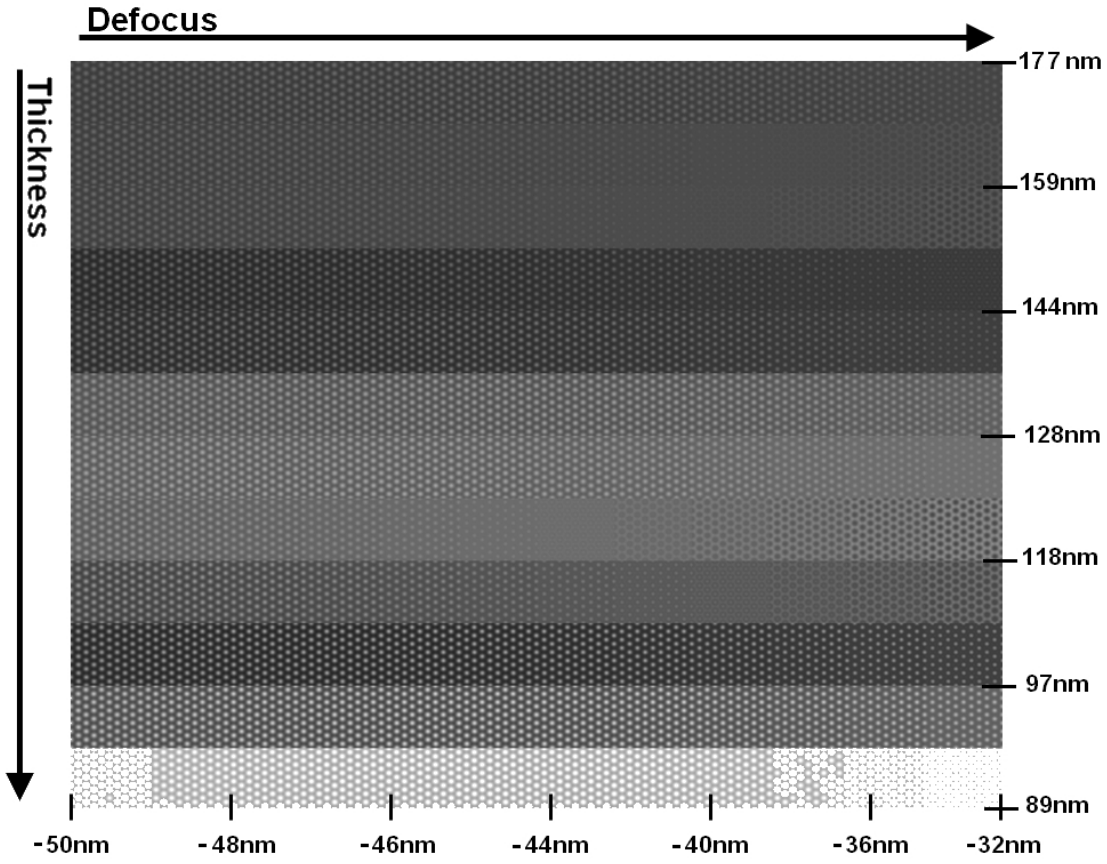


FIGURE 4.18: Map of thickness and de-focus for $Al_2O_3$. The map starts at defocus -50 nm with increments of 1 nm . The thickness is varied from 177 nm with increments.

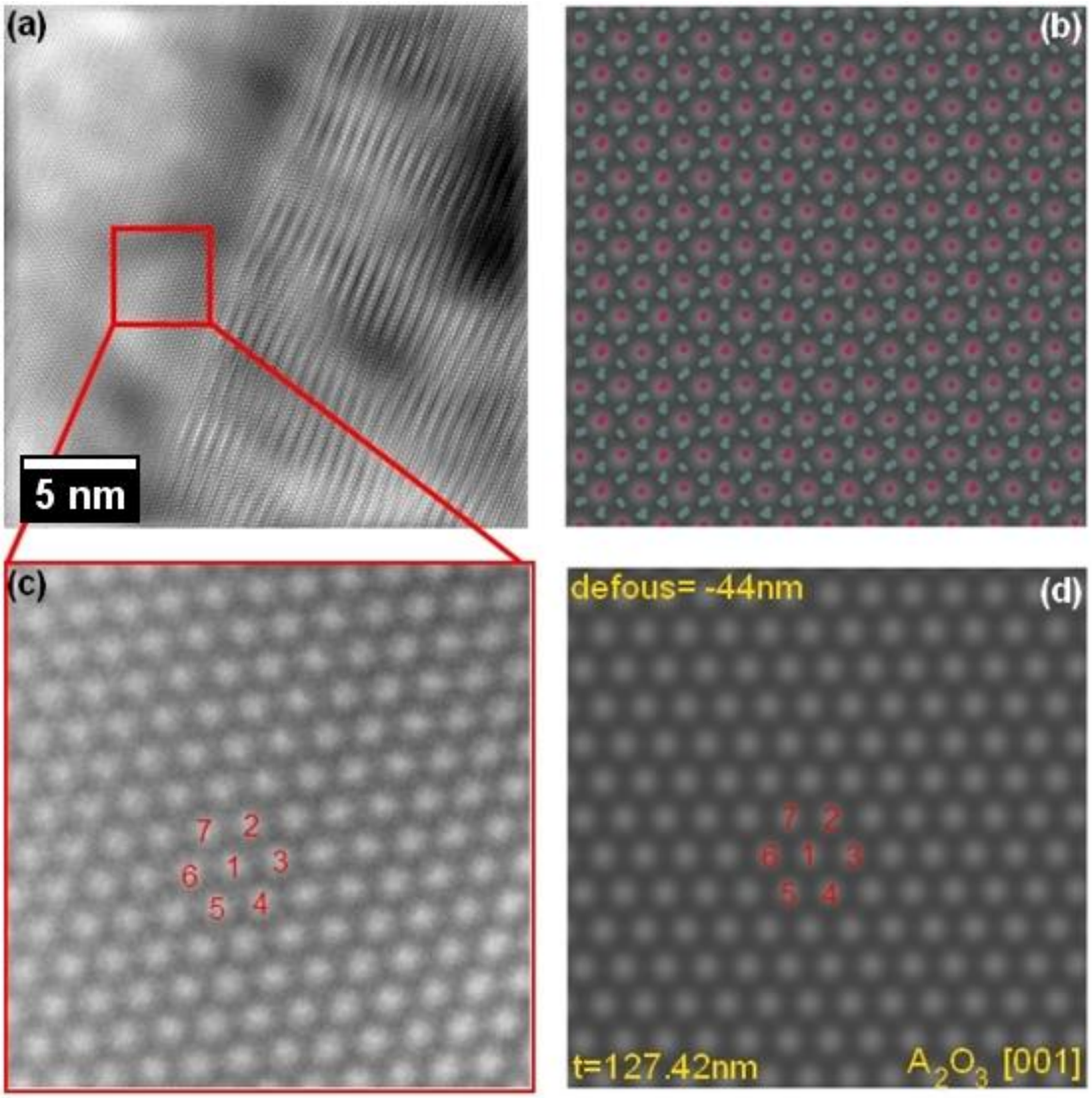


FIGURE 4.19: (a) Reduced noise image obtained after inverse FFT. (b) Image indicating the location of aluminum and oxygen atoms. The red spots are aluminum atoms and the cyan spots are the oxygen atoms. (c) Higher magnification image exposing the aluminum atoms. (d) The result of the multislice simulation with the corresponding defocus and thickness. The images in (c) and (d) are identical meaning that the simulation is good.

## 4.2 NiO-Ti Results

The results of the NiO-Ti study will be presented here. These experimental investigations were performed using light microscopy, XRD, and SEM/EDs techniques. Included will be notes and discussion about the material obtained, since it was a trial and error procedure. The results of each trial will be discussed and explained. The idea was to progressively improve the material quality based on the conclusions obtained after each trial.

### 4.2.1 Trial Run 1

This trial consisted of using a small titanium piece (Ti = 0.1 g) on top of a sintered NiO pellet (1.5 g) in a arc melting furnace in order to react the two constituents.

**Macroscopic observation.**

Figure 4.20 shows stereo microscope micrograph of the cross-sectioned composite embedded into epoxy. This sample can be divided into two main areas: the top area, which did transform, and the bottom area which was sitting on the water cooled cold plate of the arc furnace and did not react with Ti. There are two possible explanations for the presence of non-reacted volume: (1) The bottom plate was too cold for reaction with Ti, and (2) there was not enough Ti to penetrate all the way to the bottom. The only way the Ti will penetrate to the bottom is if cracks are formed and it can leak through. The top where the Ti reacted with NiO looks more reflective and it can be speculated that a metal phase is present.

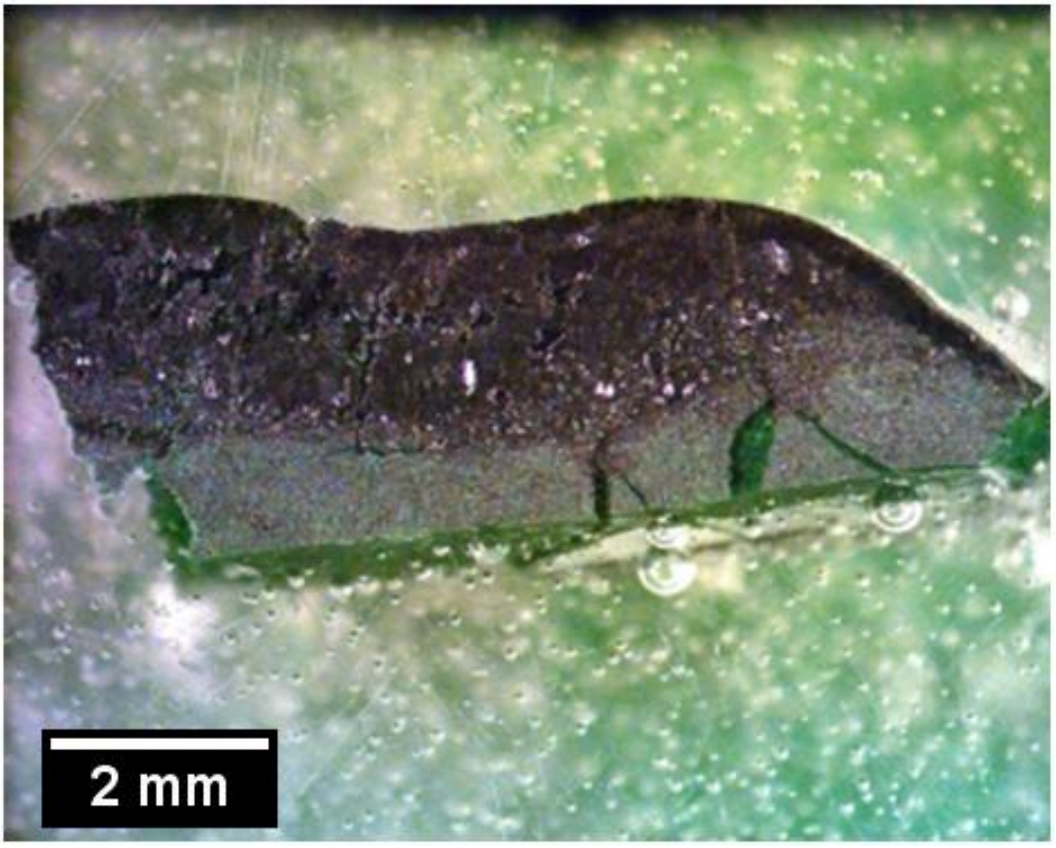


FIGURE 4.20: Macrosopic view of the entire sample fabricated. There seem to be two regions: the bottom region to which the Ti did not penetrate to and the top region which reacted with the Ti.

### Light Microscopy

Bright field light micrographs have been taken from the cross-sectioned composite pellet. At 10x the micrograph reveals that there are two or more phases present in the sample. The brighter phase looks to be metal while the remainder is a porous ceramic. The bright phase looks discrete. At least two phases have been obtained during the reaction. Further investigation has to be done in order to determine the elemental composition of the phases. These micrographs indicate that the desired interconnected networks were not produced throughout the entire sample.

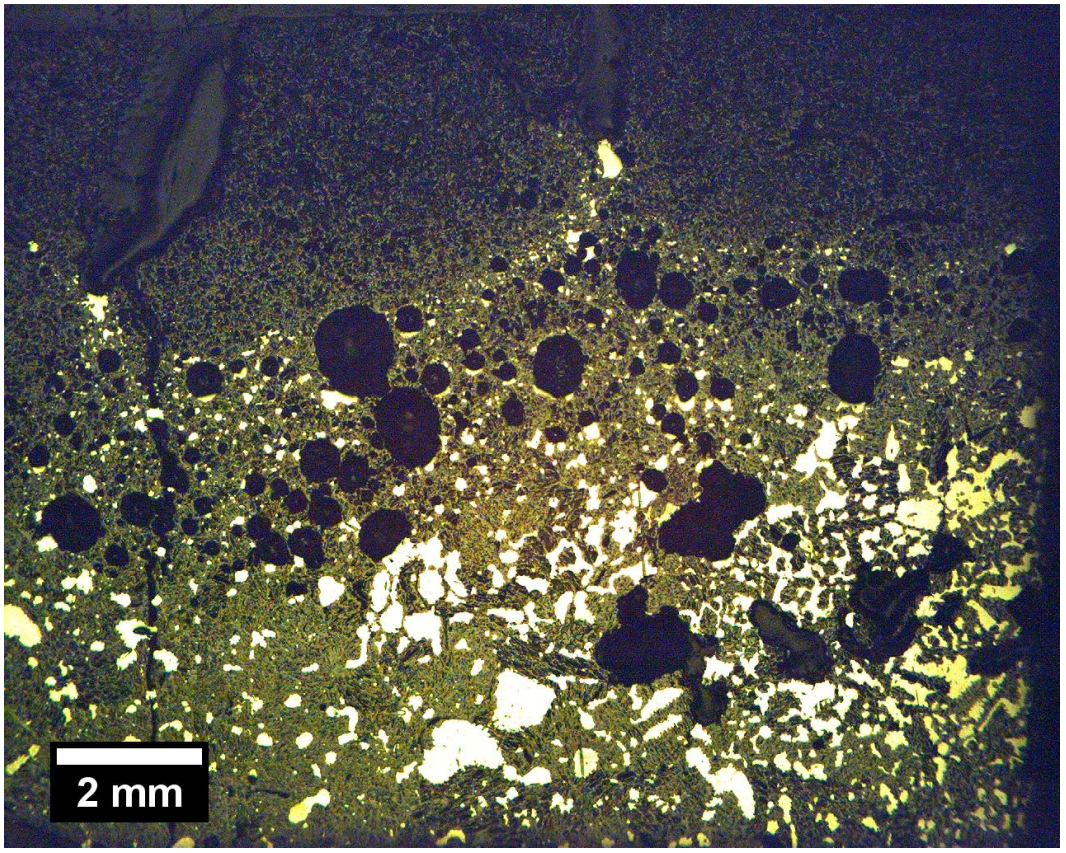


FIGURE 4.21: Bright field light micrograph showing a discrete phase embedded into a continuous ceramic phase.

### XRD Analysis

Powder XRD analysis was done on the cross-section of the sample for 7 hours to find out which phases were present in the bulk material. Three or four phases were identified to be present in the sample, Figure 4.21: Titanium oxide (TiO) and/or nickel oxide (NiO) (their powder XRD patterns are virtually indistinguishable), nickel (Ni) and nickel-titanium oxide ($Ni_3TiO_5$). It was found in literature that the $Ni_3TiO_5$ phase occurs because the sample was quenched. There is some ambiguity in the XRD data between TiO and NiO phase. Both phases match the same peaks since their unit cell parameters and space group are equivalent. XRD analysis cannot distinguish between those two phases. Further analysis has to be employed to find out if only NiO or TiO, or both phases are present in the sample.

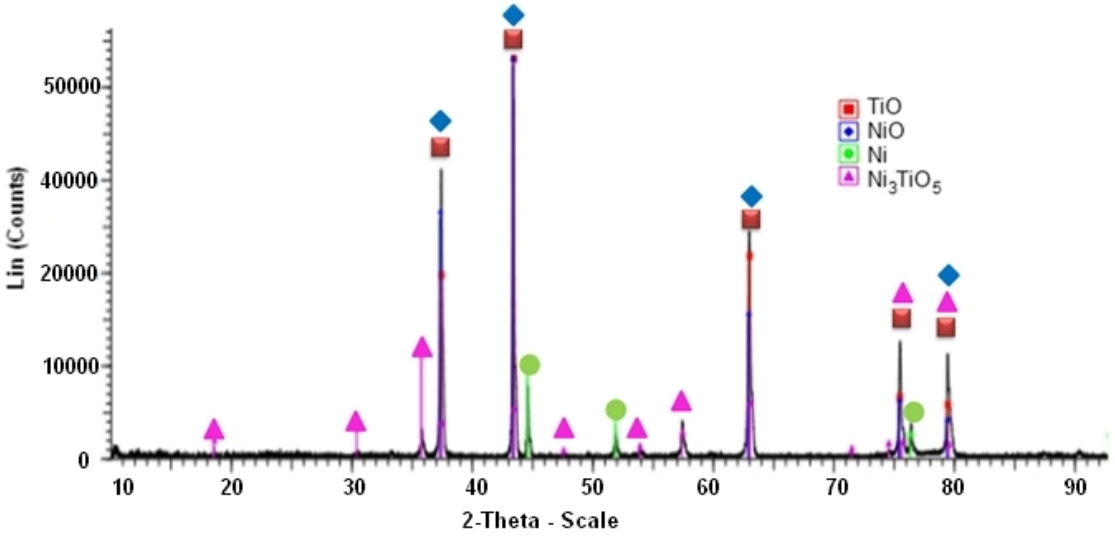


FIGURE 4.22: Powder XRD patterns of a NiO pellet after the reaction with a Ti metal piece. The result shows TiO (ICDD: 00-008-0117, FCC $Fm\bar{3}$ m, a: 4.177Å) and/or NiO (ICDD: 00-047-1049, FCC $FPm\bar{3}m$, a: 4.177Å), Ni (ICDD: 00-004-0850, FCC $Fd\bar{3}m$, a: 3.524Å) and $Ni_3TiO_5$ (ICDD: 00-030-0865, tetragonal $I4_1/amd$, a: 5.894Å, c: 8.336Å).

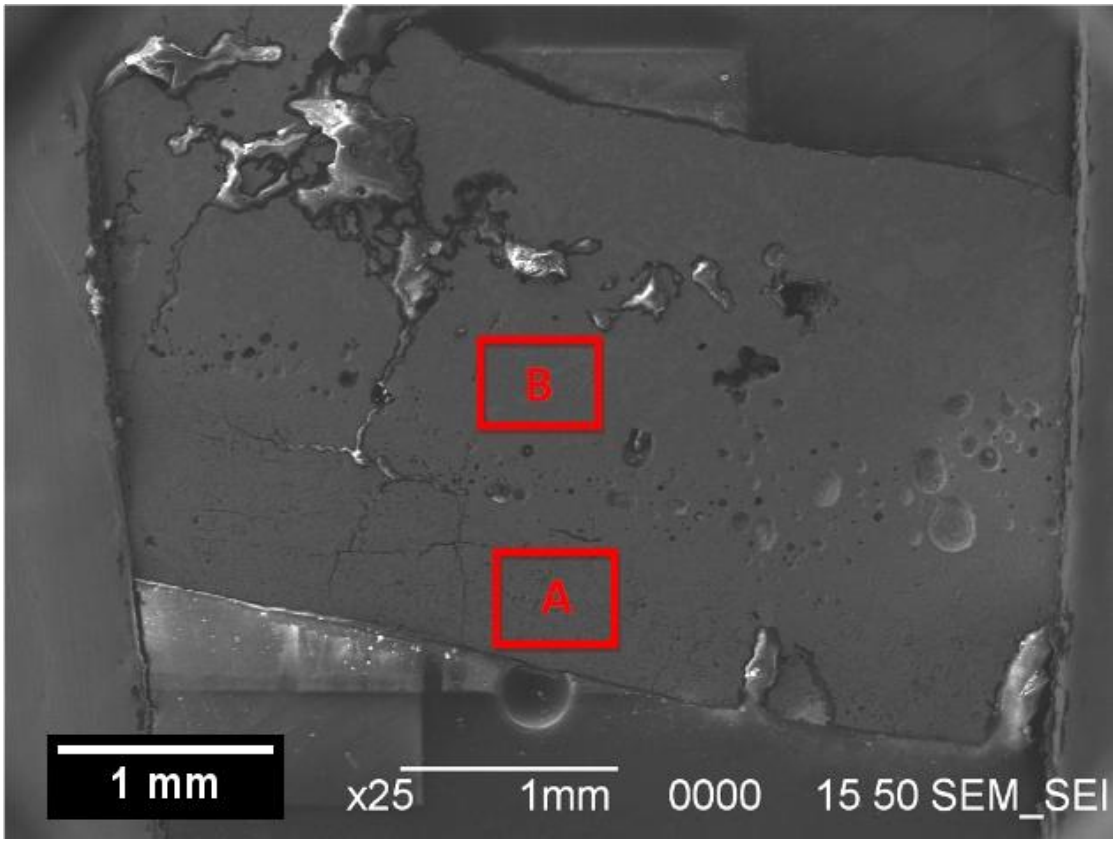


FIGURE 4.23: Low magnification secondary electrons micrograph showing the sample overview. Area A is in the untransformed region and B is in the transformed region.

### Scanning Electron Microscope/EDS Investigations

As discussed previously the sample consists of two distinctive volumes. The bottom of the sample appears to be untransformed NiO (Area A) while the top region (Area B) appears to be the area where the reaction took place, Figure 4.23. In both the transformed and untransformed regions of the sample there are many pores which either opened up during the reaction or were there after sintering. The reaction took place from the top down and slight contrast difference can be seen between the transformed phase and the original ceramic phase.

Figure 4.24 (a) shows the secondary electron micrograph of the cross sectioned untransformed NiO pallet. Many voids can be observed and the sample is quite porous. Figure

4.24 (b) shows and SEM micrograph of cross sectioned transformed sample. This microstructure corresponds to the top volume of transformed sample, Area B in Figure 4.23. This volume seems to be more compact than the untransformed one, and two morphologically different phases can be observed.

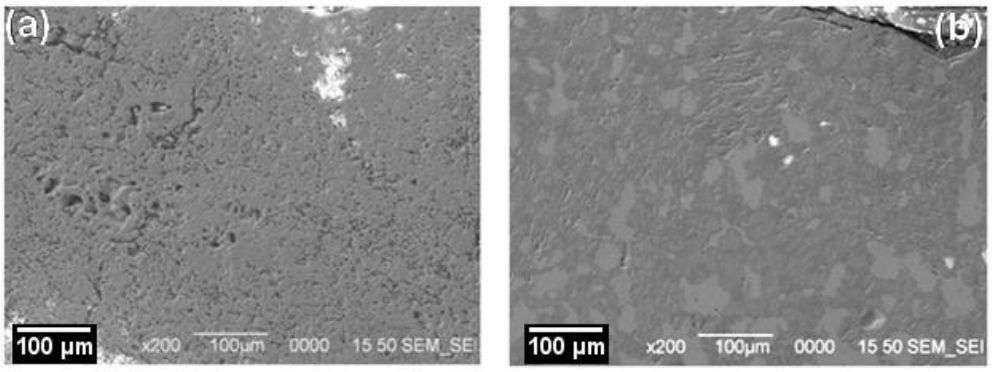


FIGURE 4.24: (a) Secondary electron micrograph of the untransformed NiO pallet. This morphology was also observed on the lower part of transformed sample (Area A in Figure 4.23) which did not participate in the reaction with titanium. (b) Electron micrograph from transformed sample, Area B in Figure 4.23.

Figure 4.25 is a higher magnification electron micrograph of the transformed sample. Two distinctive phases, A and B, can be readily observed. In order to determine the chemistry of the two phases back scattering electron imaging and EDS analysis were used, Figures 4.26 and 2.27, respectively. Based on the EDS analysis and correlating with XRD information, one metallic and there ceramic phases were observed. The metal phase is pure Ni, while the ceramic phases are TiO, NiO and $Ni_3TiO_5$.

An EDS elemental map was produce to see the elemental distribution in the sample, Figure 4.28. The change in the Ti concentrations can be seen well in the map, the darkest section has the most Ti which is confirmed with the EDS map. The map also shows clearly the pure nickel section ,in blue, in this case. Oxygen can be found everywhere, besides the pure Ni sections, meaning that most of the phases obtained by this reaction are possibly ceramic with pure nickel volumes in between.

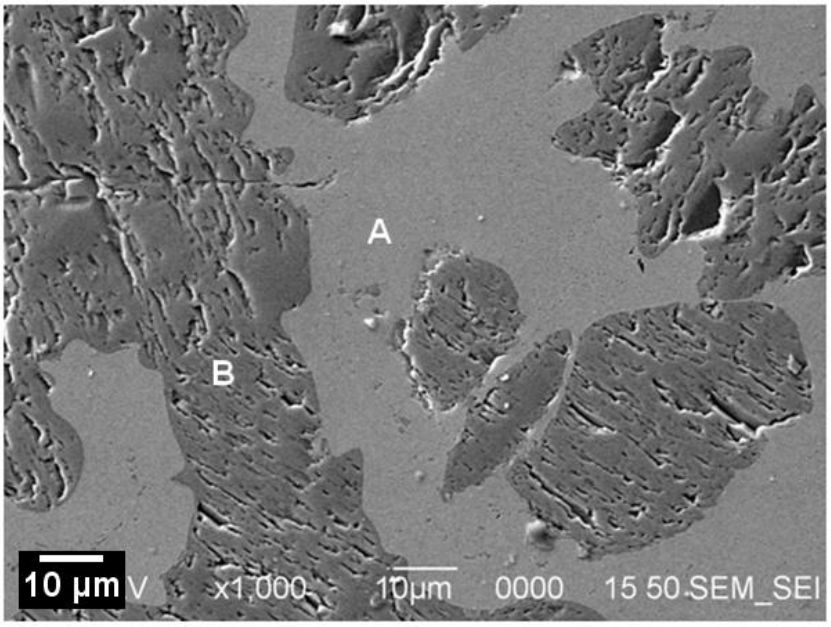


FIGURE 4.25: Electron micrograph of the transformed sample. Two distinct phases can be clearly seen: a compact metal phase (A), and a porous ceramic (B).

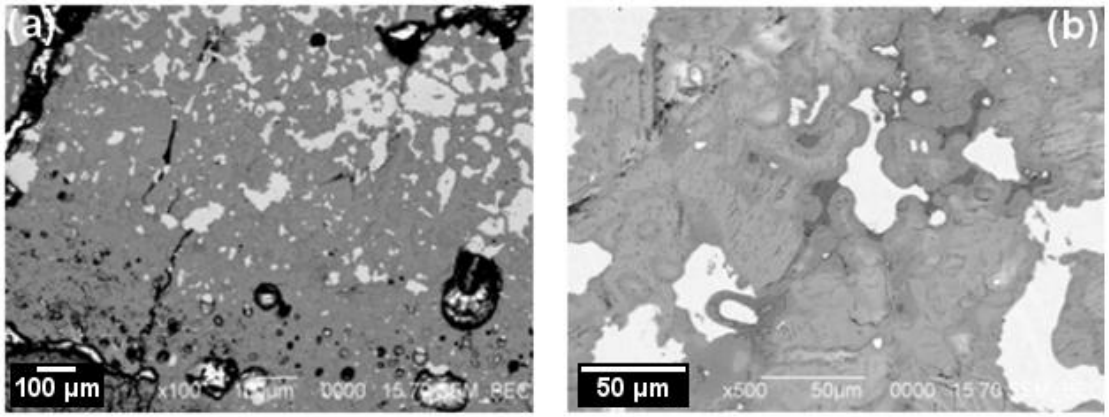


FIGURE 4.26: (a) Backscatter electron micrograph showing the discrete nature of the second phase within the ceramic matrix. (b) Higher magnification micrograph showing shades of grey which correspond to different elemental compositions

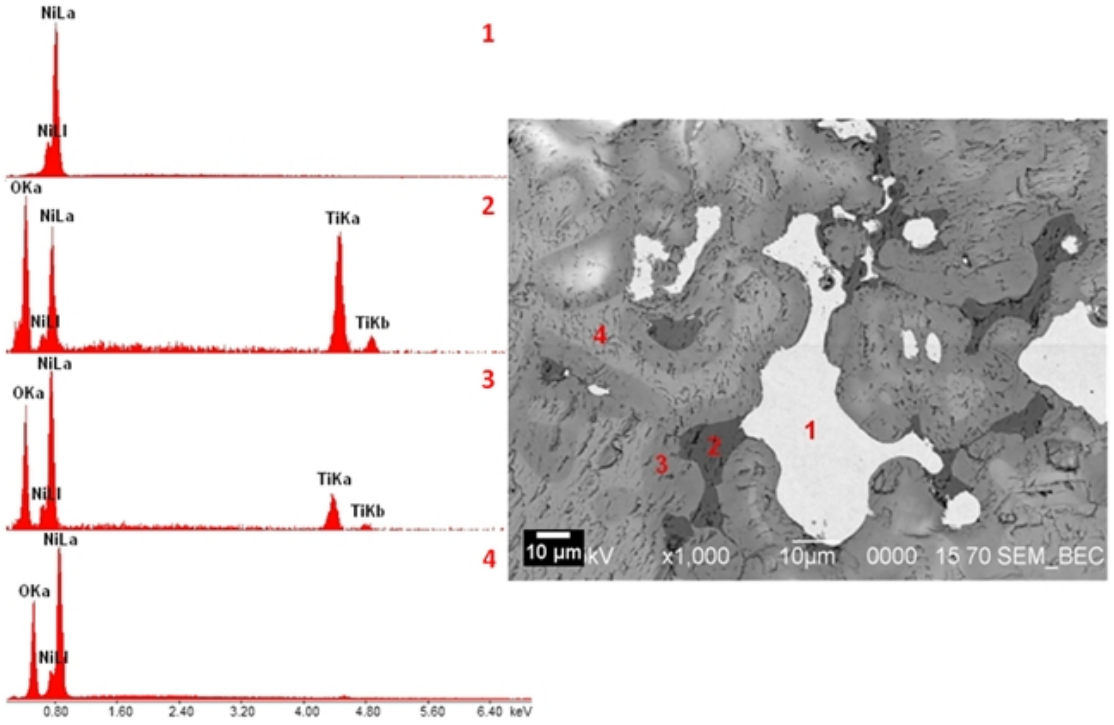


FIGURE 4.27: Backscattered electron micrograph showing four distinct shades, which correspond to a pure Ni metal phase and different ceramic phases, as determined by EDS. The brightest sections are pure nickel, and the darker shades have increasing concentrations of Ti: (1) Pure nickel, (2) TiO (could also be amorphous $TiO_2$), (3) $Ni_3TiO_5$, and (4) NiO.

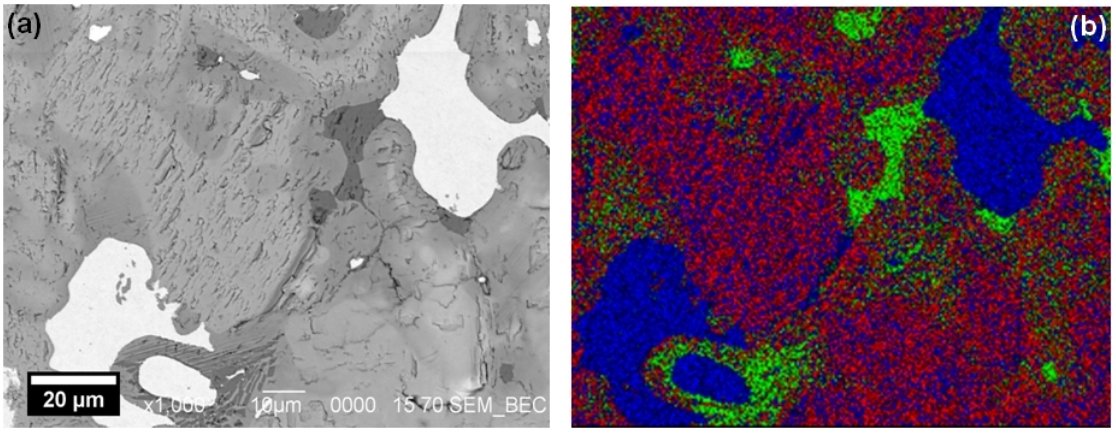


FIGURE 4.28: (a) Backscatter electron micrograph, and (b) corresponding EDS elemental map. Color code: Ni-Blue; Ti-Green, Oxygen- Red.

The first trial consisted of small amounts of Ti and a large NiO pellet. For the next trial it was decided that a larger Ti piece will be used in order to completely react with the NiO pellet. The first trial only produced small amounts of Ti-based phases and maybe if there is more titanium in the reaction larger Ti based phases might form. In the first trial attempt, the NiO pallet was incompletely transformed following the reaction with Ti, but the experiment provided some interesting results.

### 4.2.2 Trial Run 2

In this trial a larger piece of titanium (Ti = 1.00 g) was placed on top of a sintered NiO pellet (NiO = 2.01 g). During synthesis in the arc melting furnace a violent exothermic (thermite) reaction took place between Ti and NiO. The ceramic and metal separated, and in the resulting sample the metal was at the core while the ceramic peeled away from the metal core. The result was one solid metal core surrounded by flakes of ceramic. This observation is similar as reported by Kobayashi *et al.*[50], when due to a high Ti content the samples exploded. This reaction can be explained by the following stoichiometric equation:

$$2NiO + Ti \rightarrow 2Ni + (phase) + TiO_2 + \Delta G$$

where ΔG is the Gibbs free energy, which can be calculated by

$$\Delta G = \sum G_{products} - \sum G_{startingmaterial}$$

$$\Delta G_{products} = 2\,[0]_{Ni} + \left[-944\frac{kJ}{mol}\right]_{TiO_2} = -944\frac{kJ}{mol}$$

$$\Delta G_{startingmaterial} = 2\left[-244.3\frac{kJ}{mol}\right]_{NiO} + [0]_{Ti} = -488.6\frac{kJ}{mol}$$

$$\Delta G_{total} = -455.4 \frac{kJ}{mol}$$

As expected the value for the Gibbs free energy is highly negative, indicating a strong exothermic reaction which agrees with the experimental observation. Ti is very oxophilic and therefore as soon as the reaction mixture reaches a critical temperature the reaction becomes uncontrollable. The nickel metal formed in the reaction clumps together in one piece and the ceramic formed clusters around this core. It can be concluded that small Ti amounts have to be used to avoid a runaway reaction. In the next trial the Ti amount was reduced in order to avoid runaway reactions.

### 4.2.3 Trial Run 3

This trial consisted of using a titanium piece (Ti = 0.226 g) on top of a sintered NiO pellet (NiO = 2.01 g). Since the reaction is spontaneous, it can be started by heating up the Ti just enough and let the reaction self-propagate through the energy released by the exothermic reaction. The result of this trial was one solid sample; the exothermic reaction did not destroy this sample like in trial run 2. This result was very similar as in trial run 1 and therefore will not be discussed again.

### 4.2.4 NiO-TiO Pellet Trials

Ti reacts violent with the oxygen in the NiO pellets. A diluting agent has to be used in order to slow down the process and avoid a runaway reaction. After some consideration $TiO_2$ (rutile) was decided upon. This compound was selected for two reasons. First, titanium (II) oxide (TiO) is a constituent in the transformed material (see XRD results) and it was hypnotized that by rutile addition the NiO mass in the sintered palled will be reduced such as the thermite reaction will be slow down. Second, rutile was available in the laboratory. The same procedure was used for making the pallets, but the staring powder mixture was 50wt.% NiO and 50wt.% $TiO_2$ pellets. Since all parameters were

kept constant, any change to the final product will be a direct consequence of the different composition of the pellet.

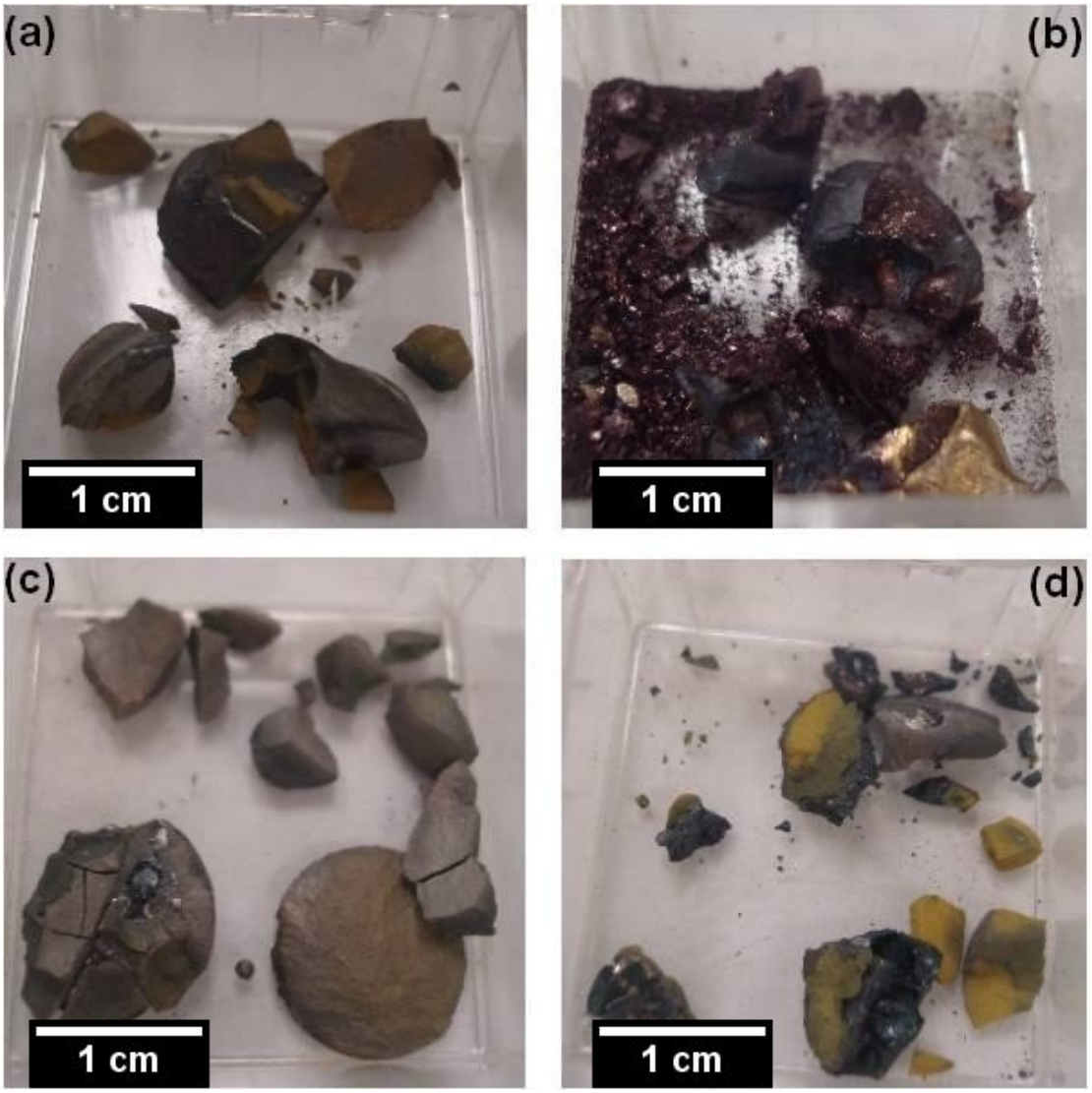


FIGURE 4.29: Four different trials of Ti reacted with 50 wt.% NiO/50 wt.% $TiO_2$ pallets. The Ti amount was varied but the final material was very brittle in all trials attempted so far. NiO/$TiO_2$ pallet reacted with (a) 0.1261 grams (Sample 5), (b) 1.0218 grams (Sample 7) (c) 0.1430 grams (Sample 6), and 0.2613 grams (Sample 4) of Ti. Details regarding pellets condition can be seen in Table 3.3.

As seen in Figure 4.29, every sample produced with 50wt.% $TiO_2$ and 50wt.% NiO starting pellets resulted in formation of a brittle material and disintegration of the pellet. The brittle nature of the final product was regarded as a consequence of using

$NiO/TiO_2$ powders mixture as starting materials, and no further analysis was done on these samples.

A pure $TiO_2$ pellet and was also reacted with Ti in order to explore this avenue, as well. As expected the reaction produced a brittle product. Therefore, it seems that that the brittle nature in the 50 wt.% NiO/50 wt.% $TiO_2$ pellet was caused by the addition of $TiO_2$. The addition of $TiO_2$ to the starting pellet did not aid in the production of the desired IPC. Thus, another agent has to be found in order to slow down the reaction between NiO and Ti.

### Final Remark

The fabrication of Ti-based ceramic-metal IPCs by reactive metal penetration method is a challenging task. The theoretical method to produce an IPC with NiO-Ti does not work as proposed by Liu and Köster[31] in their paper. The sacrificial oxide NiO does react with the molten Ti but does not produce a desired IPC as theoretically proposed. This could be due to the difficult to control nature of the NiO-Ti thermite reaction. If possible at all, a different method has to be used to fabricate this material. The best trial run was NiO palets with small amounts of pure Ti, but with the limitation of having non-continues phases within each other throughout the sample.

# Chapter 5

# Conclusion

## 5.1 Fireline Material

A complete material phase characterization on the ceramic-metallic IPCs produced by reactive metal penetration (RMP) was performed. The material was manufactured by Fireline Inc. of Youngstown, OH by immersing CFQ pre-forms into molten aluminum alloy melt containing 7.5wt.% Fe at 1200°C for 4.63 hours. The present work completes the analytical investigation of Fireline material started by a previous graduate student using light and scanning electron microscopy. The nano-scale investigation of Fireline materials, done by using scanning and transmission electron microscopy techniques include complete structure assignment, unique orientation relationships, and an HREM investigation of silicon particles.

Through electron diffraction techniques the exact structure and compositions of the inter-metallic phases was determined. In the TCON material the following phases were found to be present: Al (cubic), $Al_2O_3$ (trigonal), $Al_{13}Fe_4$ (C-centered monoclinic), and $Al_4Fe_{1.7}Si$ (hexagonal). Hence, any material fabricated in this manner will consist of these phases. Next, unique orientation relationships have been obtained between the assigned phases. The relationship between alumina and aluminum was found to

be $[\bar{1}00]_{Al_2O_3}$ // $[310]_{Al}$ and $(006)_{Al_2O_3}$ // $(002)_{Al}$. The relationship between the alumina and the binary $Al_{13}Fe_4$ phase was determined to be $[1\bar{1}1]_{Al_2O_3}$ // $[\bar{4}03]_{Al_{13}Fe_4}$ and $(\bar{1}23)_{Al_2O_3}$ // $(31\bar{1}4)_{Al_{13}Fe_4}$. Lastly, an orientation relationship was found between the alumina and the ternary $Al_4Fe_{1.7}Si$ ($\tau$") phase to be $[4\bar{4}\bar{1}]_{Al_2O_3}$ // $[120]_{\tau''}$ and $(\bar{1}\bar{1}0)_{Al_2O_3}$ // $(\bar{6}3\bar{6})_{\tau''}$. These orientation relationship show the manner in which these phases accommodate to each other. Silicon inclusions have been also observed in the TCON samples. The most interesting feature in the silicon inclusions is the modulation that was observed. It is hypothesized that the silicon was squeezed by the surrounding grains upon cooling and the modulation was caused by the silicon trying to accommodate to the smaller space. This observation was verified by simple thermal expansion coefficient analysis. The analysis shows that silicon contracts the least compared to aluminum and alumina. Therefore it is possible that the silicon particle was squeezed by the surrounding matrix, resulting into a crystal having commensurate modulated structure.

It is suggested that future work concentrates on the transformation mechanism. A complete understanding of how the interpenetrating phases are formed during the RMP processes will be useful in optimizing the final product. The transformation mechanism is much more complex then previously thought and this study revealed some insight into silicon grains nucleation and growth during the transformation. Since silicon solubility in aluminum is very limited most silicon diffuses out of the metallic phase, and pure silicon grains having a modulated crystal structure forms in the voids of interpenetrated phase composite. Regarding the formation of alumina and metallic phases more investigation has to be done on partially transformed samples using the TEM to gain more insight on the transformation mechanism.

Furthermore, future work should address the crystallography and the role of the buffer layer between $Al_2O_3$ and Al14Fe3. It seems that the ternary Al-Fe-Si phase, having hexagonal structure, accommodates the crystallographic mismatch observed in between the alumina phase (trigonal structure) and the binary Al-Fe metal phase having a C-centered monoclinic structure. More TEM samples have to be produced using FIB

techniques in order to investigate wheather the Al-Fe-Si ternary phase accompanies the $Al_{13}Fe_4$ phase everywhere in the material.

In conclusion, the 7.5 weight percent Fe-alloy addition to the Al melt caused the formation of an $Al_{13}Fe_4$ phase and a ternary $\tau''$ ($Al_4Fe_{1.7}Si$) phase in the composite material. Orientation relationship investigation shows a perfect match between the crystalline structures of most of the ceramic and metallic phases with the exception of $Al_{13}Fe_4$ and $Al_2O_3$ phases. The HREM investigation shows the existence of an Al-Fe-Si buffer layer between $Al_2O_3$ and $Al_{13}Fe_4$. Finally, the silicon particles observed in the sample have a modulated crystallographic structure. While more research is necessary to determine the exact transformation mechanisms, the TEM analysis present in this thesis helped further the knowledge of ceramic-metallic interpenetrating phase composites.

## 5.2 NiO-Ti material

An attempt has been made to fabricate interpenetrating phase composites with a shape memory alloy phase for damping application. NiO pellets have been reacted with Ti under inert gas atmosphere using an arc furnace. In theory, interpenetrated phase composites containing TiO ceramic and Ni-based metallic phases could be formed by reactive melt penetration. In this research it was attempted to obtain NiTi as a metallic phase. NiTi is a well known shape memory alloy which can provide superior damping properties to the ceramic-metallic IPCs. Combinations of different starting materials have been tried in order to obtain the desired final product.

The NiO pellets reacted with Ti and produced a discrete network of nickel metal embedded in the ceramic matrix. Other phases such as Ni, TiO, and $Ni_3TiO_5$ were also formed. The formation of NiTi phase failed due to the extremely exothermic reaction of titanium with oxygen. Further attempts have been made by modifying the initial pellet composition by adding $TiO_2$ to the initial NiO preform. This mixture performed worse and resulted in brittle material which falls apart as soon as taken out of the arc furnace.

The brittleness of the obtained composite seems to be due to the addition of $TiO_2$ to the NiO. The most compact material was obtained by using NiO pellet as starting material. However, the final product contained no NiTi phase.

It is suggested that future work concentrates on finding an agent that will slow down the reaction between titanium and oxygen with the intention of have a less violent thermite reaction. Having a less violent reaction will possibly allow the Ti and Ni inside the material to combine into a NiTi shape memory alloy phase. Another possibility is to change the process all together and use a multi-layer approach to achieve the envisioned product. This would require stacking alternating layers of NiO and Ti together. This layered stack would then be exposed to heat and would react. The layer approach would prevent large amounts of Ti of reacting with NiO causing the violent thermite reaction. In order to obtain NiTi metallic phase having shape memory property the infiltration step has to be done under inert gas atmosphere in order to prevent titanium from oxidizing.

In conclusion, the envisioned IPC was not obtained. While more research is necessary to achieve the desired final product, it has been shown that using a pellet of NiO and a piece of metal Ti inside an arc furnace will not fabricate a shape memory interpenetrating phase composite material, under the present experimental conditions. Synthesis of such a composite material seems to be challenging and difficult to achieve using reactive melt penetration process, and alternative fabrication routes have been suggested.

# Chapter 6

# References


1. Breslin, M. C., Ringnalda, J., Xu, L., Fuller, M., Seeger, J., Daehn G. S., Otani T., and Fraser, H. L. (1995). Processing, microstructure, and properties of co-continuous alumina-aluminum composites, Materials Science and Engineering, vol. A195, 113-119.

2. San Marchi, C., Kouzeli, M., Rao, R., Lewis, J.A. and Dunand, D.C. (2003). Alumina-aluminum interpenetrating-phase composites with three-dimensional periodic architecture. Scripta Materialia, vol. 49(9), 861-866.

3. La Vecchia, G., Badini, C., Puppo, D. and D'Errico, F. (2003). Co-continuous $Al/Al_2O_3$ composite produced by liquid displacement reaction: Relationship between microstructure and mechanical behavior. Journal of Materials Science, vol. 38, 3567-3577.

4. Hemrick, J.C., Hu, M.Z., Peters, K.M. and Hetzel, B. (2010). Nano-Scale Interpenetrating Phase Composites (IPCs) for Industrial and Vehicle Application. (ORNL/TM-2010/80) Oak Ridge, TN.

5. Paul, R. (2007). Microstructural and Chemical Characterization of Interpenetrating Phase Composites as Unique Refractory Materials Produced Via Reactive

Metal Penetration. Master's Thesis, Youngstown State University, Youngstown, OH U.S.A.

6. Schicker, S, Gracia, D.E., Bruhn, J, Janseen, R, and Claussen, N. (1997). Reaction Processing of $Al_2O_3$ Cmposites Containing Iron Aluminides. American Journal of Ceramics, vol. 80, 2294-2300

7. Kim, J.S., Kwon, Y.S., Lomovsky, O.I., Korchagin, M.A., Mali, V.I. and Dudina, D.V. (2006). A synthetic route for metal-ceramic interpenetrating phase composites. Material Letters, vol. 60, 3723-3726.

8. Plam, M. Concepts Derived from Phase Diagram studies for the Strengthening of Fe-Al-based alloys. Intermetalics, vol. 13, 1286-1295.

9. Yoshikawa, N., Hattori, A. and Taniguchi, S. (2003). Growth rates and microstructure of reacted layers between molten Al-Fe alloy and $SiO_2$. Materials Science and Engineering, vol. 342(A), 51-57.

10. Murthy, V.S.R., Kawahara, K., Saito, Y., Matsuzaki, T. and Watanabe, T. (2005). Orientation and Grain Boundary Microstructure of Alumina in $Al/Al_2O_3$ Composites Produced by Reactive Metal Penetration. Journal of the American Ceramic Society, vol. 88(10), 2902-2907.

11. Yurcho, A. (2011). Microstructural Investigation of Al/Al-Fe alloy-$Al_2O_3$ Interpenetrating Phase Composites Produced by Reactive Metal Penetration. Master's Thesis, Youngstown State University, Youngstown, OH U.S.A.

12. Thermite. (2005). In Amazing Rust.com International Chemical Supply . Retrieved December 26, 2012, from http://www.amazingrust.com/Experiments/how_to/Thermite.ht

13. Xi, W., Zhou, H., Ma, C., Duan, H. and Zhang, T. (2007). Thermodynamic analysis of thermite reactions for synthesizing Ni-based alloys. Journal of Materials Science, vol. 42(20), 8489-8495.

14. Wang, L.L., Munir, Z.A. and Maximov, Y.M. (1993). Thermite reactions: their utilization in the synthesis and processing of materials. Journal of Materials Science, vol. 28, 3693-3708.

15. Daehn, G.S. and Breslin, M.C. (2006) Co-continuous composite materials for friction and braking applications. Journal of the Minerals, Metals and Materials Society, vol. 58(11), 87-91.

16. Ebrahimi-Kahrizsangi, R., Torabi, O. Combination of Mechanochemical Activation and Self-Propagating behavior for the Synthesis of Nanocomposite $Al_2O_3/B_4C$ powder. Journal of Alloys and Compounds, (2011).

17. Kim, J.S., Kwon, Y.S., Lomovsky, O.I., Korchagin, M.A., Mali, V.I. and Dudina, D.V. (2006). A synthetic route for metal-ceramic interpenetrating phase composites. Material Letters, vol. 60, 3723-3726.

18. Feng, H. J. and Moore, J. (1995). In situ combustion synthesis of dense ceramic and ceramic-metal interpenetrating phase composites. Metallurgical and Materials Transactions B, vol. 26(2), 265-273.

19. Hu, Q., Luo, P. and Yan, Y. (2007). Influence of an electric field on combustion synthesis process and microstructures of TiC-$Al_2O_3$-Al composites. Journal of Alloys and Compounds, vol. 439, 132-136.

20. Mattern, A., Huchler, B., Staudenecker, D., Oberacker, R., Nagel, A. and Hoffmann, M.J. (2004). Preparation of interpenetrating ceramic-metallic composites. Journal of European Ceramic Society, vol. 24, 3399-3408.

21. Manfredi, D., Pavese, M., Biamino, S., Fino, P., Badini, C. (2008). NiAl(Si)/$Al_2O_3$ co-continuous composites by double reactive metal penetration into silica preforms. Intermetallics. 16, 580-583.

22. Brondyke,K.J. (1953) Effect of Molten Aluminum on Alumina-Silica Refractories. Journal of the American Ceramic Society, vol. 36,5, 171-174.

23. George, H. (1955). Manufacture of Articles from Substances Containing Silica. U.S. Patent No. 2,702,750.

24. Stadage and Gani.(1967) Reaction between Vitreous Silica and Molten Aluminum. Journal of the American Ceramics Society, vol. 50, 101-105.

25. Aghajanian, M.K. and Newkirk, M.S. (1992). Aluminum Metal Matrix Composites. U.S. Patent No. 5,298,339.

26. Grimshaw, R.W. and Poole, C. (1980). Composite Materials and Their Production. U.S. Patent No. 4,232,091.

27. Breslin, M.C. (1993). Process for Preparing Ceramic-Metal Composite Bodies. U.S. Patent No. 5,214,011.

28. Breslin, M.C., Transformation Kinetics of $Al_2O_3$/Al Co-Continuous Ceramic/Metal Composite Materials (C4) Produced by a Displacement Reactoin Between Liquid Al and Fused $SiO_2$, Master's thesis, The Ohio State University, 1994.

29. Daehn, G.S., Starck,B., Xu,L., Elfishawy,K.F., Ringnalda,J., and Fraser, H.L. (1996) Elastic and Plastic Behavior of a Co-Continuous Alumina/Aluminum Composite. Acta Metallurgica, vol. 44, 249-261.

30. Liu, W. and Köster, U. (1996). Criteria for formation of interpenetrating oxide/metal-composites by immersing sacrificial oxide preforms in molten metals. Scripta Materialia, vol. 35(1), 35-40.

31. Zhou, W., Hu, W., and Zhang, D. (1998). Study on the making of metal-matrix interpenetrating phase composites. Scripta Materialia, vol. 39(12), 1743-1748.

32. Ha, C. Jung, Y., Paik, U. (2000). Effect of microstructure on fracture behavior of $Al_2O_3$/Al Composite by reactive metal penetration. Journal of Alloys and Compounds, vol. 306, 292-299.

33. Banerjee, S., Roy, S.K. (2001). Net-Shape Forming of Bi-Continuous $Al_2O_3$/Al Composite by Displacement Reaction. Materials Chemistry and Physics vol. 67, 243-248.

34. Murthy, V.S.R., Kawahara, K., Saito, Y., Matsuzaki, T. and Watanabe, T. (2005). Orientation and Grain Boundary Microstructure of Alumina in $Al/Al_2O_3$ Composites Produced by Reactive Metal Penetration. Journal of the American Ceramic Society, vol. 88(10), 2902-2907.

35. Mei, J., Halldearn, H.D. and Xiao, P. (1999). Mechanism of the aluminum-iron oxide thermite reaction. Scripta Materialia, vol. 41(5), 541-548.

36. Marumo , C., Pask, J.A. (1977). Reactions and Wetting Behaviour in the Aluminum-fused Silica System, Journal of Materials Science, vol. 12, 223-233.

37. Sundman, B.,Ohnuma, I., Dupin, N., Kattner, U., Fries, S. (2009). An assessment of the entire Al-Fe system including D03 ordering. Acta Materialia 57 2896-2908.

38. Guinebretière, R. (2007). X-ray Diffraction by Polycrystalline Materials. Newport Beach, CA: ISTD, Ltd.

39. Royset, J., Leinum, J.R., Overlie, H.G. and Reiso, O. (2006). An Investigation of the Solubility of Scandium in Iron-bearing Constituent Particles in Aluminium Alloys. Materials Science Forum, vol. 519-521, 531-536.

40. Bialas, H. and Stolz, H.J. (1975). Lattice dynamics of sapphire (corundum), Part I: Phonon Dispersion by Inelastic Neutron Scattering. Zeitschrift für Physik B Condensed Matter and Quanta, vol. 21(4), 319-324.

41. Kaushish, J.P. (2010). Manufacturing Processes. Second Edition. New Dehli: PHI Learning Private Limited.

42. Liu, Z.K. and Chang, A. (1999). Thermodynamic Assessment of the Al-Fe-Si System. Metallurgical and Materials Transactions A, vol. 30A, 1081-1095.

43. Cizek, P. (2006). Electron microscopy investigation of the TiBAl and TiCAl grain refiner master alloys, Journal of Physics, vol. 26, 107-110.

44. Rapp, R.A., Ezis, A. and Yurek, G.J. (1973). Displacement Reactions in the Solid State. Metallurgical Transactions, vol. 4, 1283-1292.

45. National Bureau of Standards, US. (1981). Monogr. 25(18), 5.

46. Raghaven, V. (2002). Al-Fe-Si (Aluminum-Iron-Silicon). Journal of Phase Diagram Equilibria and Diffusion, vol. 32(2), 140-142.

47. Subramanian, R., McKamey, C., Buck, L. and Schneibel, J. (1997). Synthesis of iron aluminide-$Al_2O_3$ by in-situ displacement reactions. Materials Science and Engineering, vol. A239-240, 640-646.

48. Chu , C.L. ,Chung ,C.Y., Lin, P.H., S.D.Wang. (2004). Fabrication of Porous NiTi Shape memory alloy for hard tissue implants by combustion synthesis. Material Science and Engineering, vol. 366, 114-119.

49. Peterseim, J. (1992). Shape Memory Alloy. U.S. Patent No. 5,108,523.

50. Kobayashi, Y., Kobashi, M., Kanetake, N. (2007). Fabrication of Oxide Ceramics Composite by Reactive Infiltration Process. Advanced Material Research, vol. 26, 321-324.

51. K. Otsuka and C. M. Wayman, Eds., Shape memory materials. Cambridge University Press (1998).

52. J. Van Humbeeck. (2003). Damping capacity of thermoelastic martensite in shape memory alloys, Journal of the Alloy and Compounds, vol. 355, 58-64.

53. LIDE, D.R. CRC Handbook of Chemistry and Physics, 85ed, 2004.

54. Edmund Bühler GmbH. (2010). Operating Instructions: Mini Arc Melting System MAM-1.

55. Williams, D.B. and Carter, C.B. (2009). Transmission Electron Microscopy: A Textbook for Materials Science, Part 1-4. New York, NY: Springer Science and Business Media, LLC.

56. Koch, C. (2002). Determination of Core Structure Periodicity and Point Defect Density Along Dislocations, Dissertation, Arizona State University.

57. Cowley, J. (1981). Diffraction Physics. North-Holland Publishing Company.

58. Stadelmann, P.(2010). jEMS Instruction Manual.

59. Doreset, D.L. (1995). Structural Electron Crystallogrpahy. Plenum Press.

60. Champness, P.E. (2001). Electron Diffraction in the Transmission Electron Microscope. BIOS Scientific Publisher Limited.

61. Scheerschmidt, K., Werner, M. (2005). Carbon at Si(111)-Twins TEM Analysis Supported by Molecular Dynamics Structure Relaxations. Physica status Solidi, vol. 202, 2368-2375.

62. Aluminum Oxide Powder Diffraction File; International Centre for Diffraction Data: Newtown, PA, 2012; PDF# 00-010-0173 (accessed Jan 2012).

63. Aluminum Powder Diffraction File; International Centre for Diffraction Data: Newtown, PA, 2012; PDF# 00-004-0787 (accessed Jan 2012).

64. Silicon Diffraction File; International Centre for Diffraction Data: Newtown, PA, 2012; PDF# 00-010-0173 (accessed Jan 2012).

65. Aluminum Iron Powder Diffraction File; International Centre for Diffraction Data: Newtown, PA, 2012; PDF# 00-050-0797 (accessed Jan 2012).

66. MRS Bulletin. Science and Technology of Shape-Memory Alloys: New Developments. February 2002, 27, 2.

67. Miyazaki, S., Otsuka, K., Suzuki, Y. (1981). Transformation Pseudoelasticity and Deformation Behavior in a Ti-50.6at%Ni Alloy Scripta Metallurgica, vol. 15, no. 3, 287-292.

68. Hernandez, K., Rendziniak, D., Ragan, N., Stahl, B., Rebraca, H., Zeller, M. (2012). Extraction and Characterization of Intermetallic Fe-Al particles from Aluminum Alloys, Youngstown State University Quest Poster, Youngstown, OH U.S.A.

69. a) Sato, K. & Izumi, I. (1984). Bunseki Kagaku 33, 495-498. b) Sato, K. & Izumi, I. (1985). Mater. Charact. 37, 61-80. c) Gupta, A.K. Marois, P.H. & Lloyd, D.J. Mater. (1996) Charact. 37, 61-80.

70. Ma, X., Libertz, H., Köster, U. (1996). Multiple Twins of Monoclinic $Al_{13}Fe_4$ Showing Pseudo-Orthorhombic and Fivefold Symmetries. Phys. Stat. Sol., vol. 158, 359-367.

71. M. Ellner. (1995). Acta cryst. B51, 31.

72. Black, P. (1966). Acta Cryst, 8, 43-48.

73. Bártová, B., Vojtěch, V., Verner, J., Gemperle, A., Studnička, V. J. (2005). Alloy. Comp.,387, 193-200.

74. Grin, Y., Burkhardt, U., Ellner, M., Peters, K. Z. Krist. (1994). 209, 479-487.

75. Smith, D. (1975). ICDD Grant-in-Aid .

76. ASM International. (1995). Handbook of Ternary Alloy Phase Diagrams.

77. Standage, J. Am. Ceram. Soc. vol. 50 No. 2 pp. 101-105 (1967).

78. Prabriputaloong. (1973). Journal of American Ceramic Society. pp. 184-185.

79. Newkirk. (1987) Annual Conference on Composites and Adv. Ceram. Mat.

80. Wagner, T., Schönleber, A. (2009). A non-mathematical introduction to the superspace description of modulated structures. Acta Cryst. B65, 249-268.

# Appendix A

# Python Script

```
import math*
#Enter structure parameters
a=0.4754,b=4.754, c=1.299
#Enter two planes which angles need to be computed
#plane 1 (h1,k1,l1)
h1=1.0, k1=1.0, l1=0.0
#plane 2 (h2,k2,l2)
h2=-1.0, k2=-1.0, l2=0.0
#————————-Calculations————————
A=(h1*h2+k1*k2+0.5*(h1*k2+h2*k1)+((3.*a*a)/(4.*c*c))*l1*l2)/
(math.sqrt(((h1*h1+k1*k1+k1*h1+((3.*a*a)/(4.*c*c))*l1*l1)
*(h2*h2+k2*k2+k2*h2+((3*a*a)/(4*c*c))*l2*l2))))
angle=math.degrees(math.acos(A))
ratio=(math.sqrt(4*c*c*(h1*h1+h1*k1+k1*k1)+3*a*l1*l1)/
math.sqrt(4*c*c*(h2*h2+h2*k2+k2*k2)+3*a*l2*l2))
#————————————————-lists of h k l
#import itertools
#for a in itertools.permutations([0, 1,-1, 2,-2],3):
```

```
#print a
#—-printout———
print ”————————”
print ” Then angle between (”,int(h1),”,”,int(k1),”,”,int(l1),”) and (”,int(h2),”,”,int(k2),”,”,int(l2),”)”
print angle
print ”ratio distance is”,ratio
```

# Appendix B

# Camara Length

To calibrate the camera length a procedure was used found in Champness[60] book. An aluminum standard was used for the calibration and the Table below shows the result of the calibration.

TABLE B.1: Conversion Table between JEOL JEM-2100 readout and measured camera constant

| JEOL readout (cm) | Measured Camera Length (mm) |
|---|---|
| 50 | 93.05 |
| 60 | 111.50 |
| 80 | 145.502 |
| 100 | 185.64 |
| 120 | 222.31 |
| 150 | 278.36 |
| 200 | 359.96 |